Numerical Simulation of Ion-Cyclotron Turbulence Generated by Artificial Plasma Cloud Release

Ouliang Chang

Thesis submitted to the Faculty of the
Virginia Polytechnic Institute and State University
in partial fulfillment of the requirements for the degree of

Master of Science
in
Electrical Engineering

Wayne A. Scales, Chair
Joseph J. Wang, Co-chair
C. Robert Clauer

July 01, 2009
Blacksburg, Virginia

Keywords: Finite Electron Mass Hybrid Simulation, Ring Velocity Distribution, Nonlinear Evolution, Shear Alfven Wave

Numerical Simulation of Ion-Cyclotron Turbulence Generated by Artificial Plasma Cloud Release

Ouliang Chang

(ABSTRACT)

Possibilities of generating plasma turbulence to provide control of space weather processes have been of particular interest in recent years. Such turbulence can be created by chemical released into a magnetized background plasma. The released plasma clouds are heavy ions which have ring velocity distribution and large free energy to drive the turbulence. An electromagnetic hybrid (fluid electrons and particle ions) model incorporating electron inertia is developed to study the generation and nonlinear evolution of this turbulence. Fourier pseudo-spectral methods are combined with finite difference methods to solve the electron momentum equations. Time integration is accomplished by a 4th-order Runge-Kutta scheme or predicator-corrector method. The numerical results show good agreement with theoretical prediction as well as provide further insights on the nonlinear turbulence evolution. Initially the turbulence lies near harmonics of the ring plasma ion cyclotron frequency and propagates nearly perpendicular to the background magnetic field as predicted by the linear theory. If the amplitude of the turbulence is sufficiently large, the quasi-electrostatic short wavelength ion cyclotron waves evolve nonlinearly into electromagnetic obliquely propagating shear Alfven waves with much longer wavelength. The results indicate that ring densities above a few percent of the background plasma density may produce wave amplitudes large enough for such an evolution to occur. The extraction of energy from the ring plasma may be in the range of 10-15% with a generally slight decrease in the magnitude as the ring density is increased from a few percent to several 10's of percent of the background plasma density. Possibilities to model the effects of nonlinear processes on energy extraction by introducing electron anomalous resistivity are also addressed. Suitability of the nonlinearly generated shear Alfven waves for applications to scattering radiation belt particles is discussed.

Acknowledgments

First, I want to express my special thanks to my family and friends who gave me strength, encouragement and enjoyment in my life in Blacksburg. Without their supports, I would not be able to withstand two years' stressful work to complete this thesis.

I would like to express my gratitude to my co-advisor, Dr. Wayne A. Scales for his valuable advice, guidance and encouragement during the course of this work. I sincerely appreciate for his enthusiasm and patience in helping me learn the basic plasma physics and in solving the problems I encountered during this research work.

I would like to thank my co-advisor, Dr. Joseph J. Wang for his guidance and direction for the last two years. He helped me quickly get used to the research and study life in U.S.. I learn a lot from his persistence in research and his broad knowledge on astronautical engineering field. Without his direction and support, I would not be able to complete this thesis.

I would like to thank Dr. C. Robert Clauer for serving in my advisory committee and his passionate lectures that bring me into the world of space science. I would like to acknowledge Dr. G. Ganguli and Dr. L. Rudakov for their useful suggestions and comments during this research work.

Finally, I would like to thank anyone who ever help me in my study, research and daily life in these two years time.

This work is supported in part by the Office of Naval Research (ONR) through a MURI project led by University of Maryland.

Contents

List of Figures

List of Tables

Chapter 1

Introduction

Plasma is a ubiquitous form of matter in the universe. It is nearly always found to be magnetized and turbulent under a wide range of conditions including space and astrophysical plasmas as well as those produced in laboratory confinement devices [20]. It is said to be in turbulent state when the plasma waves are excited by the free energy in a broad continuous spectrum of frequency and experience random-looking fluctuations [7]. From a more fundamental point of view, plasma turbulence is a paradigmatic example of nonlinear dynamics in open systems with many degrees of freedom, such as velocity, electric field. Here, the system typically establishes a quasi-stationary state far from the true thermodynamic equilibrium [13]. The importance of understanding turbulence in space plasma is not only of interest to space plasma physics such as Rayleigh-Taylor instability in solar prominences [10], but also has practical applications, for example, the influence on the radio wave communication and navigation systems through scattering [39]. Since turbulence determines the general plasma state in space, it can affect the composition and dynamics of plasma constituents and is a key factor in determination of space weather which is critically important to the reliability of space assets [15]. Therefore, the low frequency turbulence in space plasma has been studied extensively [30, 45, 48]. However, the understanding of ion-cyclotron turbulence, despite its importance to the near-Earth environment, is not fully developed [28, 46, 47].

An effective way to study the properties of ion-cyclotron turbulence is to seed the turbulence in the near-Earth environment and monitor its nonlinear evolution and waves characteristics closely. As recently being proposed [15], the release of an artificial plasma cloud in the magnetosphere perpendicular to the local magnetic field may induce intense ion-cyclotron turbulence in a large volume with unique properties. Of particular interest is the possibility of such turbulence providing control of space weather processes. The scenario for generating this turbulence is the release, from a spacecraft, of an easily ionizable chemical such as lithium, cesium, etc. Upon ionization through photoionization process, a heavy ion component will be produced in the background plasma which has an anisotropic ring-velocity distribution in phase space far from thermodynamic equilibrium. Although chemical releases in the near-

Earth space environment have been studied for decades [4, 14, 16, 40], the proposed process is unique in the sense that it designs a local unstable ion distribution through shaped release of neutral gas and the free energy for development of turbulence is the kinetic energy contained in the ring-velocity plasma, which is drawn directly and efficiently from the orbital kinetic energy of the spacecraft. This amount of free energy is greater by many orders of magnitude than the energy that could be supplied to waves by any electrically driven antenna [21] and therefore the excited turbulence has the ability to greatly impact space weathering processes for such applications as the Earth's radiation belts remediation.

Specific wave modes of importance for interaction with radiation belt particles would be electromagnetic waves which would have ability to pitch angle scatter trapped relativistic electrons. Examples studied in the past include whistler and electromagnetic ion cyclotron EMIC waves [4, 26, 38] as well as lower hybrid resonance driven by ring-velocity instabilities [1, 24, 27]. Our study, however, focus on an alternative type of electromagnetic plasma turbulence (shear Alfven) induced by the ion ring-velocity instability. The frequency of the turbulence considered is near ion cyclotron harmonic frequencies of ring-velocity plasma created by the released chemical species. The waves generated are quasi-electrostatic short wavelength shear Alfven waves ($k_\perp \gg k_z$, where $k_\perp$ and k_z are the wavenumber perpendicular and parallel to the ambient magnetic field, respectively) that initially propagate nearly perpendicular to the magnetic field. It has been proposed that [15], through wave-wave coalescence, the nonlinear evolution of these waves ultimately results in electromagnetic longer wavelength shear Alfven waves ($k_\perp \sim k_z$) which propagate obliquely (although further away from perpendicular to the magnetic field), and have the ability to pitch angle scatter radiation belt electrons. Figure 1.1 shows a schematic overview of the essential process involved.

There are several important plasma physics questions that must be answered to access the practicality of this scenario [41]. First, is the efficiency of extraction of the ring-velocity plasma kinetic energy into wave energy through wave-particle processes sufficient to make a useful impact on the background plasma? Another question is what is the amplitude and characteristics of the waves in a nonlinear saturated state? Also, do these waves appear to have characteristics in frequency and wavenumber that are suitable for interactions with energetic particles? To answer these questions, a two-dimensional hybrid computational model has been developed to model the generation and nonlinear evolution of this turbulence. A particle-in-cell PIC model is used to describe the background ions and ring-velocity plasma since we want to ultimately investigate the transport of kinetic energy between different species. To save computational time, a fluid model is chosen to describe electrons as many phenomena can be explained by this simplified model. An important modification to classical fluid model is made through introducing electron inertia term in the electron momentum equation in order to correctly describe the short wavelength shear Alfven wave. In order to model the impacts of further nonlinear processes on the released energy extraction efficiency, the electron anomalous resistivity is also incorporated in the momentum equation. Using this computational model, we conduct a number of simulations on the evolution of the ion-

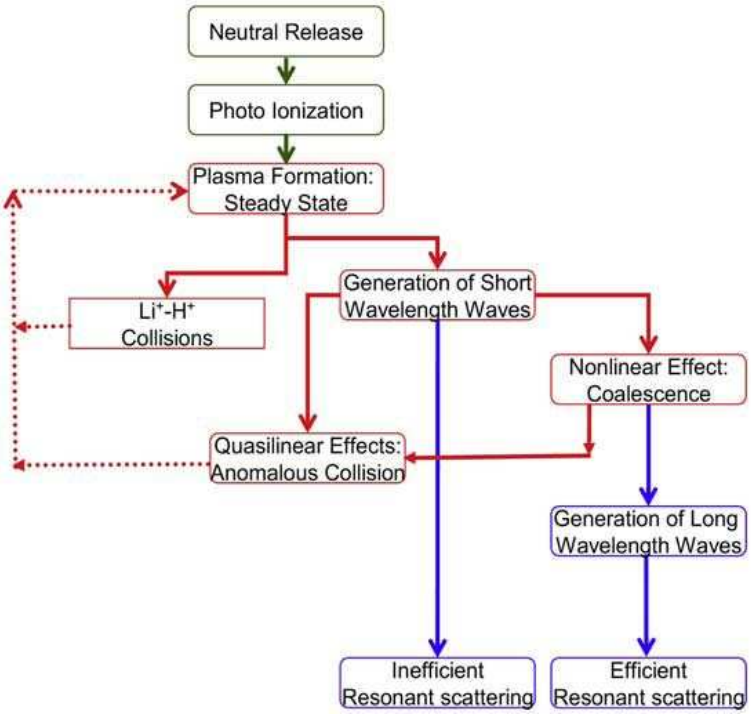

Figure 1.1: A schematic of key processes. The green and red color represent the input energy and plasma formation, respectively, while the blue represents the resulting signatures [15].

cyclotron waves generated by the ring-velocity instability under a range of parameters for the release species. These results detail the nonlinear wave-particle and wave-wave processes in the perspective of temporal evolution as well as variation of ring plasma density.

The next chapter gives a background overview including the linear theory of the ion-cyclotron instability under consideration. The computational model with numerical methods is described in the following chapter. The details of the simulation results are then shown and discussed. Finally, conclusions and future work are presented to ultimately access the feasibility of the radiation belt remediation through seeding ion-cyclotron turbulence by neutral gas release.

Chapter 2

Background

In this chapter, we first present a background review on the trapped radiation belt including causes of its existence and its impact on space assets. We then describe the concept of the radiation belt remediation through generating the ion-cyclotron turbulence by artificial plasma cloud release. The linear theory of ion-cyclotron instability and the classical hybrid computational model for space plasma simulation is also reviewed and the limitation of the classical model is pointed out, followed by the introduction of the theory of pitch angle scattering in the radiation belt environment.

2.1 The trapped radiation belt

In our study, the trapped radiation belt refers specifically to the radiation belts surrounding the Earth, although similar radiation belts have been discovered around other planets [23]. In this section, we first give a basic introduction of radiation belt, followed by the reasons why the particles are trapped in the radiation belts. Last, the influence of space weather on space activities and assets is discussed.

2.1.1 Van Allen radiation belt

The Van Allen radiation belts are two donut-shaped regions of energetic charged particles, mainly protons and electrons, trapped at high altitudes in the magnetic field of the Earth as shown in Fig. 2.1. The Van Allen belts are most intense over the Equator and are effectively absent above the poles [8]. No real gap exists between the two belts; they actually merge gradually, with the flux of charged particles showing two regions of maximum density. The inner region is centered approximately 3,000 km above the terrestrial surface. The outer region of maximum density is centered at an altitude of about 15,000 to 20,000 km. This

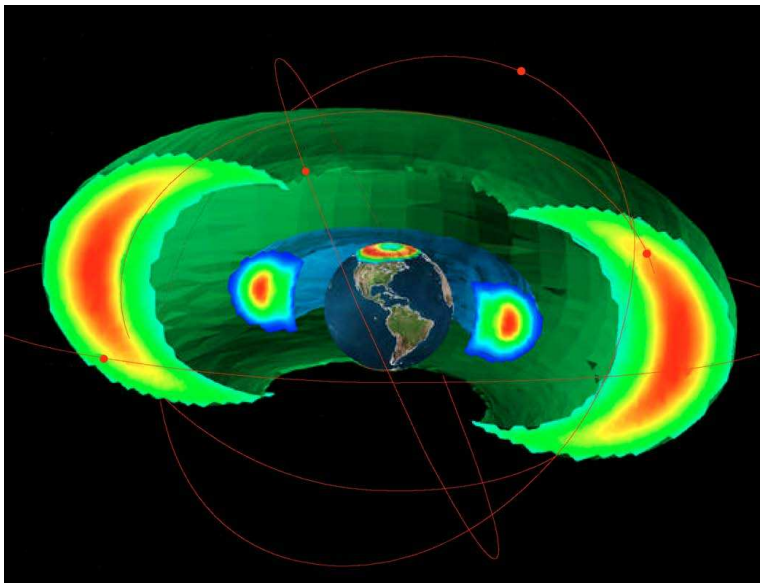

Figure 2.1: A schematic of the Van Allen radiation belts generated by computer model showing the two main radiation belts, the outer belt and the inner belt [Courtesy of the Air Force Research Laboratory].

can be seen from Van Allen's first map (Fig. 2.2) of the radiation belts.

The inner radiation belt consists largely of highly energetic protons, with exceeding 30MeV. It is believed that the protons of the inner belt originate from the decay of neutrons produced when high energy cosmic rays from outside the solar system collide with atoms and molecules of the Earth's atmosphere [5]. This is a fairly stable population but it is subject to occasional perturbations due to geomagnetic storms, and it varies with 11-year solar cycle.

The outer belt consists mainly of high energy (0.1-10 MeV) electrons trapped by the Earth's magnetosphere. The protons of the outer belt have much lower energies than those of the inner belt, but their fluxes are much higher. The energetic particles in the outer belts are produced by injections and energization events following geomagnetic storms and sequent wave-particle interactions [19], which make them much more dynamic than the inner belt. While radiation belt particles are lost, e.g., by collision with the rarefied gas of the outermost atmosphere, the new ones are frequently injected from the magnetotail [44]. The particle population of the outer belt fluctuates widely and could possibly rise to energies of order 10 MeV when geomagnetic storms occur.

2.1.2 The trapped particles

It is generally understood that the Van Allen belts are a result of the collision of Earth's magnetic field with the solar wind [23]. Radiation from the solar wind then becomes trapped

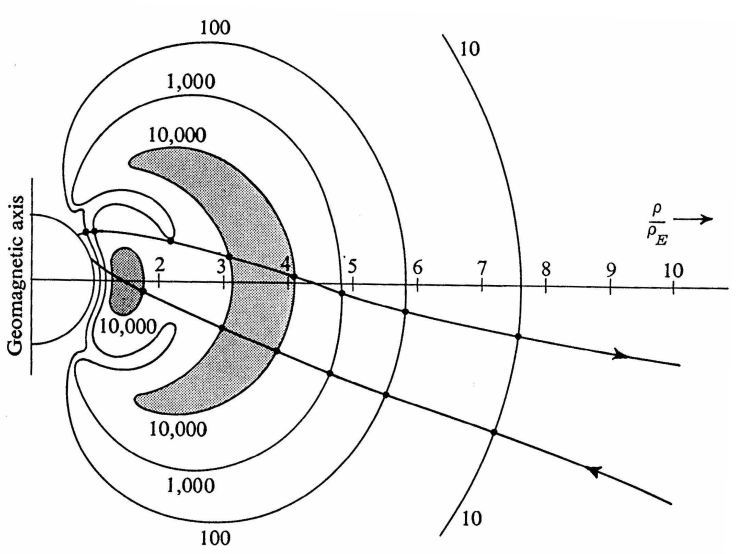

Figure 2.2: Van Allen's first map of the radiation belts, showing the inner and outer zones of high count rate. The contours are labeled by the count rate of a Geiger counter of about $1cm^2$ area covered by $1gm/cm^2$ of lead [2].

in the Earth's magnetic field because of the so-called magnetic mirror effect. To understand the magnetic mirror effect, we need to be aware of the motions of trapped particles in the radiation belts first.

There are three primary cyclic motions in Earth's magnetic field [7], which are illustrated in Fig. 2.3. The first and simplest one is gyro motion. That is the particle gyrating around the magnetic field line in an equipotential plane. The typical time scale for gyro motion is microseconds for trapped electrons and milliseconds for trapped protons [39]. The force of gyro motion is the Lorentz force in a uniform magnetic field which can be expressed as Eq. (2.1) below:

$$m\frac{d\vec{v}}{dt} = q(\vec{v} \times \vec{B}) \tag{2.1}$$

The center of the circular orbit of gyro motion is called guiding center, which also has its own motion. In general, the motion of the trapped particles is the sum of the gyro motion and the other two guiding center motion, which are drift motion and bounce motion.

The drift motion of trapped particles is a slow drift from one field line to another, gradually going all the way around Earth. Ions drift westward, electrons drift eastward. Due to the different direction of drift motion of ions and electrons, an electric current is produced circling the Earth clockwise. The typical time scale for drift motion is 30 minutes for ions and 50 minutes for electrons to circle around the Earth. The drift motion is due to the curvature of the Earth's magnetic field which produces not only centrifugal forces, but also

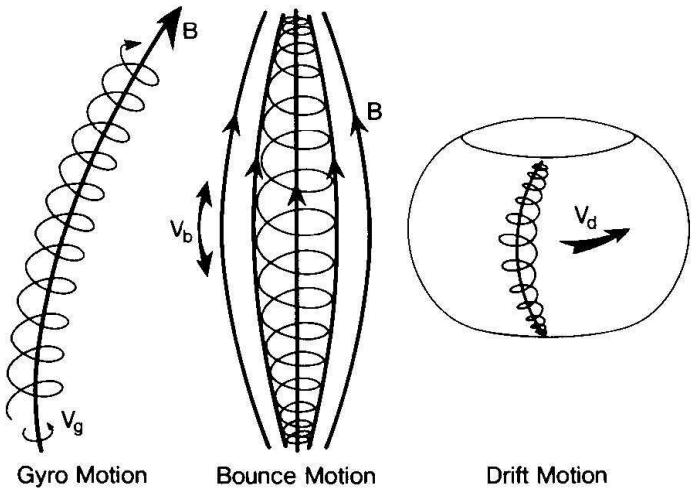

Figure 2.3: Three cyclic motions in the Earth's dipolar magnetic field [37].

gradient $\vec{B}$ forces on the guiding center motion. Since any curved field will have a gradient $\vec{B}$ perpendicular to the field line, the inhomogeneous magnetic field then produces a force term acting on the guide center, which can be expressed as Eq. (2.2) below:

$$m\frac{d\vec{v}}{dt} = q(\vec{v} \times \vec{B}) - \mu\nabla_{\perp}\vec{B} \tag{2.2}$$

Here μ is magnetic moment which equals to $\frac{1}{2}mv_{\perp}^2$, where subscript $\perp$ denotes the direction perpendicular to the background field line. The centrifugal force is $\vec{F}_{cf} = \frac{mv_z^2}{R_c}\hat{r}$, where subscript z denotes the direction along the background field line, R_c is the radius of curvature and $\hat{r}$ is a unit vector that points outwards the center of curvature. Combing the two forces together, we can find the velocity of the guiding center's drift motion as shown in Eq. (2.3) below:

$$\vec{v}_{\nabla_{\perp}B} + \vec{v}_R = \frac{m}{q}\frac{\vec{R}_c \times \vec{B}}{R_c^2 B^2}(v_z^2 + \frac{1}{2}v_{\perp}^2) \tag{2.3}$$

The third motion of trapped particles is bounce motion. The force of bounce motion is due to the inhomogeneity along the magnetic field line, which is expressed as $\vec{F}_z = -\mu\nabla_z\vec{B}$, or simply the $\vec{v} \times \vec{B}$ force in the parallel direction due to cross product of the perpendicular components. When particles in the radiation belt gyrate around field lines, they also move along field lines. As the particles approach either of the magnetic poles where field lines converge, the increase in the strength of the field can slow down and reverse the parallel velocity, reflecting the particles. The magnetic force is much stronger near the Earth than far away, and on any field line it is greatest at the ends, where the line enters the atmosphere. Thus electrons and ions can remain trapped for a long time, bouncing back and forth from

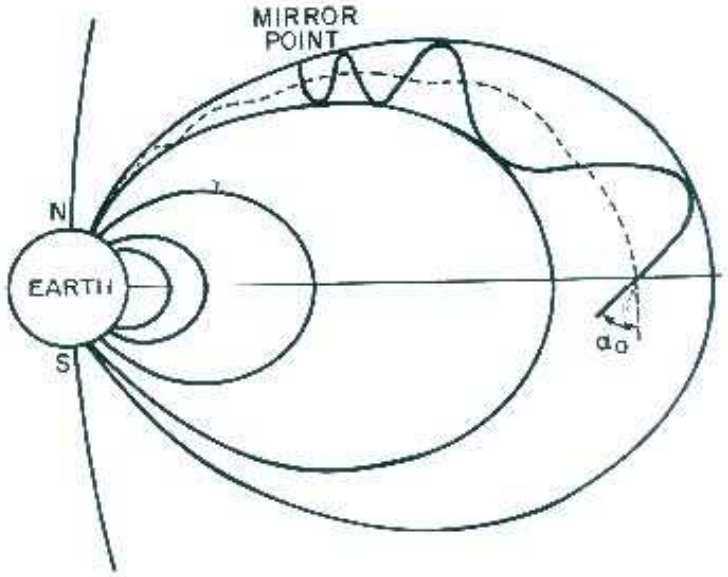

Figure 2.4: The mirror effect of the Earth's magnetic field. One particle bounces, the other is lost [8].

mirror point in one hemisphere to the other. This is the magnetic mirror effect and in this way the Earth holds on to its radiation belts. The typical time scale for bounce motion is 1 second for ions and 0.1 second for electrons to bounce around the two magnetic poles.

However, not all the particles can be repelled by the magnetic mirror effect. When the parallel velocity is large enough, or the pitch angle is smaller than the critical condition, the particles will not be reflected and is said to be lost in the loss cone [7]. Only those particles whose pitch angle is larger or equal to the critical value can be trapped in the belts. The relation can be expressed in Eq. (2.4):

$$\sin\alpha = \frac{v_\perp}{\sqrt{v_\perp^2 + v_z^2}} \geq \sqrt{\frac{B}{B_{max}}} \tag{2.4}$$

where α is the pitch angle, defined as the angle between the velocity vector and the magnetic field line, B_{max} is the maximum magnetic field. Figure 2.4 shows two particles, one is reflected in the mirror point; the other is lost in the loss cone. Even those trapped particles are not forever bouncing between the mirror points. Over time to time, they could collide with atoms in the thin atmosphere, changing their velocity vector and pitch angle, resulting in their removal from the radiation belt. However, more energetic particles are continuously injected in the belt region and then become trapped, forming the current radiation belt structure.

The gap between the inner and outer Van Allen belts, which is also called safe slot, is caused by the very low frequency (VLF) radio waves scattering particles in pitch angle and thus

ejecting the particles that would otherwise accumulate there [8]. This mechanism indicates the possibility to pitch angle scatter the trapped particles with suitable electromagnetic waves artificially generated in the radiation belt. We will come back to this scenario later in section 2.2.

2.1.3 Space weather impact

Space weather is the concept of changing environmental conditions in near-Earth space within the magnetosphere. It is distinct from the concept of weather within a planetary atmosphere, and deals with phenomena involving ambient plasma, magnetic fields, radiation and other matter in space [29]. A variety of physical phenomena are associated with space weather, including geomagnetic storms and substorms, energization of the Van Allen radiation belts, ionospheric disturbances and scintillation, aurora and geomagnetically induced currents at Earth's surface.

Space weather is of importance primarily because it exerts a profound influence in several areas related to space exploration, development and even our daily activities on the Earth [42]. Changing geomagnetic conditions can induce changes in atmospheric density causing the rapid degradation of spacecraft altitude in LEO. Geomagnetic storms due to increased solar activities can potentially blind sensors aboard spacecrafts, interfere with on-board electronics and blackout HF radio communications. An understanding of space environmental conditions is also important in designing shielding and life support systems for manned spacecraft, as the radiation dose can damage electronics onboard spacecraft through induced electric currents and threaten the life of astronauts. Besides, electrojets in geomagnetic storms can cause those ground induced currents which may lead to power grid transformer catastrophic failure and massive electricity blackout [8].

The Van Allen radiation belt, particularly, produces a harmful effect on man and electronics due to the high energy particle radiation. Solar cells, integrated circuits, and sensors can be damaged by the energetic particles' radiation. Electronics on satellites must be hardened against radiation to operate reliably [17]. However, even with shielding, during the geomagnetic storms, satellites are still very vulnerable to the enhanced radiation dose. Some human activities, such as a high altitude nuclear weapon test [12, 34], could also inject high energy electrons into the inner radiation belt and energize the radiation which could damage or even destroy many satellites in LEO. The estimation of the enhanced energetic electron population after a nuclear detonation can be found in Fig 2.5.

Since the radiation belts are hazards for satellites and moderately dangerous for human beings, difficult and expensive to shield against, it has been proposed to remove the belts by draining the trapped energetic particles out of the region. One way to achieve it is to pitch angle scatter the particles by wave-particle interactions generated by artificial plasma turbulence. We will describe this approach in the following section.

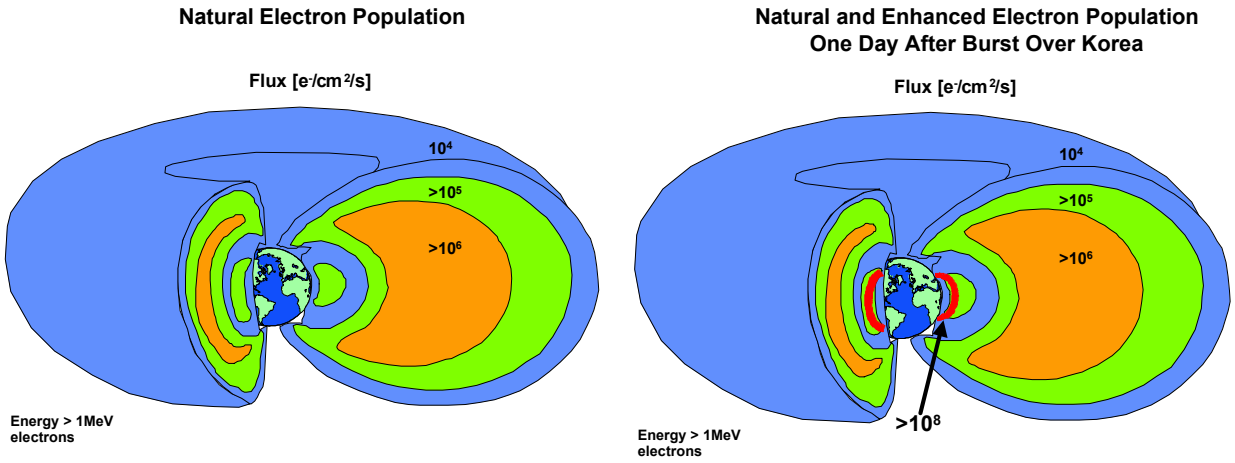

Figure 2.5: Radiation belts pumping by a high altitude nuclear burst [34].

2.2 Remediation of the radiation belt

The concept of the radiation belt remediation through seeding ion-cyclotron turbulence by artificial plasma cloud release and utilizing the turbulence for scattering relativistic electrons is initially proposed by Ref. [15]. Such idea is based on release of an easily ionized vapor (we will consider lithium throughout this thesis) into a background electron-hydrogen plasma representative of the Earth's magnetosphere from a satellite traversing the radiation belt. The essential ingredient for the success of the concept is the ability to create a ring-velocity distribution in the perpendicular velocity of the released chemical ions through photoionization. As mentioned in chapter 1, this converts the large orbital kinetic energy of the neutrals into a reservoir of free energy for the waves to tap into. Intense plasma instability will be triggered by this ring-velocity distribution, and the waves generated are quasi-electrostatic, perpendicular propagating short wavelength Alfven wave amplified around lithium harmonics. After the saturation of linear wave growth, the nonlinear wave-wave process will result in plasma turbulence, converting the quasi-electrostatic short wavelength waves into electromagnetic longer wavelength shear Alfven wave, propagating far from perpendicular direction. These daughter waves are said to be capable of wave-particle interacting with the trapped relativistic electrons in the radiation belts and transfer a portion of free energy to them. The electrons are then accelerated by the waves and their pitch angles are decreased. Through this way, the trapped electrons can be scattered into loss cone and finally out of the radiation belts in their bounce motion to the magnetic poles as described in section 2.1.2. Let us first briefly review the creation of plasma cloud with a ring-velocity distribution, followed by the linear theory of the initial generation of highly oblique shear Alfven waves near lithium cyclotron harmonics. Then the classical hybrid computational model to simulate the nonlinear process is discussed. Finally, a brief estimation of the efficiency of pitch angle scattering of relativistic electrons through this approach is accessed.

2.2.1 Creation of plasma cloud with a ring-velocity distribution

It is the neutral gas released from a satellite that leads to the formation of plasma with an anisotropic ring-velocity distribution. The neutral gas chosen, is usually cold, heavy and easily ionized chemical, such as lithium. The vaporized lithium is released from nozzles on a satellite body radially normal to the satellite orbit in Earth's equatorial plane where the ambient magnetic field is perpendicular to the satellite orbit, shown schematically in Fig. 2.6(a). The desired release altitude is between $3000km$ and $9000km$, corresponding to $L = 1.5 \sim 2.5$. It gives the neutral lithium a large perpendicular velocity $v_\perp$ which equals the satellite orbital velocity $v_s \sim 7km/s$. This leads to an anisotropic velocity distribution ($v_\perp \approx V_s \gg v_z$), which is essential to drive plasma instabilities. The lithium atoms will then form a neutral cloud and move across the magnetic field line following the satellite trajectory. Given a proper releasing speed V_R , it is possible that the width of the lithium cloud can reach as long as $\Delta L \approx 1$ ($6000km$) shown in Fig. 2.6(b).

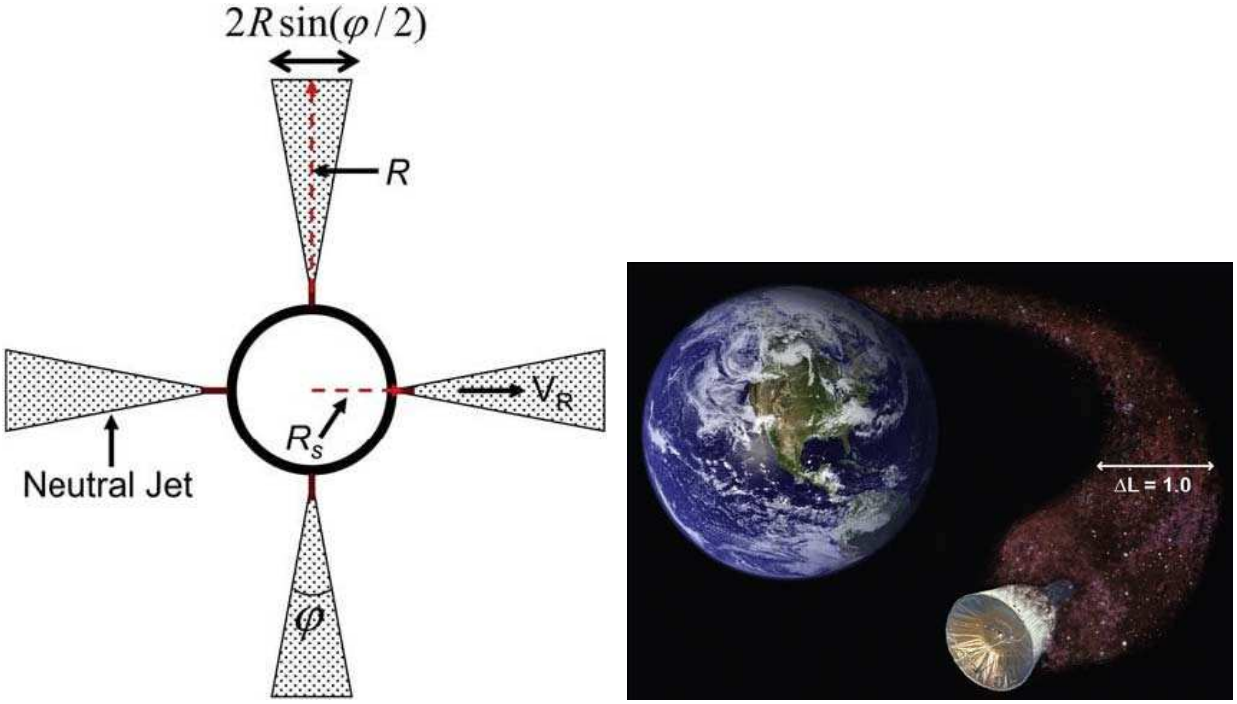

(a) A schematic of the cross section perpendicular to the satellite orbit. Here R_s is the satellite dimension. Four nozzles inject conical jets of neutral lithium with velocity V_R perpendicular to the satellite motion simultaneously and continuously.

(b) A lithium cloud of width $\Delta L \approx 1$ ($6000km$) is photoionized into a plasma cloud in the Earth's equatorial plane where the ambient magnetic field is perpendicular to satellite orbit.

Figure 2.6: Schematics of the neutral lithium gas release [15].

After becoming ionized through photoionization, the ions will attach to the Earth's magnetic field line in the equatorial plane and begin gyro motion around the field line. Consequently,

they can no longer move across the field lines. Note that at this time, these ions still have larger perpendicular velocity $v_\perp$. After the ions spinning up around the field line, the perpendicular velocity is randomly pointing every direction in the equatorial plane and therefore forms a narrow distribution of velocities perpendicular to the background magnetic field B_0, centered just at V_s. In the phase space $v_x - v_y$(where subscript x and y denote two perpendicular direction), this distribution forms a ring shape and thus is called ring-velocity distribution. The phase space of ring-velocity distribution is shown in Fig. 4.14, chapter 4. The initial lithium ring-velocity distribution function can be approximated below [15]:

$$f_0 = \frac{1}{(2\pi)^{3/2} v_{t\perp}^2 v_{tz}} \exp(-\frac{(v_\perp - v_r)^2}{2v_{t\perp}^2} - \frac{v_z^2}{2v_{tz}^2}) \tag{2.5}$$

Here subscript t denotes the thermal component. We also define the ring plasma velocity v_r which equals satellite orbit velocity V_s. Initially, $v_{tz}, v_{t\perp} \ll v_r$ and the injection energy per ion $E = \frac{1}{2} m_{Li} v_r^2$ equals to $1.79eV$, indicating a huge amount of total energy. As we said before, this amount of free energy could leads to the plasma instability, which as shown in the following section generates relatively short wavelength ($k_\perp \gg k_z$) shear Alfven waves near lithium cyclotron harmonics.

2.2.2 Linear theory of electromagnetic ion-cyclotron instability

Plasma instability refers to the growth of wave amplitude and the transfer of energy and momentum from a source of free energy in the plasma. The plasma instability is always a motion which decreases the free energy and brings the plasma closer to the thermodynamic equilibrium where the wave amplitude reaches a steady state value in nonlinear evolution [7]. Turbulence or irregularities in space plasmas are produced by plasma instabilities through their nonlinear evolution.

If the waves are to grow, the frequency ω must be complex. The complex frequency can be express as $\omega = \omega_r + i\gamma$, where ω_r and γ are real, and γ is positive. Since the field is expressed as $E = E_0 + E_1 e^{-i(\vec{k}\cdot\vec{r} - \omega t)}$, the amplitude of small fluctuation term will grows exponentially with time $E_1 e^{\gamma t}$. γ is then called the growth rate. As the approximation of the linear plasma wave theory is used, the exponentially growing wave could only satisfies the approximation for a short time compared with $1/\gamma$; at longer time, the waves become nonlinear and the mathematical expressions above are no longer applicable.

There are many plasma conditions to drive instability and for this particular study, it is the anisotropic ring-velocity distribution of lithium ions to trigger this ion-cyclotron instability. Physically speaking, the growth of waves is due to wave-particle interactions through inverse ion Landau damping. The wave phase velocity $\vec{v_p} = \omega/\vec{k}$ under consideration is near the ring plasma velocity v_r and thus the lithium ions could transfer part of the free energy to the growing waves. It is the same as surfing in the ocean [7]. If the surfboard moves slightly

faster than the wave, it would push on the waves as it moves uphill; the wave then could gain energy while the surfboard loses energy.

The detailed linear theory of the ion-cyclotron instability can be found in Ref. [15] for the case of releasing lithium into an ambient electron-hydrogen plasma under parameters of the Earth's magnetosphere at $L = 2$ $(6000km)$. Only a brief review of the key characteristics of the plasma instability will be described here.

Considering short wavelength shear Alfven waves where $k_x \gg k_z, k_y = 0$ (two dimension in space), the dispersion relation is determined by Maxwell equations neglecting the displacement current:

$$\vec{\nabla} \times \vec{B} = \frac{4\pi}{c}\vec{J} \Longleftrightarrow i\vec{k} \times \vec{B} = \frac{4\pi}{c}\vec{J} \tag{2.6}$$

$$\vec{\nabla} \times \vec{E} = -\frac{1}{c}\frac{\partial \vec{B}}{\partial t} \Longleftrightarrow \vec{k} \times \vec{E} = \frac{\omega}{c}\vec{B} \tag{2.7}$$

Using Eq. (2.7) to represent $\vec{B}$ in Eq. (2.6), we can get:

$$(k_x^2 + k_z^2)\vec{E} - \vec{k}(k_x E_x + k_z E_z) = \frac{4\pi i\omega}{c^2}\vec{J} \tag{2.8}$$

The quasi-neutral condition gives:

$$\vec{\nabla} \cdot \vec{J} = 0 \tag{2.9}$$

where $\vec{J} = \bar{\boldsymbol{\sigma}} \cdot \vec{E}$ and $\bar{\boldsymbol{\sigma}}$ is the conductivity tensor. From the y component of Eq. (2.8):

$$E_y = \frac{4\pi i\omega\sigma_{yx}}{k^2c^2(1 - \frac{4\pi i\omega\sigma_{yy}}{c^2k^2})}E_x \tag{2.10}$$

and the quasi-neutral condition gives:

$$E_z = -\frac{\sigma_{xx}k_x}{\sigma_{zz}k_z}E_x \tag{2.11}$$

Substituting Eq. (2.10) and Eq. (2.11) for E_y and E_z respectively in the x component of Eq. (2.8), we obtain the dispersion relation for the shear Alfven wave for $k_x \gg k_z$:

$$\frac{k_z^2c^2}{\omega^2} = \frac{4\pi i}{\omega}\sigma_{xx}\left(1 - \frac{k_x^2c^2}{4\pi i\omega\sigma_{zz}}\right) \tag{2.12}$$

The derivation of getting and is described in detail in Ref. [15]. Substituting the expression

of conductivity in Eq. (2.12) gives the dispersion relation:

$$\begin{aligned} D(\omega,k) = & \frac{k_z^2 V_A^2}{\omega^2}\left(1+\frac{k_x^2c^2}{\omega_{pe}^2}\frac{1}{\zeta^2 Z'(\zeta)}\right)^{-1} \\ & -\sum_\ell \frac{\ell^2\Omega_H^2}{\ell^2\Omega_H^2-\omega^2}\frac{2\Gamma_\ell(b_H)}{b_H} \\ & +\sum_\ell \frac{n_{Li}m_{Li}}{n_H m_H}\frac{dJ_\ell^2(\sigma_s)}{\sigma_s d\sigma_s}\frac{\ell^2\Omega_{Li}^2}{\omega(\omega-\ell\Omega_{Li})} \\ & = 0 \end{aligned} \tag{2.13}$$

where the subscripts H, e, Li indicate ambient ion hydrogen, electron and lithium, respectively. m denotes the species mass and n denotes the particle density. ℓ is the cyclotron harmonic number. $\Omega_{H(Li)}$ is the hydrogen (lithium) cyclotron frequency and $\omega_{pe(pH)}$ is the electron (hydrogen) plasma frequency. V_A is the Alfven speed and c is the speed of light in vacuum. $Z'(\zeta)$ is the derivative of the plasma dispersion function, $\zeta = \omega/\sqrt{2}k_z v_{te}$. $\Gamma_\ell(b_H) = I_\ell(b_H)exp(-b_H)$, where I_ℓ is the modified Bessel function, $b_H = (k_x\rho_H)^2/2$ and $\rho_H = v_{tH}/\Omega_H$ is the hydrogen gyroradius. J_ℓ is the Bessel function of order ℓ and $\sigma_s = k_x v_r/\Omega_{Li}$.

As we can see, the dispersion relation consists of three terms. The first two terms are due to ambient electron and ions. The third term, due to the ring-velocity lithium ions, is responsible for the instability of short wavelength shear Alfven waves. Note that we ignore the thermal lithium component from the dispersion relation since initially the lithium ions are assumed to be cold. As the thermal lithium population increases with time, there exists a threshold for the instability where the wave amplitude saturates at a steady state value. The growth rate γ is obtained from imposing the double resonance condition that the real frequency ω_r is determined by both Eq. (2.13) and the lithium cyclotron harmonic frequencies $\omega_r = \ell\Omega_{Li}$. The growth rate then can be expressed as [15]:

$$\gamma = \frac{\ell\Omega_{Li}}{2}\left[-\Delta+\sqrt{\Delta^2+\frac{n_{Li}m_{Li}}{n_H m_H}\left|\frac{dJ_\ell^2(\sigma_s)}{\sigma_s d\sigma_s}\right|\frac{b_H}{\Gamma_1(b_H)}\left(\frac{\Omega_H^2-\ell^2\Omega_{Li}^2}{\Omega_H^2}\right)^2}\right] \tag{2.14}$$

where $\Delta = \zeta^3\exp(-\zeta^2)\left(\frac{\Omega_H^2-\ell^2\Omega_{Li}^2}{2\Omega_H^2}\right)$.

Solving Eq. (2.14) numerically, we can obtain the growth rate versus wavenumber. Figure 2.7 shows the growth rate for parameters consistent with creation of ring-velocity lithium ions at an altitude approximately $6000km$. The ambient hydrogen density is fixed at $n_H = 3\times10^3 cm^{-3}$, electron and hydrogen temperature are equal at $T_e = T_H = 0.53eV$, the lithium ring is assumed to be cold at $T_{Li}\approx 0$. $B_0 \approx 0.04G$, $V_A = 1.6\times10^3 km/s$, $v_r = 7km/s$ and $m_{Li}/m_H = 7$. Four values of the ratio of lithium to hydrogen ion density $n_{Li}/n_H = 1\%, 5\%, 10\%$ and 30% are shown to assess the variation of density on wave processes. The first three harmonics $\ell = 1, 2, 3$ which have the largest growth rate are shown. Fixed values

of k_x are shown for each harmonic so the growth rate is maximized while k_z is varied. It should be noted that the waves propagate nearly perpendicular to the magnetic field with $k_x/k_z \sim 250$. Therefore initially these waves have short wavelengths, propagating perpendicular to the magnetic field. In the lowest density case, the $\ell = 1$ harmonic has a significantly higher growth rate than the higher harmonics. It can be observed from Fig. 2.7 that increasing the ring density tends to drive the harmonics to more similar amplitudes.

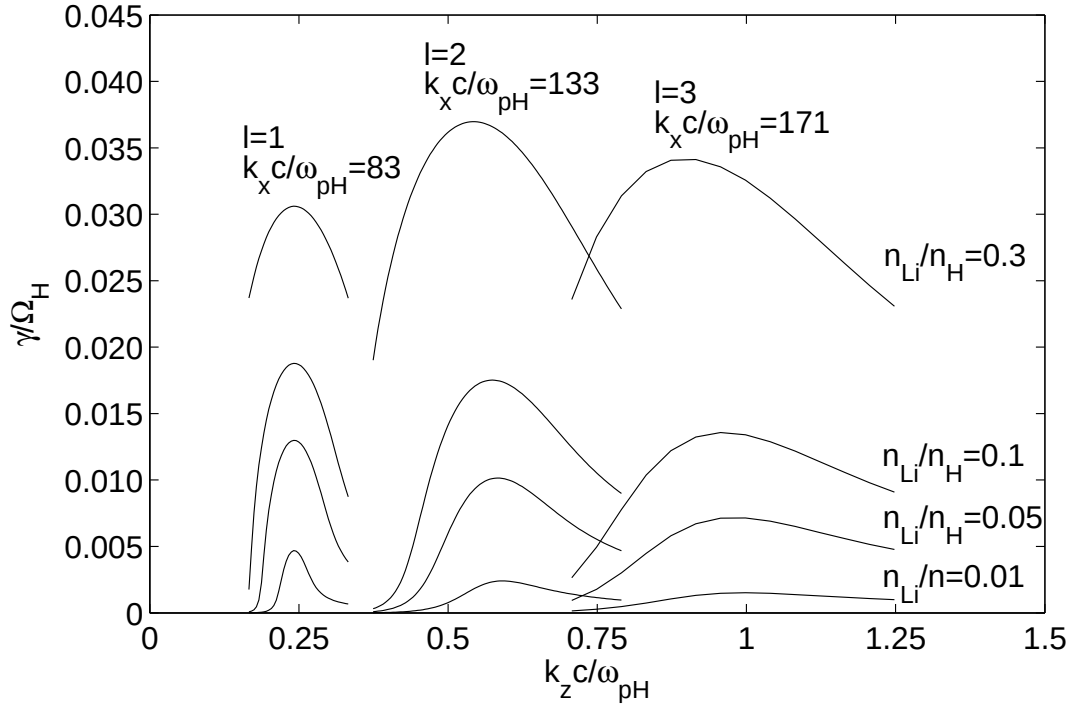

Figure 2.7: Variation of linear growth rate of the first three lithium cyclotron harmonics ℓ versus parallel wavenumber k_z for different density ratios n_{Li}/n_H. The perpendicular wavenumber k_x is chosen to achieve maximum growth for each cyclotron harmonic.

The energy of these waves is largely in the kinetic energy of the particles (hydrogen and electron). This can be observed by comparing particles' kinetic and fluctuating field energy shown in Eq. (2.15).

$$\frac{(m_e n_e |v_e|^2 + m_H n_H |v_H|^2)/2}{|B|^2/8\pi} = (1 + \frac{2k_x^2 c^2}{\omega_{pe}^2}) \gg 1 \tag{2.15}$$

$$W_1 \approx \frac{|B|^2}{8\pi}(1 + \frac{2k_x^2 c^2}{\omega_{pe}^2}) \tag{2.16}$$

Here W_1 denotes the initial wave energy density. Eq. (2.15) and (2.16) indicates, initially, the waves generated by the ring velocity instability are weakly electromagnetic in nature,

but rather quasi-electrostatic with most energy stored in particles. Such signatures are observed in the simulation results of chapter 4. Ref. [15] shows that an important nonlinear effect will make these waves evolve into longer wavelength electromagnetic waves with energy density W_2 equally partitioned in the fluctuating fields and the particles, which is expressed in Eq. (2.17).

$$W_2 \approx \frac{|B|^2}{8\pi}(1 + \frac{k_z^2 c^2}{\omega_{pH}^2}) \tag{2.17}$$

2.2.3 Classical electromagnetic hybrid computational model

Since the linear plasma wave approach is based on perturbation theory, the linear theory results are only valid for a short time when the wave amplitude is still relatively small, as described in section 2.2.2. The waves are then in the nonlinear evolution and turbulent state. There is much more important information in nonlinear evolution of turbulence, such as the energy exchange between waves and plasma cloud, the wave-wave process, etc. Therefore, another technique is needed to access the nonlinear process. Usually, we need to investigate the nonlinear development of plasma turbulence in a numerical way and the classical hybrid model is one of commonly used computational models to study plasma instabilities and nonlinear evolutions.

Generally, the term "hybrid model" in plasma physics can refer to any computational model in which one or more of the plasma species are neglected the identity of individual particles and treated as a single or multiple fluids that only the motion of fluid elements as a whole is taken into account, while the remaining species are treated kinetically as particles [52]. That's why it is called hybrid model. The plasma in the hybrid model can be coupled to the electromagnetic fields in a variety of ways: full Maxwell equations, low-frequency approximation (neglect displacement current), electrostatic only, etc. The classical electromagnetic hybrid model usually refers to the most common type of hybrid model used in space plasmas: where all the ions are treated kinetically, the electrons are assumed to be a single massless fluid, and the electromagnetic fields are treated in the low-frequency approximation.

A classical hybrid computation [52] usually model phenomena that occur on shorter time and distance scales than can be treated by magnetohydrodynamics (MHD) model in fluid limit and yet do not resolve processes that occur on electron scales (e.g., electron inertial length c/ω_{pe} and electron plasma frequency ω_{pe}) which are usually treated with fully particle-in-cell (PIC) techniques [3]. The relevant hybrid scales are then the ion inertial length c/ω_{pH}, and ion cyclotron frequency Ω_H. In space, the length scale is typically on the order of 10's to 100's of kilometers and times on the order of seconds.

A typical shear Alfven wave is an ion mode wave [7] and is on the ion spatial and time scale which is suitable to be modeled by the classical hybrid model. However, as shown on Fig. 2.7, the short wavelength shear Alfven wave under consideration has short perpendicular

wavelength which is comparable to the electron inertial length ($k_x \gg k_z, k_x c/\omega_{pH} \sim 100, \lambda_x \sim 3c/\omega_{pe}$, where λ_x is projection of wavelength in X direction). This could also be seen from the wave dispersion relation Eq. (2.13), which incorporates finite electron inertia effects through including the electron plasma frequency ω_{pe} term. Correspondingly, we also need to incorporate the electron inertia effects in the hybrid computation to correctly model the generation and evolution of the short wavelength shear Alfven waves. This is achieved by assuming the electrons as a finite mass fluid. The detailed modification of the classical hybrid model is discussed in chapter 3.

2.2.4 Pitch angle scattering of relativistic electrons by shear Alfven waves

The general theory of pitch angle scattering of energetic electrons has been applied to study whistler and electromagnetic waves [4, 26, 38] as a source for inducing pitch angle scattering in the radiation belt environment. In our work, the source of scattering will be focused on the turbulence of longer wavelength shear Alfven waves due to the nonlinear evolution of the initially generated short wavelength shear Alfven waves.

The resonance condition of the wavenumbers for the pitch angle scattering can be shown as [15]:

$$\frac{k_z v_z}{\omega_{pH}} = \frac{k_z c \cos\alpha}{\omega_{pH}} \approx \frac{\Omega_e/\omega_{pH}}{2E+1} \tag{2.18}$$

where E is the electron kinetic energy in MeV. Ω_e is the electron cyclotron frequency and the relativistic electron speed along the magnetic field is $v_z \approx c\cos\alpha$, α is pitch angle. Applying the parameters at $L = 2$, the right-hand side of Eq. (2.18) is approximately 3.5 for a 2 MeV electron. Assuming the maximum wavenumber $k_z v_z/\omega_{pH}$ is around 5 and a moderate pitch angle α, the parallel wavenumbers could meet the resonance condition for a wide range of energetic electrons.

As described in pitch angle scattering of section 2.1.2, the $\vec{v} \times \vec{B}$ force changes the electron velocity in Z direction and hence the pitch angle α, since $\delta v_z = -v\sin\alpha\delta\alpha$ in cylindrical coordinates. Ref. [15] shows that the change of pitch angle could be expressed as:

$$\Delta\alpha^2(\gamma_R) = \frac{4\Omega_e/\gamma_r T_t L_z L_\phi L R_E}{4\pi(B_0^2/8\pi)(LR_E)^3} \frac{2\Delta L_z(\gamma_R)}{L_z} \frac{W_2}{1 + k_z^2 c^2/\omega_{pH}^2} \tag{2.19}$$

where $\gamma_R = 2E + 1$. T_t is the turbulence lifetime, L_z, L_ϕ are dimensions of turbulence cloud along the magnetic field and in the azimuthal direction, respectively. R_E is the Earth radius and $2\Delta L_z(\gamma_R)/L_z$ is the fraction of electron trajectory over which the resonance condition is satisfied. As shown in Eq. (2.19), the change in pitch angle depends on the energy deposited into the waves, i.e. the magnetic part of the wave energy density $W_2/(1 + k_z^2 c^2/\omega_{pH}^2)$. Note

that in the nonlinear evolution, the wave energy is equally partitioned in the fluctuating fields and particles. Therefore, $W_2/(1 + k_z^2 c^2/\omega_{pH}^2)$ is large enough for a sufficient pitch angle change. On the other hand, the initial highly oblique shear Alfven waves have most of energy stored in the particles and the magnetic part of wave energy is too small to make an efficient resonant scattering. Ref. [15] estimates that in the environment of $L = 2$, for 2 MeV electrons, $\Delta\alpha^2 \approx 20\eta$, where η is the fraction of the free energy released which goes into the longer wavelength part of the turbulence. With a few percent of the energy deposited in the turbulence as shown in the simulation results in chapter 4, a change in pitch angle of order of unity (in radian) could be achieved and this is large enough to scatter the trapped relativistic electrons into the loss cone.

Chapter 3

Numerical methods

In this chapter, we first describe the modified hybrid model for the generation and nonlinear evolution of the short wavelength shear Alfven waves, followed by an overview of the spectral method and finite difference method used to solve the modified electron momentum equation. We then discuss the time integration methods used to solve the temporal dependence of the field equations. After that the particle-in-cell (PIC) techniques for the kinetic ions are introduced along with the mesh configuration and boundary condition. Last, we consider how the distribution function is initialized and the hybrid model is normalized in the simulation.

3.1 Modified hybrid model

In this section, we describe the main features of the newly developed magnetized two-dimensional electromagnetic hybrid model used for studying the generation and development of the perpendicular propagating shear Alfven waves. Three species, as described in section 2.2.2, are included in the model. Again, these are ambient hydrogen and electrons and also the ionized release species ion which will be taken to be lithium. To model the plasma dynamics, the model uses particle ions and fluid electrons with finite electron inertia effects included. The hydrogen ions are initialized with a Maxwellian velocity distribution while the lithium ions are initialized with a standard ring velocity distribution in the plane perpendicular to the background magnetic field $\vec{B}_0$. We will discuss the initialization of the ion distribution function later in this chapter. The neutral lithium ionization process is not included in the current version of the model although it is relatively straightforward. It has been shown that this is a reasonable assumption [15] since the creation time of the ring plasma is shorter than the time for the ring plasma to release its energy to plasma waves. The relativistic particle electrons are not included in the current model either, therefore, the pitch angle scattering process could not be investigated numerically. However, the current model is capable of evaluating the amount of energy deposited in the turbulence during

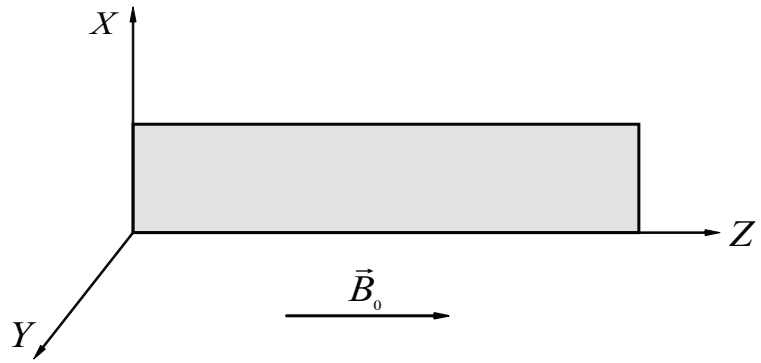

Figure 3.1: Schematic of simulation geometry in the $X - Z$ plane. Note that the domain is elongated along the magnetic field.

nonlinear process and it could be utilized to estimate the pitch angle scattering efficiency through the theoretical model described in section 2.2.4. Figure 3.1 shows the configuration of the simulation domain ($X - Z$ plane, where the background magnetic field is along the Z direction). Note that since the perpendicular propagating shear Alfven waves has $k_x \gg k_z$, the length of X direction is much shorter than the length of Z direction in order to well resolve k_x, and the simulation domain is elongated along the magnetic field.

The electromagnetic fields are treated with a low frequency approximation and thus the displacement current is neglected in Ampere's law [52]. Therefore Faraday's and Ampere's law become:

$$\vec{\nabla} \times \vec{E} = -\frac{1}{c}\frac{\partial \vec{B}}{\partial t} \tag{3.1}$$

$$\vec{\nabla} \times \vec{B} = \frac{4\pi}{c}\vec{J} \tag{3.2}$$

To treat the plasma ignoring effects on the electron Debye length scale, quasi-neutrality is imposed by setting:

$$q_i n_i - e n_e = 0 \Longrightarrow n_e = n_i = n_H + n_{Li} \tag{3.3}$$

where subscript e and q_i denote the electron charge and ion charge, respectively, and they are equal in our model. n_i is the total ion number density calculated from the PIC part. The other Maxwell's equations, e.g., Poisson's equation, $\vec{\nabla} \cdot \vec{E} = 4\pi e(n_i - n_e)$, is satisfied by virtue of the quasi-neutral approximation Eq. (3.3) and boundary conditions (which is discussed in section 3.6); likewise $\vec{\nabla} \cdot \vec{B} = 0$ is also satisfied. Also, because of quasi-neutrality, Eq. (3.2) could be rewritten as:

$$\vec{\nabla} \times \vec{B} = \frac{4\pi}{c} e n_i (\vec{v}_i - \vec{v}_e) \tag{3.4}$$

which could be used to find $\vec{v}_e$ from $\vec{v}_i$, the ion flow velocity determined from the PIC method [3]. Here $\vec{v}_i = (\vec{\Gamma}_H + \vec{\Gamma}_{Li})/n_i$, $\vec{\Gamma}_H$ and $\vec{\Gamma}_{Li}$ are hydrogen and lithium fluxes, respectively.

To be consistent with the hybrid model, the ions are treated kinetically, using standard PIC techniques. Each simulation macro-particle (charge q_p, mass m_p) is subject to the standard equations of motion:

$$m_p \frac{d\vec{v}_p}{dt} = q_p(\vec{E} + \frac{\vec{v}_p \times \vec{B}}{c}) - q_p \eta \vec{J} \tag{3.5}$$

$$\frac{d\vec{x}_p}{dt} = \vec{v}_p \tag{3.6}$$

where subscript p denotes a macro-particle representing a group of ions. The physical meaning of the last term of Eq. (3.5) will be shown shortly. $\vec{E}$, $\vec{B}$ and $\vec{J}$, which have values given on a spatial grid, are interpolated to the particle location. The updated particle information is then collected at the grid points to determine the ion number density n_i and ion flow velocity v_i. The detailed PIC techniques on ion dynamics will be addressed in section 3.7.

As motioned in section 2.2.3, in order to eliminate kinetic electron effects, the classical hybrid model treat electrons as a massless fluid ($m_e = 0$). The electron momentum equation is thus [7]:

$$m_e n_e \frac{d\vec{v}_e}{dt} = 0 = -en_e(\vec{E} + \frac{\vec{v}_e \times \vec{B}}{c}) - \vec{\nabla}\bar{\boldsymbol{P}}_{\boldsymbol{e}} + en_e\eta\vec{J} \tag{3.7}$$

where $\vec{v}_e$ is the electron fluid velocity and $\bar{\boldsymbol{P}}_{\boldsymbol{e}}$ is the electron pressure tensor. The last term in Eq. (3.7), which contains the current density $\vec{J}$ and resistivity η, represents both collisional effects between the electrons and ions and anomalous electron collisions with plasma turbulence [51]. The impact of such collisional processes will be accessed and discussed later in chapter 4. For momentum conservation, it requires adding $-e\eta\vec{J}$ to the acceleration term in the ion particle equation of motion Eq. (3.5) as well.

Since the model is to describe the generation and evolution of the short wavelength shear Alfven waves which has electron inertia spatial scale as described in section 2.2.3, we need to incorporate the electron inertia effect [11, 50] in the model through introducing finite electron mass fluid in electron momentum Eq. (3.7), and the modified momentum equation becomes:

$$m_e n_e \frac{d\vec{v}_e}{dt} = -en_e(\vec{E} + \frac{\vec{v}_e \times \vec{B}}{c}) + en_e\eta\vec{J} \tag{3.8}$$

The pressure term is neglected in Eq. (3.8) because the plasma considered has a very low $\beta = \frac{nKT}{B^2/8\pi}$ and the pressure force only has insignificant impact on the physics. Note the fact

that $n_e\vec{v}_e = n_i\vec{v}_i - \frac{\vec{J}}{e}$, and we can use ion flow velocity v_i to substitute electron fluid velocity v_e. By manipulating Eq. (3.1, 3.3, 3.4) and take advantage of electron continuity equation $\frac{\partial n_e}{\partial t} + \vec{\nabla}\cdot(n_e\vec{v}_e) = 0$ and ion momentum equation $\frac{\partial \vec{v}_i}{\partial t} + (\vec{v}_i\cdot\vec{\nabla})\vec{v}_i = \frac{e}{m_i}\vec{E} + \frac{e\vec{v}_i\times\vec{B}}{cm_i} - \frac{e\eta}{m_i}\vec{J}$ to eliminate time derivatives [9, 22], the electron momentum equation (3.8) can be rewritten as:

$$\begin{aligned}
&\frac{c^2}{4\pi}(\vec{\nabla}(\vec{\nabla}\cdot\vec{E}) - \nabla^2\vec{E}) + \frac{e^2 n_i}{m_e}\vec{E} \\
&= -\frac{n_i e^2}{cm_e}(\vec{v}_i\times\vec{B}) + \frac{e}{4\pi m_e}(\vec{\nabla}\times\vec{B})\times\vec{B} + \frac{ce^2 n_i\eta}{4\pi m_e}(\vec{\nabla}\times\vec{B}) \\
&+ \frac{c}{4\pi}(\vec{v}_i\cdot\vec{\nabla})(\vec{\nabla}\times\vec{B}) - \frac{c^2}{16\pi^2 e n_i}((\vec{\nabla}\times\vec{B})\cdot\vec{\nabla})(\vec{\nabla}\times\vec{B}) \\
&+ \frac{c}{4\pi}((\vec{\nabla}\times\vec{B})\cdot\vec{\nabla})\vec{v}_i \\
&+ \frac{c}{4\pi}(\vec{\nabla}\cdot\vec{v}_i)(\vec{\nabla}\times\vec{B}) + \frac{c^2}{16\pi^2 e n_i^2}(\vec{\nabla}\times\vec{B})((\vec{\nabla}\times\vec{B})\cdot\vec{\nabla})n_i
\end{aligned} \tag{3.9}$$

The detailed derivation of Eq. (3.9) is given in Appendix A. From the right-hand side of Eq. (3.9), we could see several nonlinear terms. These nonlinear terms are essential for modeling the evolution of shear Alfven waves in the turbulence state. The advantage of Eq. (3.9) is that it incorporates the finite electron inertia without containing an explicit time derivative. In general, one could use Eq. (3.9) to solve for electric field equation and use Eq. (3.1) to time advance the whole electromagnetic field. The time integration methods are discussed in detail in section 3.4.

However, the challenge of this model comes from the fact that the dispersion relation Eq. (2.8) for the waves requires $\vec{\nabla}\cdot\vec{E} \neq 0$ in Eq. (3.9) while at the same time the quasi-neutral assumption which indicates $\vec{\nabla}\cdot\vec{E} = 4\pi e(n_i - n_e) \approx 0$ must be maintained. Naively solving Eq. (3.9) explicitly may introduce numerical inaccuracies into the simulation due to the direct violation of the Poisson's equation $\vec{\nabla}\cdot\vec{E} = 4\pi e(n_i - n_e)$. Thus, solving the field equation which has $\vec{\nabla}\cdot\vec{E}$ term must be avoided. The method presented here is to separate electric field into transverse $\vec{E}_t$ and longitudinal $\vec{E}_l = -\vec{\nabla}\phi_e$ components (where ϕ_e is the electric scalar potential) and take advantage of their identities [18] :

$$\begin{aligned}
&\because \vec{\nabla}\times\vec{E}_l = 0, \vec{\nabla}\cdot\vec{E}_t = 0 \\
&\therefore \vec{\nabla}(\vec{\nabla}\cdot\vec{E}) - \nabla^2\vec{E} \\
&= \vec{\nabla}\times(\vec{\nabla}\times\vec{E}) = \vec{\nabla}\times(\vec{\nabla}\times(\vec{E}_l + \vec{E}_t)) \\
&= \vec{\nabla}\times(\vec{\nabla}\times\vec{E}_t) = \vec{\nabla}(\vec{\nabla}\cdot\vec{E}_t) - \nabla^2\vec{E}_t = -\nabla^2\vec{E}_t
\end{aligned} \tag{3.10}$$

Applying the above identity to Eq. (3.9), the transverse electric field equation can be obtained

as:

$$
\begin{aligned}
&-\frac{c^2}{4\pi}\nabla^2\vec{E}_t+\frac{e^2n_i}{m_e}\vec{E}_t\\
&=-\frac{n_ie^2}{cm_e}(\vec{v}_i\times\vec{B})+\frac{e}{4\pi m_e}(\vec{\nabla}\times\vec{B})\times\vec{B}+\frac{ce^2n_i\eta}{4\pi m_e}(\vec{\nabla}\times\vec{B})\\
&+\frac{c}{4\pi}(\vec{v}_i\cdot\vec{\nabla})(\vec{\nabla}\times\vec{B})-\frac{c^2}{16\pi^2en_i}((\vec{\nabla}\times\vec{B})\cdot\vec{\nabla})(\vec{\nabla}\times\vec{B})\\
&+\frac{c}{4\pi}((\vec{\nabla}\times\vec{B})\cdot\vec{\nabla})\vec{v}_i\\
&+\frac{c}{4\pi}(\vec{\nabla}\cdot\vec{v}_i)(\vec{\nabla}\times\vec{B})+\frac{c^2}{16\pi^2en_i^2}(\vec{\nabla}\times\vec{B})((\vec{\nabla}\times\vec{B})\cdot\vec{\nabla})n_i-\frac{e^2n_i}{m_e}\vec{E}_l
\end{aligned}
\tag{3.11}
$$

and the longitudinal field equation which is written in terms of the electric potential $\vec{E}_l = -\vec{\nabla}\phi_e$:

$$
\begin{aligned}
&\nabla^2\phi_e+\frac{1}{n_i}(\vec{\nabla}n_i\cdot\vec{\nabla}\phi_e)\\
&=\frac{1}{c}(\vec{B}\cdot(\vec{\nabla}\times\vec{v}_i)-\vec{v}_i\cdot(\vec{\nabla}\times\vec{B}))+\frac{1}{cn_i}(\vec{v}_i\times\vec{B})\cdot\vec{\nabla}n_i\\
&+\frac{1}{4\pi en_i}(\vec{B}\cdot\nabla^2\vec{B}+(\vec{\nabla}\times\vec{B})\cdot(\vec{\nabla}\times\vec{B}))-\frac{c\eta}{4\pi n_i}(\vec{\nabla}\times\vec{B})\cdot\vec{\nabla}n_i+\frac{1}{n_i}(\vec{\nabla}n_i\cdot\vec{E}_t)\\
&-\frac{cm_e}{4\pi e^2n_i}((\vec{\nabla}\times\vec{B})\cdot(\vec{\nabla}(\vec{\nabla}\cdot\vec{v}_i))+\vec{\nabla}\cdot((\vec{v}_i\cdot\vec{\nabla})(\vec{\nabla}\times\vec{B})+(\vec{\nabla}\times\vec{B}\cdot\vec{\nabla})\vec{v}_i))\\
&+\frac{c^2m_e}{16\pi^2e^3n_i^2}\vec{\nabla}\cdot((\vec{\nabla}\times\vec{B}\cdot\vec{\nabla})(\vec{\nabla}\times\vec{B}))\\
&-\frac{c^2m_e}{16\pi^2e^3n_i^3}(\vec{\nabla}\times\vec{B})\cdot((\vec{\nabla}\times\vec{B}\cdot\vec{\nabla})(\vec{\nabla}n_i)+(\vec{\nabla}n_i\cdot\vec{\nabla})(\vec{\nabla}\times\vec{B})-\vec{\nabla}n_i\times\nabla^2\vec{B})\\
&-\frac{c^2m_e}{16\pi^2e^3n_i^3}\vec{\nabla}n_i\cdot((\vec{\nabla}\times\vec{B}\cdot\vec{\nabla})(\vec{\nabla}\times\vec{B}))\\
&+\frac{c^2m_e}{8\pi^2e^3n_i^4}((\vec{\nabla}\times\vec{B})\cdot\vec{\nabla}n_i)^2
\end{aligned}
\tag{3.12}
$$

The derivation of separating the electric field equations can be found in Appendix A. A standard pseudo-spectral method [6] or a finite difference method (e.g., preconditioned conjugate gradient (PCG) method) can be applied to solve Eq. (3.11) and Eq. (3.12). In addition, an iterative procedure is required for calculating $\vec{E}_t$ and $\vec{E}_l$ since the two equations are coupled. The numerical methods used to solve the electric field equations are described in the following sections.

3.2 Spectral method

In this section, we focus on the spectral method we are using, the pseudo-spectral method, and the application of this method to solve the electric field equation (3.11) and (3.12). Spectral methods, in general, are based on representing the solution to a partial differential equation (PDE) as a truncated series of a smooth function of the dependent variable [6]. The advantages of spectral method are its accuracy and its ability to handle nonlinear PDEs as it could transform partial derivatives to ordinary multiplication operations although its computation time is more costly comparing with that of finite difference method. Three most commonly used spectral schemes are: Galerkin, collocation and tau. Among the three schemes, the collocation approach is the simplest method. However, it requires the periodic boundary condition. The differential equation and the boundary condition then has to be satisfied exactly at the collocation points which are usually the same as the physical grid points. The earliest application of the spectral collocation method to PDEs was made for spatially periodic problems by Orszag [33] who termed it pseudo-spectral method. Our computational model allows us to use periodic boundary conditions. Thus, from now on we will only be concerned with the pseudo-spectral method.

3.2.1 Fourier transform

The common method of applying spectral techniques to equations that depend on space or time is to work in Fourier domain as a function of wavenumber or frequency, using Fourier transforms on the space and time variable. This is a well known technique which provides for a reliable solution to problems with periodic functions. Any physical process can be described either in the physical space domain, by the values of some quantity u as a function of physical space x, e.g., $u(x)$, or else in Fourier domain, where the process is specified by giving its amplitude U as a function of wavenumber k, that is $U(k)$, with $-\infty < k < \infty$. To go back and forth between two domains, the 1D Fourier and inverse Fourier transform equations are introduced [36]:

$$U(k) = \int_{-\infty}^{\infty} u(x) e^{-ikx} dx \tag{3.13}$$

$$u(x) = \frac{1}{2\pi} \int_{-\infty}^{\infty} U(k) e^{ikx} dk \tag{3.14}$$

These equations are continuous and in computational applications, we have to use the discretized version of the Fourier transform. A common situation is to have a function sampled at evenly spaced discrete intervals, Δx. For any sampling interval Δx, the Nyquist critical wavenumber is given by:

$$k_c = \frac{1}{2\Delta x} \tag{3.15}$$

This lead to an important theorem for discrete sampling known as the sampling theorem: If a continuous function $u(x)$, sampled at an interval Δx, is bandwidth limited to wavenumbers smaller in magnitude than k_c, then the function $u(x)$ is completely determined by its samples u_n. The sampling theorem is significant because it allows for the entire information content of a signal to be reproduced provided it is sampled at sufficient rate. Suppose we have an even function of $N+1$ consecutive samples:

$$u_j \equiv u(x_j), x_j = j\Delta x, j = 0, 1, 2, ..., N \tag{3.16}$$

such that the sampling interval is Δx, the set of points x_j are referred to as nodes or grid points and the period of the quantity u_j is just the domain length $N\Delta x$. The wavenumber is defined as:

$$\mathrm{k_n} = \frac{2\pi n}{N\Delta x}, \text{where mode number } n = -\frac{N}{2}, ..., 0, ..., \frac{N}{2} \tag{3.17}$$

The discrete Fourier transform (DFT) is of the $N+1$ points u_j, denoted by U_n

$$U_n = \sum_{j=0}^{N} u_j e^{-i\mathrm{k_n}x_j} = \sum_{j=0}^{N} u_j e^{-i\frac{2\pi n}{N}j} \tag{3.18}$$

Likewise, the formula for the inverse discrete Fourier transform can be derived as:

$$u_j = \frac{1}{N}\sum_{n=-N/2}^{N/2} U_n e^{i\mathrm{k_n}x_j} = \frac{1}{N}\sum_{n=-N/2}^{N/2} U_n e^{i\frac{2\pi n}{N}j} \tag{3.19}$$

Similar to the one-dimensional case, we define the two-dimensional DFT and inverse DFT as following [6]:

$$U_{n_x,n_y} = \sum_{j_x=0}^{N_x}\sum_{j_y=0}^{N_y} u_{j_x,j_y} e^{-i\mathrm{k_{n_x}}x_{j_x}} e^{-i\mathrm{k_{n_y}}y_{j_y}} \tag{3.20}$$

$$u_{j_x,j_y} = \frac{1}{N_x}\frac{1}{N_y}\sum_{n_x=-N_x/2}^{N_x/2}\sum_{n_y=-N_y/2}^{N_y/2} U_{n_x,n_y} e^{i\mathrm{k_{n_x}}x_{j_x}} e^{i\mathrm{k_{n_y}}y_{j_y}} \tag{3.21}$$

where $\mathrm{k_{n_x}} = \frac{2\pi n_x}{N\Delta x}, \mathrm{k_{n_y}} = \frac{2\pi n_y}{N\Delta y}$ are corresponding wavenumbers in $\hat{\mathbf{k}}_\mathbf{x}$ and $\hat{\mathbf{k}}_\mathbf{y}$ direction, respectively, and $x_{j_x} = j_x\Delta x$, $y_{j_y} = j_y\Delta y$ are discrete grid points. Here $n_x = -\frac{N_x}{2}, ..., \frac{N_x}{2}; n_y = -\frac{N_y}{2}, ..., \frac{N_y}{2}; j_x = 0, 1, ..., N_x; j_y = 0, 1, ..., N_y$

For 1D case, the DFT maps $N+1$ complex number U_n into $N+1$ complex numbers u_j. As the number of input data points increases, the output frequency spectrum becomes closer to continuous spectrum. The amount of computation involved in computing an N-point

DFT is $O(N^2)$ process. With N getting bigger, the computational time will be dramatically increased. In modern scientific computing (also in this thesis), a far more efficient algorithm known as fast Fourier transform (FFT) which is derived from DFT is usually applied instead of DFT. The basis idea of FFT is that a DFT of length N can be expressed as the sum of two DFTs, each of length $N/2$, cutting the processing time in half. This process can be repeated recursively on the DFT of the length $N/2$ and so on until only two components left. The computational time for an N-point FFT is $O(\log_2^N)$, which is much more efficient comparing with DFT when dealing with a larger N. However, it is usually necessary that N be an integer power of 2 for a FFT in order to do binary manipulation. The detailed derivation of the FFT algorithm can be found in Ref. [36].

3.2.2 Differentiation

In Fourier space, differentiation is simply a matter of multiplying each Fourier quantity with the imaginary unit times the corresponding wavenumber. In two dimensional space, this could be expressed analytically by

$$F\left\{\frac{\partial u(x,y)}{\partial x}+\frac{\partial u(x,y)}{\partial y}\right\}=i\vec{k}U(k) \tag{3.22}$$

where F represents the Fourier Transform operation and $\vec{k}=k_x\hat{\mathbf{k}}_\mathbf{x}+k_y\hat{\mathbf{k}}_\mathbf{y}$ is the wavenumber. Eq. (3.22) are for continuous transform, which is the true spectral derivative referred as Fourier Galerkin derivative. We can also extend the analysis of derivative operations to that of Laplacian, which for 2-D is:

$$\nabla^2=\frac{\partial^2}{\partial^2 x}+\frac{\partial^2}{\partial^2 y} \tag{3.23}$$

In the Fourier space, the Laplacian operator becomes a multiplication of each Fourier quantity with $-k^2$, where $k^2=k_x^2+k_y^2$ in 2-D.

In performing derivatives and Laplacians on a discrete grid, $\vec{k}$ and k^2 are replaced by $\vec{\mathrm{k}}_\mathrm{n}$ and k_n^2, respectively [3], where

$$\vec{\mathrm{k}}_\mathrm{n}=\mathrm{k}_{\mathrm{n_x}}\left[\frac{\sin(\mathrm{k}_{\mathrm{n_x}}\Delta x)}{\mathrm{k}_{\mathrm{n_x}}\Delta x}\right]\hat{\mathbf{k}}_\mathbf{x}+\mathrm{k}_{\mathrm{n_y}}\left[\frac{\sin(\mathrm{k}_{\mathrm{n_y}}\Delta y)}{\mathrm{k}_{\mathrm{n_y}}\Delta y}\right]\hat{\mathbf{k}}_\mathbf{y} \tag{3.24}$$

and

$$\mathrm{k}_\mathrm{n}^2=\mathrm{k}_{\mathrm{n_x}}^2\left[\frac{\sin(\frac{\mathrm{k}_{\mathrm{n_x}}\Delta x}{2})}{\frac{\mathrm{k}_{\mathrm{n_x}}\Delta x}{2}}\right]^2+\mathrm{k}_{\mathrm{n_y}}^2\left[\frac{\sin(\frac{\mathrm{k}_{\mathrm{n_y}}\Delta y}{2})}{\frac{\mathrm{k}_{\mathrm{n_y}}\Delta y}{2}}\right]^2 \tag{3.25}$$

where the definition of $\mathrm{k}_{\mathrm{n_x}}$ and $\mathrm{k}_{\mathrm{n_y}}$ are same as described in section 3.2.1. This discreteness effect can be explained by considering the derivative operator and the Laplacian operator

(in 1D for simplicity) as

$$\frac{du(x)}{dx} \longrightarrow \frac{u(x+\Delta x) - u(x-\Delta x)}{2\Delta x} \tag{3.26}$$

$$\frac{d^2u(x)}{dx} \longrightarrow \frac{u(x+\Delta x) - 2u(x) + u(x-\Delta x)}{\Delta x^2} \tag{3.27}$$

obtained by finite differencing [6]. Then substituting Eq. (3.18) into the Fourier transform of Eq. (3.26) and (3.27) and specializing them for the 2-D case, we obtain the results in Eq. (3.24) and (3.25). As the grid becomes finer, $\vec{\mathrm{k}}_\mathrm{n}$ and k_n^2 approach the continuous result $\vec{k}$ and k^2, respectively.

3.2.3 Convolution

Nonlinear terms such as those found in Eq. (3.11) and (3.12) need a careful treatment by the spectral method. This is due to the property of the Fourier transform which states that products in real space give rise to convolution in Fourier space. Thus, we need a specific method that can evaluate Fourier-space convolution effectively and accurately.

Consider the evaluation of the one-dimensional convolution for discrete cases:

$$W(k) = U(k) \otimes V(k) \Longrightarrow W_n = \sum_{p+q=n} U_p V_q, \quad -\frac{N}{2} \leq n, q \leq \frac{N}{2} \tag{3.28}$$

where $\otimes$ denotes convolution. W_n, U_p and V_q are discrete Fourier quantity and p, q, n denote the Fourier mode numbers. Direct summation of Eq. (3.28) takes $O(N^2)$ operations in one dimension, and the number of operations will become extremely large as we go to higher dimensions and larger N. Therefore, doing direction evaluation of Eq. (3.28) for convolution in Fourier domain is not very efficient. The reason that makes direct evaluation of Eq. (3.28) inefficient is their nonlocality: W_n depends on U_p and V_q for $\max(n - N/2, -N/2) < p < \min(n + N/2, N/2)$.

Fortunately, this nonlocality can be avoided by using suitable inverse Fourier transform to express $W(k)$ as local product of inverse-Fourier-transformed fields, since the convolution in Fourier space equals the Fourier transform of products in real space. Orszag [32] was the fist to develop this pseudo-spectral method. The approach is to use inverse FFT to transform U_p and V_p to u_j and v_j in physical space. Since u_j and v_j are defined at exactly on the $N+1$ grid point, we can define w_j as the local product $u_j v_j$ of the physical space fields, and then use the FFT to return to the Fourier space. The overall convolution sequence can be summarized by:

$$U_p, V_q \xrightarrow{IFFT} u_j, v_j \xrightarrow{\times} w_j \xrightarrow{FFT} W_n \tag{3.29}$$

We find that

$$\begin{aligned}\hat{W}_n &= \sum_{j=0}^{N} w_j e^{-i\frac{2\pi n}{N}j} = \sum_{j=0}^{N} u_j v_j e^{-i\frac{2\pi n}{N}j} \\ &= \frac{1}{N^2}\sum_{j=0}^{N}\sum_{|p|\le N/2} U_p e^{i\frac{2\pi p}{N}j} \sum_{|q|\le N/2} V_q e^{i\frac{2\pi q}{N}j} e^{-i\frac{2\pi n}{N}j} \\ &= \sum_{|p|,|q|\le N/2} U_p V_q \frac{1}{N^2}\sum_{j=2}^{2} w_j e^{i\frac{2\pi}{N}(p+q-n)j} \end{aligned} \tag{3.30}$$

where $\hat{W}_n$ is the aliased convolution sum, Using the discrete transform orthogonality relations [32], Eq. (3.30) can be rewritten as

$$\hat{W}_n = \sum_{p+q=n} U_p V_q + \sum_{p+q=n\pm N} U_p V_q = W_n + \sum_{p+q=n\pm N} U_p V_q \tag{3.31}$$

where W_n is the true convolution term given in Eq. (3.28). The second term on the right-hand side of Eq. (3.31) originates from the property that $\exp[i\frac{2\pi}{N}(n \pm N)j] = \exp[i\frac{2\pi}{N}nj]$ for all integral j in a periodic system $N\Delta x$ such that the discrete grid points $x_j = j\Delta x$ cannot distinguish the wave vector $\mathrm{k_n} = \frac{2\pi n}{N\Delta x}$ and its alias $\mathrm{k_{n\pm N}} = \frac{2\pi(n\pm N)}{N\Delta x}$, $\mathrm{k_{n\pm 2N}} = \frac{2\pi(n\pm 2N)}{N\Delta x}$ etc. For any $n < N/2$, there always exists a nonzero aliasing error. Eq. (3.31)) is applicable only for one-dimensional case. Derivation for higher dimension cases, although is much more involved, is similar to that of the one-dimensional case. In three dimensions, in addition to the singly-aliased term on the right-hand side of Eq. (3.31)), there are two other singly-aliased contributions, three doubly-aliased terms and one triply-aliased contribution. Aliasing errors usually, but not always, lead to numerical instabilities; they, however, always lead to inaccuracies, especially for high n modes. Therefore, in order to eliminate the aliasing terms, we apply the phase shifting method to compute Eq. (3.31).

Aliasing removal by phase shifting

The discrete transform of Eq. (3.19) can be redefined as a phase shift transform:

$$\tilde{u}_j = \frac{1}{N}\sum_{n=-N/2}^{N/2} U_n e^{i\mathrm{k_n}(x_j+\Delta)} \tag{3.32}$$

$$\tilde{v}_j = \frac{1}{N}\sum_{n=-N/2}^{N/2} V_n e^{i\mathrm{k_n}(x_j+\Delta)} \tag{3.33}$$

which are just the transform on a grid shifted by the factor Δ in physical space. We then compute the local product of $\tilde{u}_j\tilde{v}_j$ and inverse transform it back to the Fourier space. The result of the convolution of the shifted grid is:

$$\tilde{W}_n = \sum_{j=0}^{N} \tilde{u}_j\tilde{v}_j e^{-i\mathrm{k_n}(x_j+\Delta)} \tag{3.34}$$

while the results for the unshifted grid in give in Eq. (3.30). With some manipulations, and letting $\Delta = \Delta x/2$, i.e., shift of half a grid cell, we find that the true convolution term can be expressed as:

$$W_n = \frac{1}{2}(\hat{W}_n + \tilde{W}_n) - \sum_m W_{n+Nm} \tag{3.35}$$

where $m = (m_1, m_2, m_3)$ have one zero component and two components independently ± 1. Patterson [35] and Orszag [31] have shown that using these two types of grid shifted by a half grid cell eliminates all the singly- and triply-aliased terms. And if the set of allowable modes used in the convolution sum is reduced, there will not be any modes that contribute to the doubly-aliased terms. This aliasing removal technique is applied in the spectral method whenever encountering convolution in our work.

3.2.4 Spectral filtering

To eliminate numerical noises and unreliable high mode number structures which might otherwise lead to numerical instabilities, a spectral filter in Fourier domain is applied [3]. Spectral filter is simply, just multiplying each mode value by the corresponding attenuating factor $SM(\vec{k})$:

$$SM(\vec{k}) = \exp(-\alpha^N) \tag{3.36}$$

where $\alpha = \vec{k}/k_{last}$, k_{last} is the mode number that the amplitude of this mode is attenuated to $\frac{1}{e}$ of its original value and N is the coefficient to specify the shape of attenuating, i.e., smooth or not. The one-dimensional form $SM(\vec{k})$ is plotted in Fig. 3.2. This filter attenuates the short wavelengths (high n modes). By specifying k_{last} and N, we could choose the shape of filter that is able to best truncate the unwanted Fourier modes. In the simulation cases shown in chapter 4, we specify k_{last}=32 and N=0.5 as a standard spectral filter paramters.

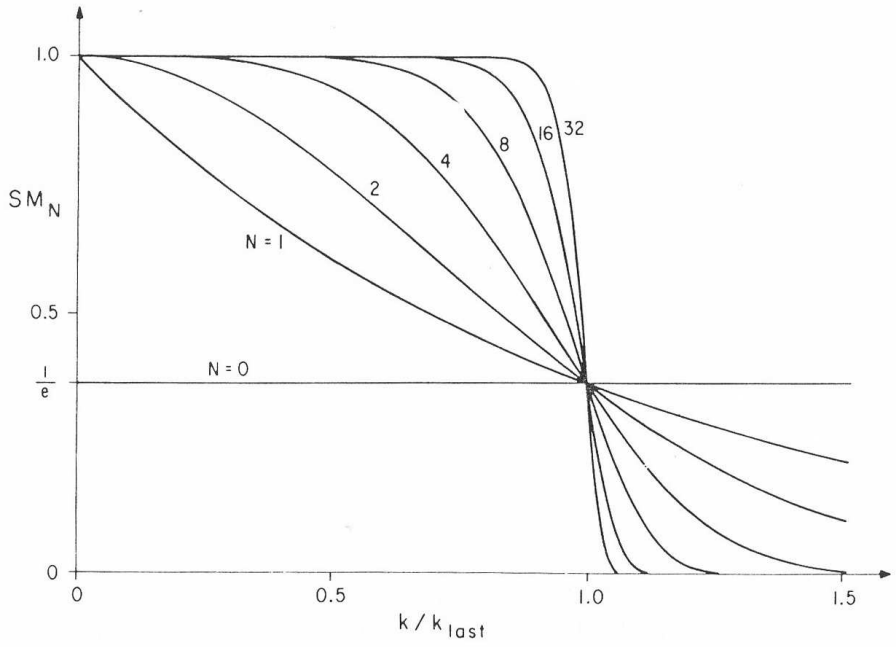

Figure 3.2: Spectral filter $SM(\vec{k}) = \exp(-\alpha^N)$ for various values of N [3].

3.2.5 Electric field equations in the Fourier space

Based on the spectral method described in previous sections, we now apply the spectral method on solving the electric field equations (3.11) and (3.12). Taking two-dimensional case $(X - Y)$ as an example, the longitudinal electric field equation (3.12) can be rewritten as:

$$
\begin{aligned}
&(\frac{\partial^2}{\partial x^2}+\frac{\partial^2}{\partial y^2})\phi_e \\
&=\frac{1}{c}(B_x\frac{\partial v_{iz}}{\partial y}-B_y\frac{\partial v_{iz}}{\partial x}+B_z(\frac{\partial v_{iy}}{\partial x}-\frac{\partial v_{ix}}{\partial y})-v_{ix}\frac{\partial B_z}{\partial y}+v_{iy}\frac{\partial B_z}{\partial x}-v_{iz}(\frac{\partial B_y}{\partial x}-\frac{\partial B_x}{\partial y})) \\
&+\frac{1}{n_i}(\frac{\partial n_i}{\partial x}E_{tx}+\frac{\partial n_i}{\partial y}E_{ty}-\frac{\partial n_i}{\partial x}\frac{\partial \phi_e}{\partial x}-\frac{\partial n_i}{\partial y}\frac{\partial \phi_e}{\partial y} \\
&\quad+\frac{1}{c}(v_{iy}B_z-v_{iz}B_y)\frac{\partial n_i}{\partial x}+\frac{1}{c}(v_{iz}B_x-v_{ix}B_z)\frac{\partial n_i}{\partial y} \\
&\quad+\frac{1}{4\pi e}(B_x(\frac{\partial^2 B_x}{\partial x^2}+\frac{\partial^2 B_x}{\partial y^2})+B_y(\frac{\partial^2 B_y}{\partial x^2}+\frac{\partial^2 B_y}{\partial y^2})+B_z(\frac{\partial^2 B_z}{\partial x^2}+\frac{\partial^2 B_z}{\partial y^2}) \\
&\quad+\frac{\partial B_z}{\partial y}\frac{\partial B_z}{\partial y}+\frac{\partial B_z}{\partial x}\frac{\partial B_z}{\partial x}+(\frac{\partial B_y}{\partial x}-\frac{\partial B_x}{\partial y})(\frac{\partial B_y}{\partial x}-\frac{\partial B_x}{\partial y})) \\
&\quad-\frac{c\eta}{4\pi}(\frac{\partial B_z}{\partial y}\frac{\partial n_i}{\partial x}-\frac{\partial B_z}{\partial x}\frac{\partial n_i}{\partial y}) \\
&\quad-\frac{cm_e}{2\pi e^2}(\frac{\partial B_z}{\partial y}(\frac{\partial^2 v_{ix}}{\partial x^2}+\frac{\partial^2 v_{iy}}{\partial x\partial y})-\frac{\partial B_z}{\partial x}(\frac{\partial^2 v_{ix}}{\partial x\partial y}+\frac{\partial^2 v_{iy}}{\partial y^2}) \\
&\quad+\frac{\partial^2 B_z}{\partial x\partial y}(\frac{\partial v_{ix}}{\partial x}-\frac{\partial v_{iy}}{\partial y})+\frac{\partial^2 B_z}{\partial y^2}\frac{\partial v_{iy}}{\partial x}-\frac{\partial^2 B_z}{\partial x^2}\frac{\partial v_{ix}}{\partial y})) \\
&+\frac{1}{n_i^2}\frac{c^2m_e}{8\pi^2e^3}(\frac{\partial^2 B_z}{\partial x\partial y}\frac{\partial^2 B_z}{\partial x\partial y}-\frac{\partial^2 B_z}{\partial x^2}\frac{\partial^2 B_z}{\partial y^2}) \\
&+\frac{1}{n_i^3}\frac{c^2m_e}{16\pi^2e^3}(\frac{\partial B_z}{\partial y}(\frac{\partial B_z}{\partial y}\frac{\partial^2 n}{\partial x^2}-2\frac{\partial B_z}{\partial x}\frac{\partial^2 n}{\partial x\partial y})+\frac{\partial B_z}{\partial x}\frac{\partial B_z}{\partial x}\frac{\partial^2 n}{\partial y^2} \\
&\quad+2\frac{\partial B_z}{\partial y}(\frac{\partial n}{\partial x}\frac{\partial^2 B_z}{\partial x\partial y}-\frac{\partial n}{\partial y}\frac{\partial^2 B_z}{\partial x^2})+2\frac{\partial B_z}{\partial x}(\frac{\partial n}{\partial y}\frac{\partial^2 B_z}{\partial x\partial y}-\frac{\partial n}{\partial x}\frac{\partial^2 B_z}{\partial y^2}) \\
&\quad+(\frac{\partial B_y}{\partial x}-\frac{\partial B_x}{\partial y})(\frac{\partial n}{\partial y}(\frac{\partial^2 B_x}{\partial x^2}+\frac{\partial^2 B_y}{\partial x\partial y})-\frac{\partial n}{\partial x}(\frac{\partial^2 B_x}{\partial x\partial y}+\frac{\partial^2 B_y}{\partial y^2}))) \\
&+\frac{1}{n_i^4}\frac{c^2m_e}{8\pi^2e^3}(\frac{\partial B_z}{\partial y}\frac{\partial n}{\partial x}-\frac{\partial B_z}{\partial x}\frac{\partial n}{\partial y})(\frac{\partial B_z}{\partial y}\frac{\partial n}{\partial x}-\frac{\partial B_z}{\partial x}\frac{\partial n}{\partial y})
\end{aligned}
\tag{3.37}
$$

Assuming a periodic system, then the spatial variables may be transformed by using pseudo-spectral method as described in previous sections for solutions of the above equation. Again note that real space (x, y) is transformed to Fourier space (k_x, k_y) and subscript $\vec{k}$ denotes

Fourier domain quantity, where $k^2 = k_x^2 + k_y^2$. Therefore in the Fourier domain:

$$
\begin{aligned}
\phi_{e\vec{k}} = -\frac{1}{k_x^2+k_y^2}(& \\
&+ \frac{1}{c}(B_{x\vec{k}} \otimes (ik_y v_{iz\vec{k}}) - B_{y\vec{k}} \otimes (ik_x v_{iz\vec{k}}) + B_{z\vec{k}} \otimes (ik_x v_{iy\vec{k}} - ik_y v_{ix\vec{k}}) \\
&\quad - v_{ix\vec{k}} \otimes (ik_y B_{z\vec{k}}) + v_{iy\vec{k}} \otimes (ik_x B_{z\vec{k}}) - v_{iz\vec{k}} \otimes (ik_x B_{y\vec{k}} - ik_y B_{x\vec{k}})) \\
&+ (\frac{1}{n_i})_{\vec{k}} \otimes ((ik_x n_{i\vec{k}}) \otimes E_{tx\vec{k}} + (ik_y n_{i\vec{k}}) \otimes E_{ty\vec{k}} - (ik_x n_{i\vec{k}}) \otimes (ik_x \phi_{e\vec{k}}) - (ik_y n_{i\vec{k}}) \otimes (ik_y \phi_{e\vec{k}}) \\
&\quad + \frac{1}{c}(v_{iy}B_z - v_{iz}B_y)_{\vec{k}} \otimes (ik_x n_{i\vec{k}}) + \frac{1}{c}(v_{iz}B_x - v_{ix}B_z)_{\vec{k}} \otimes (ik_y n_{i\vec{k}}) \\
&\quad + \frac{1}{4\pi e}(B_{x\vec{k}} \otimes (-k_x^2 B_{x\vec{k}} - k_y^2 B_{x\vec{k}}) + B_{y\vec{k}} \otimes (-k_x^2 B_{y\vec{k}} - k_y^2 B_{y\vec{k}}) + B_{z\vec{k}} \otimes (-k_x^2 B_{z\vec{k}} - k_y^2 B_{z\vec{k}}) \\
&\quad + (ik_y B_{z\vec{k}}) \otimes (ik_y B_{z\vec{k}}) + (ik_x B_{z\vec{k}}) \otimes (ik_x B_{z\vec{k}}) + (ik_x B_{y\vec{k}} - ik_y B_{x\vec{k}}) \otimes (ik_x B_{y\vec{k}} - ik_y B_{x\vec{k}})) \\
&\quad - \frac{c\eta}{4\pi}((ik_y B_{z\vec{k}}) \otimes (ik_x n_{i\vec{k}}) - (ik_x B_{z\vec{k}}) \otimes (ik_y n_{i\vec{k}})) \\
&\quad - \frac{cm_e}{2\pi e^2}((ik_y B_{z\vec{k}}) \otimes (-k_x^2 v_{ix\vec{k}} - k_x k_y v_{iy\vec{k}}) - (ik_x B_{z\vec{k}}) \otimes (-k_x k_y v_{ix\vec{k}} - k_y^2 v_{iy\vec{k}}) \\
&\quad - k_x k_y B_{z\vec{k}} \otimes (ik_x v_{ix\vec{k}} - ik_y v_{iy\vec{k}}) - k_y^2 B_{z\vec{k}} \otimes (ik_x v_{iy\vec{k}}) + k_x^2 B_{z\vec{k}} \otimes (ik_y v_{ix\vec{k}}))) \\
&+ (\frac{1}{n_i^2})_{\vec{k}} \otimes (\frac{c^2 m_e}{8\pi^2 e^3}(k_x k_y B_{z\vec{k}} \otimes k_x k_y B_{z\vec{k}} - k_x^2 B_{z\vec{k}} \otimes k_y^2 B_{z\vec{k}})) \\
&+ (\frac{1}{n_i^3})_{\vec{k}} \otimes (\frac{c^2 m_e}{16\pi^2 e^3}((ik_y B_{z\vec{k}}) \otimes (-(ik_y B_{z\vec{k}}) \otimes k_x^2 n_{\vec{k}} + 2(ik_x B_{z\vec{k}}) \otimes k_x k_y n_{\vec{k}}) \\
&\quad - ((ik_x B_{z\vec{k}}) \otimes (ik_x B_{z\vec{k}})) \otimes k_y^2 n_{\vec{k}} \\
&\quad + 2(ik_y B_{z\vec{k}}) \otimes (-(ik_x n_{\vec{k}}) \otimes k_x k_y B_{z\vec{k}} + (ik_y n_{\vec{k}}) \otimes k_x^2 B_{z\vec{k}}) \\
&\quad + 2(ik_x B_{z\vec{k}}) \otimes (-(ik_y n_{\vec{k}}) \otimes k_x k_y B_{z\vec{k}} + (ik_x n_{\vec{k}}) \otimes k_y^2 B_{z\vec{k}}) \\
&\quad + (ik_x B_{y\vec{k}} - ik_y B_{x\vec{k}}) \otimes (-(ik_y n_{\vec{k}}) \otimes (k_x^2 B_{x\vec{k}} + k_x k_y B_{y\vec{k}}) + (ik_x n_{\vec{k}}) \otimes (k_x k_y B_{x\vec{k}} + k_y^2 B_{y\vec{k}})))) \\
&+ (\frac{1}{n_i^4})_{\vec{k}} \otimes (\frac{c^2 m_e}{8\pi^2 e^3}((ik_y B_{z\vec{k}}) \otimes (ik_x n_{\vec{k}}) - (ik_x B_{z\vec{k}}) \otimes (ik_y n_{\vec{k}})) \otimes \\
&\quad ((ik_y B_{z\vec{k}}) \otimes (ik_x n_{\vec{k}}) - (ik_x B_{z\vec{k}}) \otimes (ik_y n_{\vec{k}})))) \qquad (3.38)
\end{aligned}
$$

Comparing Eq. (3.38) and (3.37), it is clear that by using pseudo-spectral method, the PDE in real space is transformed to simple multiplication operations and thus $\phi_{e\vec{k}}$ is easily obtained. Like the longitudinal part, transverse electric field components are also easily obtained after transformed into Fourier domain. Note that no matter in Fourier domain or real space domain, an iterative procedure is still required for calculating transverse and longitudinal components since the electric field equations are coupled.

3.3 Finite difference method

Besides spectral methods, finite difference method could also be applied to solve PDEs, such as electric field equations (3.11)) and (3.12). The advantage of finite difference method is its considerably simpler code than that of pseudo-spectral method and its fast computation time [36]. In this section, we introduce the finite difference method and the preconditioned conjugate gradient (PCG) algorithm which is applied to solve the linear systems generated by discretizing the electric field equations using finite difference method. A comparison of using finite difference method and spectral method to solve the field equation is also addressed.

3.3.1 Finite difference approximation

Finite-difference methods approximate the solutions to differential equations by replacing derivative expressions with equivalent finite divided difference approximations known as difference quotients. To be more specific, derivatives in the partial differential equation are approximated by linear combinations of function values at the discrete grid points. Take a two-dimensional space $(X-Y)$ case as an example, where the uniform mesh grid of the $X-Y$ space is shown in Fig. 3.3. In computational application, the continuous variable $u(x,y)$ is defined on the discretized grid points, such as:

$$u_{i,j} \equiv u(x_i, y_j), x_i = i\Delta x, y_j = j\Delta y, i, j = 0, 1, 2, ..., N \tag{3.39}$$

where $\Delta x, \Delta y$ is the grid cell size. Consider a sample partial differential equation:

$$\frac{\partial u(x,y)}{\partial x} = f(x,y) \tag{3.40}$$

The heart of the finite difference method for solving differential equation is the Taylor series expansion of a function at a particular point:

$$u_{i+1,j} = u_{i,j} + \frac{\Delta x}{1!}\frac{\partial u(x,y)}{\partial x}\bigg|_{i,j} + \frac{\Delta x^2}{2!}\frac{\partial^2 u(x,y)}{\partial x^2}\bigg|_{i,j} + \frac{\Delta x^3}{3!}\frac{\partial^3 u(x,y)}{\partial x^3}\bigg|_{i,j} + ... \tag{3.41}$$

Therefore, the first order partial derivative can be expressed as:

$$\begin{aligned}
\frac{\partial u(x,y)}{\partial x}\bigg|_{i,j} &= \frac{u_{i+1,j} - u_{i,j}}{\Delta x} - \frac{\Delta x}{2!}\frac{\partial^2 u(x,y)}{\partial x^2}\bigg|_{i,j} - \frac{\Delta x^2}{3!}\frac{\partial^3 u(x,y)}{\partial x^3}\bigg|_{i,j} - ... \\
&= \frac{u_{i+1,j} - u_{i,j}}{\Delta x} + O(\Delta x) \\
&\approx \frac{u_{i+1,j} - u_{i,j}}{\Delta x}
\end{aligned} \tag{3.42}$$

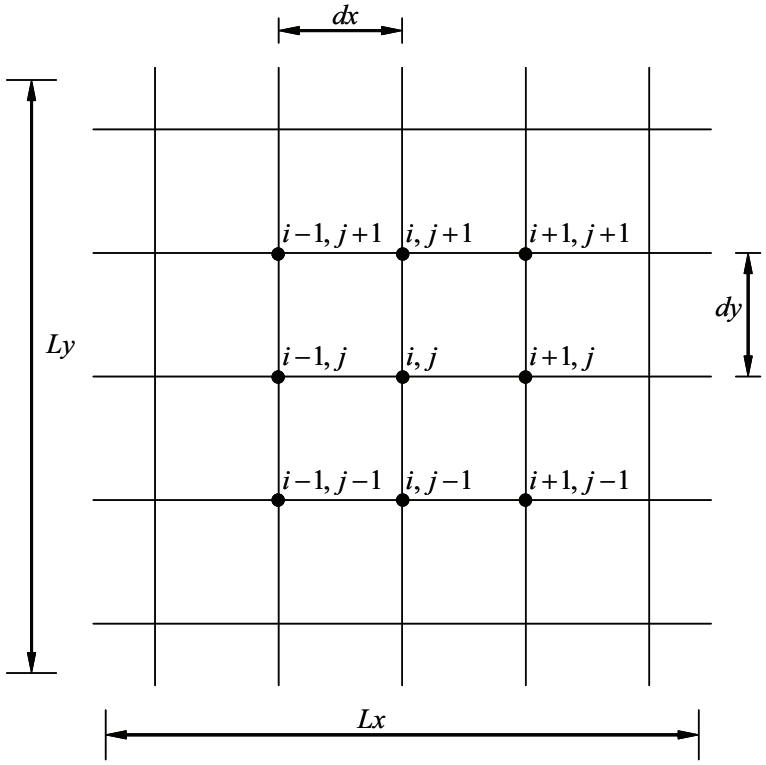

Figure 3.3: 2D uniform mesh grid setup.

where $O(\Delta x)$ is first order truncation error. This approximation is known as the forward difference. Replacing Δx by $-\Delta x$, the backward difference equation is obtained:

$$\left.\frac{\partial u(x,y)}{\partial x}\right|_{i,j} \approx \frac{u_{i,j} - u_{i-1,j}}{\Delta x} \tag{3.43}$$

To obtain more accurate approximation, we take mean of forward and backward difference:

$$\left.\frac{\partial u(x,y)}{\partial x}\right|_{i,j} \approx \frac{u_{i+1,j} - u_{i-1,j}}{2\Delta x} \tag{3.44}$$

This is central difference approximation which has a second order truncation error, and therefore more accurate. These above finite difference approximations could also be applied to $\frac{\partial u}{\partial y}$, such that the central difference approximation is:

$$\left.\frac{\partial u(x,y)}{\partial y}\right|_{i,j} \approx \frac{u_{i,j+1} - u_{i,j-1}}{2\Delta y} \tag{3.45}$$

Using Eq. (3.44), the sample partial differential equation (3.40) can be discretized to a set of linear equations:

$$\frac{u_{i+1,j} - u_{i-1,j}}{2\Delta x} = f_{i,j},\ i = 1, 2, ..., N-1,\ j = 0, 1, 2, ..., N \tag{3.46}$$

where $f_{i,j} \equiv f(x_i, y_j)$. Eq. (3.46) can be rewritten as:

$$A\mathrm{u} = \mathrm{b} \tag{3.47}$$

where A is the tri-diagonal coefficient matrix, u and b are column vectors, denoting $u_{i,j}$ and $f_{i,j}$, respectively. With proper boundary conditions, $u_{i,j}$ could be obtained easily by doing a matrix inverse operation or using Gaussian elimination method [36].

Similar to the first order partial derivative, the second order central difference approximation is:

$$\left.\frac{\partial^2 u(x,y)}{\partial x^2}\right|_{i,j} \approx \frac{u_{i+1,j} - 2u_{i,j} + u_{i-1,j}}{\Delta x^2} \tag{3.48}$$

$$\left.\frac{\partial^2 u(x,y)}{\partial y^2}\right|_{i,j} \approx \frac{u_{1,j+1} - 2u_{i,j} + u_{i,j-1}}{\Delta y^2} \tag{3.49}$$

$$\left.\frac{\partial^2 u(x,y)}{\partial x \partial y}\right|_{i,j} \approx \frac{u_{i+1,j+1} - u_{i+1,j-1} - u_{i-1,j+1} + u_{i-1,j-1}}{4\Delta x \Delta y} \tag{3.50}$$

We now apply the finite difference approximation to the electric field equation (3.11). The x component of Eq. (3.11) can be expanded as:

$$\begin{aligned}
&-(\frac{\partial^2}{\partial x^2} + \frac{\partial^2}{\partial y^2})E_{tx} + \frac{e^2}{m_e} n_i E_{tx} \\
&= -\frac{e^2}{m_e} n_i (v_{iy} B_z - v_{iz} B_y) + \frac{e}{4\pi m_e}(-\frac{\partial B_x}{\partial x} B_z - (\frac{\partial B_y}{\partial x} - \frac{\partial B_x}{\partial y}) B_y) + \frac{ce^2\eta}{4\pi m_e} n_i \frac{\partial B_z}{\partial y} \\
&+ \frac{c}{4\pi}(v_{ix}\frac{\partial^2 B_z}{\partial x \partial y} + v_{iy}\frac{\partial^2 B_z}{\partial y \partial y}) - \frac{c^2}{16\pi^2 e}\frac{1}{n_i}(\frac{\partial B_z}{\partial y}\frac{\partial^2 B_z}{\partial x \partial y} - \frac{\partial B_z}{\partial x}\frac{\partial^2 B_z}{\partial x \partial y}) \\
&+ \frac{c}{4\pi}(\frac{\partial B_z}{\partial y}\frac{\partial v_{ix}}{\partial x} - \frac{\partial B_z}{\partial x}\frac{\partial v_{ix}}{\partial y})) \\
&+ \frac{c}{4\pi}(\frac{\partial x_{ix}}{x} + \frac{\partial x_{iy}}{y})\frac{\partial B_z}{\partial y} + \frac{c^2}{16\pi^2 e n_i^2}\frac{\partial B_z}{\partial y}(\frac{\partial B_z}{\partial y}\frac{\partial n_i}{\partial x} - \frac{\partial B_z}{\partial x}\frac{\partial n_i}{\partial y}) \\
&- \frac{e^2}{m_e} n_i E_{lx}
\end{aligned} \tag{3.51}$$

Using central difference approximation, Eq. (3.51) is discretized as below:

$$-\frac{1}{\Delta x^2}E_{tx_{i-1,j}} - \frac{1}{\Delta y^2}E_{tx_{i,j-1}} + (\frac{2}{\Delta x^2} + \frac{2}{\Delta y^2} + \frac{e^2}{m_e})E_{tx_{i,j}} - \frac{1}{\Delta y^2}E_{tx_{i,j+1}} - \frac{1}{\Delta x^2}E_{tx_{i+1,j}} = b_{x_{i,j}} \tag{3.52}$$

$$A\mathrm{E_{tx}} = \mathrm{b_x} \tag{3.53}$$

where $b_{x_{i,j}}$ denotes the discretized value of the right-hand side of Eq. (3.51) on grid point $(i, j), i, j = 1, 2, ..., N-1$. Like the one-dimensional case, A is the coefficient matrix, $\mathrm{E_{tx}}$ and $\mathrm{b_x}$ are column vectors, denoting $E_{tx_{i,j}}$ and $b_{x_{i,j}}$, respectively. Note that in two-dimensional condition, A is no longer a tri-diagonal matrix, but a penta-diagonal matrix. Besides, since the computational model uses periodic boundary conditions, there are extra four diagonals. Such linear system arises regularly when numerically solving PDEs. With a finer mesh gird, it can become a sparse system that is too large to be solved by common direct or iterative methods within an acceptable computation time. In the following section, the preconditioned conjugate gradient (PCG) method which is applied to solve Eq. (3.51) for its ability to handle large sparse systems is introduced.

3.3.2 Preconditioned conjugate gradient method

The conjugate gradient method is an algorithm for the numerical solutions of particular systems of linear equations, namely those whose matrices are symmetric and positive definite. The conjugate gradient method is the most prominent iterative method for solving large sparse systems of linear equations. Besides, it is computational memory-efficient and run quickly with sparse matrices, since conjugate gradient method reference the large sparse A only through its multiplication of a vector, or the multiplication of its transpose and a vector [43]. These operations can be very efficient for a properly stored sparse matrix.

The simplest, "ordinary" conjugate gradient algorithm provide a quite general means for solving the $N \times N$ linear system

$$A\mathrm{x} = \mathrm{b} \tag{3.54}$$

where x is an unknown vector, b is a known vector, and A is a known coefficient matrix, which is square, symmetric and positive-definite. The basic idea is minimizing the quadratic function [36]:

$$f(\mathrm{x}) = \frac{1}{2}\mathrm{x}^{\mathrm{T}} A\mathrm{x} - \mathrm{b}^{\mathrm{T}}\mathrm{x} \tag{3.55}$$

This function is minimized when its gradient

$$\vec{\nabla} f = A\mathrm{x} - \mathrm{b} \tag{3.56}$$

is zero, which is equivalent to Eq. (3.54). The minimization is carried out by generating a succession of search directions $\mathrm{p_k}$ and improved minimizers $\mathrm{x_k}$. At each stage a quantity α is found that minimizes $f(\mathrm{x_k} + \alpha_k \mathrm{p_k})$ and $\mathrm{x_{k+1}}$ is set equal to the new point $\mathrm{x_k} + \alpha_k \mathrm{p_k}$. The $\mathrm{p_k}$ and $\mathrm{x_k}$ are built up in such a way that $\mathrm{x_{k+1}}$ is also the minimizer of f over the whole vector space of directions already taken, $\{\mathrm{p_1}, \mathrm{p_2}, ..., \mathrm{p_k}\}$. After N iterations, the minimizer over the entire vector space is reached, i.e., the solution to Eq. (3.54).

The reason the method is named conjugate gradient is due to the constraints to find α_k, $\mathrm{p_k}$. Let $\mathrm{r_k}$ be the residual at the kth step:

$$\mathrm{r_k} = \mathrm{b} - A\mathrm{x_k} \tag{3.57}$$

So the direction of residual $\mathrm{r_k}$ is along the line from $\mathrm{x_k}$ in the direction of the local downhill gradient $-\vec{\nabla} f(\mathrm{x_k})$. In the conjugate gradient method, the constraints is imposed on α_k that each new residual $\mathrm{r_{k+1}}$ is orthogonal to all the previous residuals $\mathrm{r_{0,1,\ldots,k}}$ and search directions $\mathrm{p_{0,1,\ldots,k}}$; and each new search direction $\mathrm{p_k}$ is constructed from the residuals to be conjugate (A-orthogonal) to all the previous residuals $\mathrm{r_{0,1,\ldots,k+1}}$ and search directions $\mathrm{p_{0,1,\ldots,k}}$ [43]. The effect of such conjugacy constraint on convergence of conjugate gradient method is illustrated and compared with that of gradient descent method in Fig. 3.4.

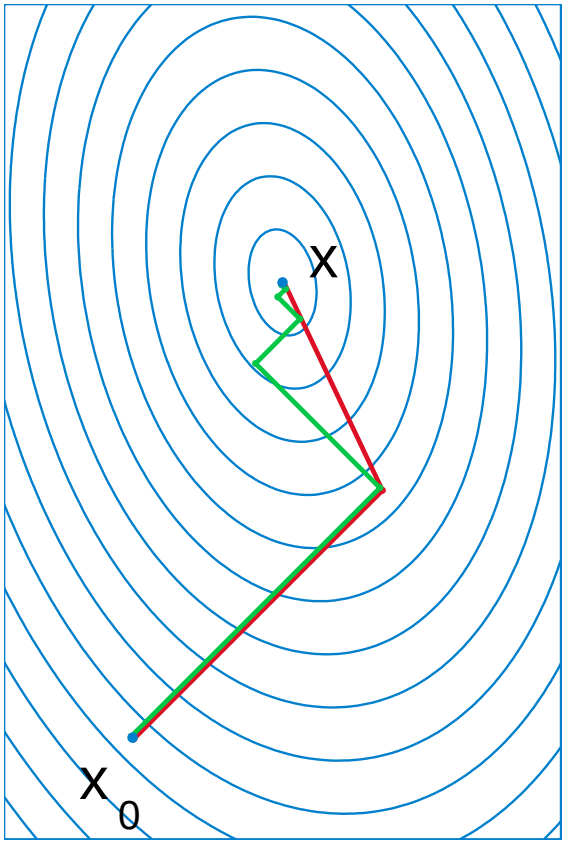

Figure 3.4: A comparison of the convergence of conjugate gradient method (in red) and gradient descent method with optimal step size (in green) for minimizing a quadratic function associated with a given linear system.

In some cases, preconditioning, as used in our work to solve electric field equations, is necessary to ensure fast convergence of the conjugate gradient method. It is a technique for reducing the condition number of a matrix. Suppose that P is a symmetric, positive-definite

matrix that approximates A, but is easier to invert. We can solve $A\mathrm{x} = \mathrm{b}$ indirectly by solving:

$$P^{-1}A\mathrm{x} = P^{-1}\mathrm{b} \tag{3.58}$$

If the condition number of $P^{-1}A$ is much smaller than that of A, or if the eigenvalues of $P^{-1}A$ are better clustered than those of A, we can iteratively solve Eq. (3.58) more quickly than the original problem. Preconditioners are especially useful when using an iterative method to solve a large, sparse linear system, since the rate of convergence for most iterative linear solvers degrades as the condition number of a matrix increases.

3.3.3 Comparison of finite difference method and spectral method

The advantage of finite difference method, as mentioned before, is its relatively simple coding implementation and its economy in computation time. However, it has to trade off the accuracy especially dealing with partial differential equations with many nonlinear terms, since the finite difference approximation may be less accurate when handling multiplication of partial derivatives or high order nonlinear terms. On the contrary, the spectral method could transform PDEs to ordinary multiplication operations and therefore much more accurate. But computation time consumed on the Fourier transforms and convolution is relatively costly.

Another advantage of finite difference method is its ability to be applied to a wide range of problems, comparing with spectral method which is preferred for regular geometries and smooth functions. Finite difference scheme could handle problems well with discontinuities while other methods are not capable of [36]. However, for a periodic system, spectral method has more advantages than any other methods, since it does not need to specify any variable values on the boundary [33].

In our work, we observed that the simulation results are more accurate when using pseudo-spectral scheme and cases using finite difference method would become less stable after being run for a considerable simulation time.

3.4 Methods of time integration

After the electric field is obtained from Eq. (3.11) and (3.12) by pseudo-spectral method or finite difference method, the electromagnetic field needs to be time advanced. In most applications of spectral methods to PDEs, the spectral methods are used for spatial discretization, but conventional finite difference methods are used in temporal discretization. We may use finite difference methods for time integration, because we do not have to deal with nonlinearities (e.g. Eq. (3.1)) that may cause inaccuracies and other problems (as in

the spatial integration). Finite difference in temporal discretization is similar to finite difference in spatial discretization described in section 3.3.1. Consider a sample time differential equation:

$$\frac{\partial u}{\partial t} = f(x, y, t) \tag{3.59}$$

Applying Taylor series expansion:

$$u(t^N + \Delta t) = u(t^N) + \frac{\Delta t}{1!}\frac{\partial u}{\partial t}\bigg|_{t^N} + \frac{\Delta t^2}{2!}\frac{\partial^2 u}{\partial t^2}\bigg|_{t^N} + \frac{\Delta t^3}{3!}\frac{\partial^3 u}{\partial t^3}\bigg|_{t^N} + ... \tag{3.60}$$

where Δt is the finite time step. The time derivative is approximated by:

$$\frac{\partial u}{\partial t}\bigg|_{t^N} \approx \frac{u(t^N + \Delta t) - u(t^N)}{\Delta t} \tag{3.61}$$

This is known as the forward time difference.

An important consideration in evaluating a numerical method is that of stability. By stability of the numerical method we mean that it imitates the behavior of the equations to the extent that the computational errors in time level N is not amplified in time level $N + 1$. By itself, the simple forward time difference method is unstable. However, it provides the starting point for deriving several good stable methods. In this section, we discuss two standard methods used to time advance the electromagnetic field.

3.4.1 Runge-Kutta method

In numerical analysis, the Runge-Kutta methods are an important family of implicit and explicit iterative methods for the approximation of solutions of differential equations. Many Runge-Kutta time discretizations have been applied in combination with spectral methods or conjugate gradient method for PDEs [6]. Runge-Kutta methods move a solution over an interval by combining the information from multiple Euler-style steps (each involving one evaluation of the right-hand side of Eq. (3.59)). Then the information obtained is used to match a Taylor series expansion. Runge-Kutta method is more stable and accurate than methods like leapfrog and Crank-Nicolson approximation [36].

The 4th-order Runge-Kutta (RK4), as used in our work, is the most commonly used in the family of Runge-Kutta methods because of its high accuracy and 5th-order truncation error. Apply this scheme to our computational model and rewrite the Faraday's law (Eq. (3.1)) in terms of electric field, we have

$$\frac{\partial \vec{B}}{\partial t} = -c(\vec{\nabla} \times \vec{E}) = -c\vec{\nabla} \times \vec{F}(\vec{B}, n_i, \vec{v}_i) \tag{3.62}$$

where Eq. (3.11) and (3.12) is rewritten as $\vec{E} = \vec{F}(\vec{B}, n_i, \vec{v}_i)$. Note that in a typical hybrid model, the particle positions $\vec{x}_p$ and the fields $\vec{E}$ and $\vec{B}$ are known at time step N (denoted by the superscript N), while the particle velocities $\vec{v}_p$ are known at the half-time step $N + 1/2$. In the RK4 scheme, the quantities on the right-hand side of Eq. (3.62) are all fixed to be evaluated at time level $N + 1/2$ except for $\vec{B}$. We can then advance this equation from time level N to time level $N + 1$ with $\vec{B}$ on the right-hand side using a 4th-order Runge-Kutta scheme as below [52]:

$$
\begin{aligned}
\vec{B}^{N+\theta} &= \vec{B}^N - c\frac{\Delta t'}{6}(\vec{K}_1^N + 2\vec{K}_2^N + 2\vec{K}_3^N + \vec{K}_4^N) \\
\vec{K}_1^N &= \vec{\nabla} \times \vec{F}(\vec{B}^N, n_i^{N+1/2}, \vec{v}_i^{N+1/2}) \\
\vec{K}_2^N &= \vec{\nabla} \times \vec{F}(\vec{B}^N + \frac{\Delta t'}{2}\vec{K}_1^N, n_i^{N+1/2}, \vec{v}_i^{N+1/2}) \\
\vec{K}_3^N &= \vec{\nabla} \times \vec{F}(\vec{B}^N + \frac{\Delta t'}{2}\vec{K}_2^N, n_i^{N+1/2}, \vec{v}_i^{N+1/2}) \\
\vec{K}_4^N &= \vec{\nabla} \times \vec{F}(\vec{B}^N + \Delta t'\vec{K}_3^N, n_i^{N+1/2}, \vec{v}_i^{N+1/2})
\end{aligned}
\tag{3.63}
$$

with a subcycled time interval, $\Delta t' = \theta \Delta t$. As shown clearly in Eq. (3.63), Runge-Kutta scheme takes multiple steps (here is 4 steps in 4th-order scheme) in going from t^N to $t^{N+\theta}$. Besides, from the perspective of variables $n_i, \vec{v}_i$, since they are fixed at time $N + 1/2$, it is a leapfrog scheme for them.

In reality, in order to minimize the computational error arising from the time advancing electromagnetic field, θ is chosen to be 0.1, i.e., going from N to $N + 1$, there are 10 subcycles in a 4th-order Runge-Kutta cycle, that is 40 steps from N to $N + 1$. However, because that our electric field solver is a fully implicit scheme and needs to be iterated no matter using spectral methods or finite difference methods, solving electric field 40 times per cycle is really time consuming. That is the trade-off for the high accuracy of 4th-order Runge-Kutta scheme.

3.4.2 Predicator-corrector method

Another commonly used time integration method is predicator-corrector method. Predicator-corrector methods try to combine the simplicity of the explicit method with the robustness of implicit methods by devising a two step explicit method. First, the prediction step calculates a rough approximation of the desired quantity, which is achieved by extrapolation from stored previous step solutions. Second, the corrector step refines the initial approximation using another means with implicit flavor. Based on different ways of extrapolating and correcting, predictor-corrector method can be divided into several kinds. The particular predicator-corrector method, as used in our work, is the Adams-Bashfort-Moulton scheme [36]. In this scheme, the Adams-Bashfort part is the predictor while the Adams-Moulton part is the corrector. Applying this scheme to solve the field equations, the basic idea is to: (i) make

a prediction of the fields (denoted by primes) at $N+1$; (ii) advance the particles in the predicted fields in order to compute the ion source terms at time level $N+3/2$; (iii) use that current and charge density to compute predicted fields at $N+3/2$; and (iv) use the average of the field at $N+1/2$ and the predicted field at $N+3/2$ to get $N+1$. In equation form, this procedure becomes the following five steps [52]:
(1) Computer the field at $N+1/2$

$$\vec{B}^{N+1/2} = \vec{B}^{N} = \frac{\Delta t}{2}\vec{\nabla} \times \vec{E}^{N}$$
$$n_i^{N+1/2} = \frac{1}{2}(n_i^{N+1} + n_i^{N})$$
$$\vec{E}^{N+1/2} = \vec{F}(\vec{B}^{N+1/2}, \vec{v}_i^{N+1/2}, n_i^{N+1/2})$$

(2) Predict the field at $N+1$ (Adams-Bashfort part)

$$\vec{E}'^{N+1} = -\vec{E}^{N} + 2\vec{E}^{N+1/2}$$
$$\vec{B}'^{N+1} = \vec{B}^{N+1/2} = \frac{\Delta t}{2}(\vec{\nabla} \times \vec{E}'^{N+1})$$

(3) Advance the ion particles to obtain the predicted source term
$\vec{v}_i{}'^{N+3/2}, \vec{x}_i{}'^{N+2}$ is determined from PIC method (PIC method in introduced in section 3.7)
(4) Computer the predicted field at $N+3/2$

$$\vec{B}'^{N+3/2} = \vec{B}'^{N+1} = \frac{\Delta t}{2}(\vec{\nabla} \times \vec{E}'^{N+1})$$
$$n_i'^{N+3/2} = \frac{1}{2}(n_i'^{N+2} + n_i^{N+1})$$
$$\vec{E}'^{N+3/2} = \vec{F}(\vec{B}'^{N+3/2}, \vec{v}_i{}'^{N+3/2}, n_i'^{N+3/2})$$

(5) Determine the corrected field at $N+1$ (Adams-Moulton part)

$$\vec{E}^{N+1} = \frac{1}{2}(\vec{E}^{N+1/2} + \vec{E}'^{N+3/2})$$
$$\vec{B}^{N+1} = \vec{E}^{N+1/2} - \frac{\Delta t}{2}(\vec{\nabla} \times \vec{E}^{N+1})$$

As observed from the above procedures, the predicator-corrector method uses the past information and therefore has a sense of robustness and is highly stable. However, since two computation cycles are required for each time step which means moving the ion particles twice, the computational speed of predicator-corrector methods is relatively slow. Besides, since it needs to store past information, the scheme is much less memory-efficient comparing with Runge-Kutta methods.

3.4.3 Comparison between Runge-Kutta method and predicator-corrector method

In our application, we examine the results obtained by 4th-order Runge-Kutta scheme and by predicator-corrector scheme. Considering the computational time, 4th-order Runge-Kutta scheme is more costly, since it need to solve electric field iteratively for 40 times . On the other hand, even if predicator-corrector scheme has to push ion particles twice, it virtually only need to solve electric field twice and take less time for one time step.

However, in terms of accuracy, the predicator-corrector scheme leads to an initial damping of electromagnetic field which is not observed when using 4th-order Runge-Kutta scheme. The results are compared in Fig. 3.5. Even if we choose η to be zero in Eq. (3.8), which means the damping mechanism is minimized, this initial field damping phenomenon is still observed for cases with low density ratio of lithium ring. The reason might be that the predicator-corrector scheme uses only two steps for time advancing per time step, while 4th-order Runge-Kutta scheme needs 40 steps.

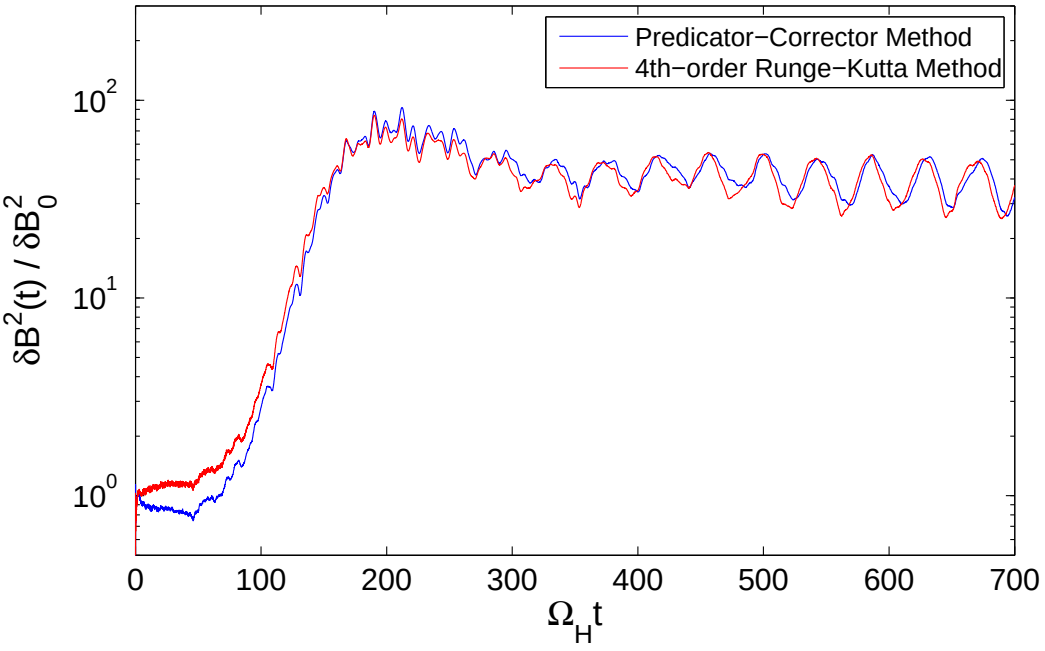

Figure 3.5: A comparison between predicator-corrector scheme and 4th-order Runge-Kutta scheme for a test case with same parameters. An initial damping of fields is observed when using predicator-corrector scheme for time integration.

3.5 Mesh configuration

Before we are in the position to shift to ion dynamics part of the computational model, it is useful to describe the mesh configuration of the hybrid model first. Hybrid model in space are usually (but not always) done on a rectangular grid. The ion particles are located anywhere within the simulation domain subdivided into 2D computational cells. This is so-called domain grid. The field quantities, on the contrary, are defined only on discrete grid points of their own unique grid mesh, such as the electric field grid and the magnetic field grid. Usually, a staggered pair of grids is used, with the electric field $\vec{E}$, plasma density $n_{i(e)}$ and flow velocity $\vec{v}_{i(e)}$ located on the vertices of one grid, and the magnetic field $\vec{B}$ on the vertices of the other grid [52]. The two grids are staggered for half a cell size if they have same resolution. Comparison of the different three mesh grids, domain, electric field, magnetic field grid, is shown in Fig. 3.6.

The reason to use staggered grid mesh is simple. In Maxwell equations (3.1) and (3.2), the electric field $\vec{E}$ and magnetic field $\vec{B}$ are in curl relation. A staggered grid could maximize the accuracy of calculating a curl relation without interpolating $\vec{E}$ and $\vec{B}$ components [49], since curl $\vec{E}$ will be given properly on the $\vec{B}$-grid, while curl $\vec{B}$ will be correct at the location of the electric field. Therefore, it has a continuous tight coupling between $\vec{E}$ and $\vec{B}$. For example, in our two dimensional space $(X - Z)$ hybrid model:

$$\frac{\partial B_x}{\partial t} = c\frac{\partial E_y}{\partial z} \Longrightarrow c\frac{E_y(i,j) - E_y(i,j-1) + E_y(i-1,j) - E_y(i-1,j-1)}{2\Delta z} \tag{3.64}$$

3.6 Boundary condition treatment

Since we are dealing with periodic boundary condition, the physical domain is virtually infinite. However, in real computational application, the domain size needs to be fixed. Therefore, to create a periodic system, we need to do boundary condition treatment whenever the simulation particles are out of bound. Specifically, when a particle is out of left or lower bound, one system domain length in the corresponding direction should be added to the particle position; when a particle is out of right or upper bound, one domain length should be subtracted from the particle position. Fig. 3.7 illustrates the periodic boundary treatment. When particles moves out of the system domain and enter into the shaded guard cells, the treatment will be applied to enforce the particles back in the domain again from the opposite boundary end.

In addition to physical grid cells, there is a "ghost cell" outside each boundary of the field mesh grids [51], i.e., surrounding the physical grid cells. Ghost cells are described by mesh points $I = 1$ and $NX2$ ($NX2 = NX + 2$), $J = 1$ and $NZ2$ ($NZ2 = NZ + 2$) in the electric field and magnetic field grid of Fig. 3.6.

As will be shown clearly in the next section, the ghost cells are important for computing the

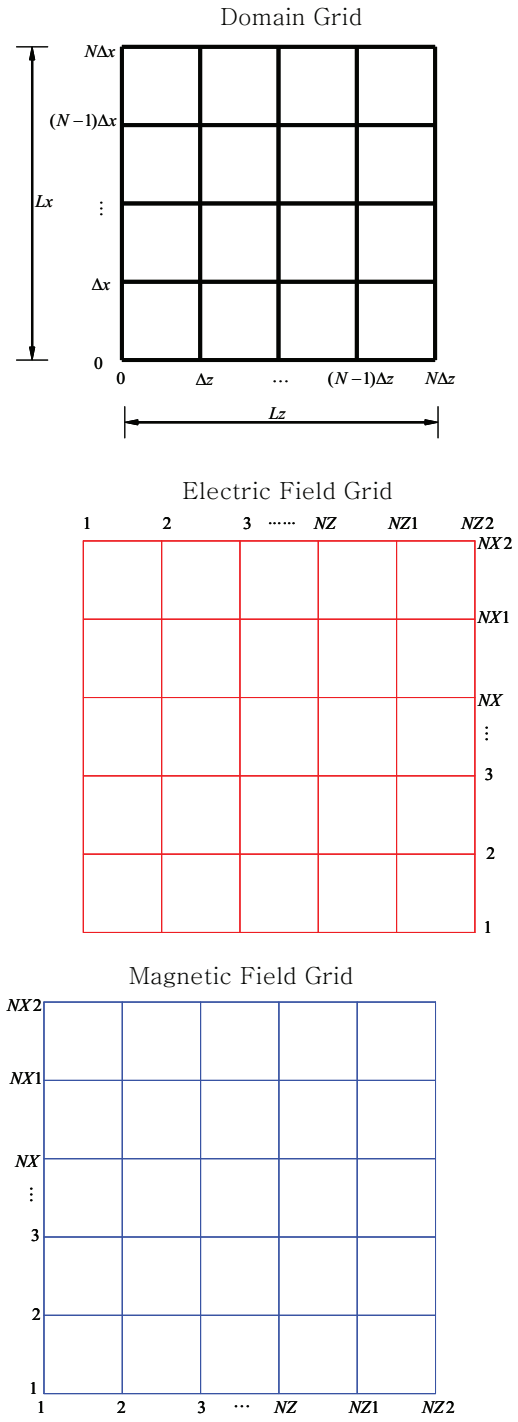

Figure 3.6: A staggered mesh grid system. The black color domain grid represents the physical space of the model. The red color electric field grid defines electric field $\vec{E}$, charge density n_i and current $\vec{J}$. The blue color magnetic field grid defines the magnetic field $\vec{B}$.

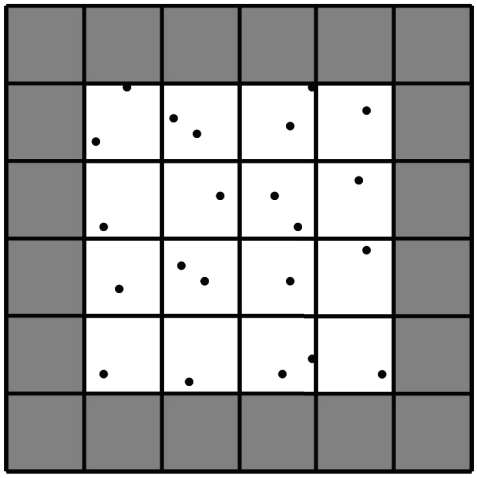

Figure 3.7: Periodic boundary treatment for a 2D spatial domain is applied when particles move into shaded guard cells.

forces acting on the kinetic particles as well as assigning the particles' contribution to the density n_i and flow velocity $\vec{v}_i$, such that the accumulation of density and flow velocity in the ghost cells should be placed back in the physical cells of the system. Take the X direction as an example. The density and flow velocity accumulated in the ghost cell 1 are put in the last physical cell $NX1$; while the density and flow velocity accumulated in the ghost cell $NX2$ are deposited in the first physical cell 2.

Besides, ghost cells are essential to imposing boundary condition on the electromagnetic fields. The periodic boundary condition indicates that the field quantities values at left ghost cell 1 equal the field quantities values at the right boundary cell $NX1$ and the field values at right ghost cell $NX2$ equal the values at the left boundary cell 2. So applies to the Z direction.

3.7 Particle-in-cell techniques

While the electrons are considered as a single fluid, the ions dynamics are treated with particle-in-cell (PIC) techniques in the hybrid model. A particle-in-cell simulation attempts to emulate plasma behavior by modeling plasma as hundreds of thousands of charged macro test particles and following the evolution of the orbits of individual test particles which are interacting with each other in an externally applied and discretized field [3]. It is the most rudimentary method to simulate a plasma, and in most cases, the test particles in the simulation model may be identified directly with the particles in the plasma. Each test particle has a set of attributes such as mass, position, charge and momentum. The evolution of the process in the plasma is determined by the laws of interactions between the particles using the discretized version of Maxwell's equations for the macroscopic field,

Newton's second law of motion, and the Lorentz' force equation. Since the particle models follow the motion of the plasma on the finest space scale and the most rapid time scale, it is limited to looking at the phenomenon in a relatively small sample of plasma and over a relatively short period of time. That's why we claimed in section 2.2.3 that processes that occur on electron scales are usually treated with fully PIC techniques.

The particles can be located anywhere within the simulation domain but the macroscopic field quantities are defined only on the discrete grid points, therefore, two interpolation steps are needed to link the particle orbits and the field components [49]. The first step is a "gather" step, which interpolate fields from grid points to particle positions. The particles velocity and trajectories are then updated using the information from the fields. The second step is called "scatter" step, as it deposits the current/charge of each particle to the field grid points and updates the discretized field quantities. Since the methods to update the fields have been introduced in the previous sections, we focus on the techniques related with other aspects of the above two steps in this section, which are interpolating fields on particle positions, moving the particles and accumulating charge density and current to grid points.

3.7.1 Interpolating fields on particle positions

The electromagnetic fields are interpolated to the particle's position to give the correct acceleration force on each particle. Typically, linear weighting is used for interpolation. This amounts to bilinear (linear in Z direction times linear in X direction) area weighting in our 2D computational model. To get a clearer view of bilinear area weighting, we superpose mesh grids of Fig. 3.6 as shown in Fig. 3.8. For example, if a particle in located at (x_p^N, z_p^N), the electromagnetic fields $\vec{E}^N(x_p^N, z_p^N), \vec{B}^N(x_p^N, z_p^N)$ on the particle position are obtained by a linear combination of contributions from the nearest four neighboring grid points [51].

$$\vec{E}^N(x_p^N, z_p^N) = W_{ie,je}\vec{E}'^N_{ie,je} + W_{ie+1,je}\vec{E}'^N_{ie+1,je} + W_{ie,je+1}\vec{E}'^N_{ie,je+1} + W_{ie+1,je+1}\vec{E}'^N_{ie+1,je+1} \quad (3.65)$$

$$\vec{B}^N(x_p^N, z_p^N) = W_{ib,jb}\vec{B}^N_{ib,jb} + W_{ib+1,jb}\vec{B}^N_{ib+1,jb} + W_{ib,jb+1}\vec{B}^N_{ib,jb+1} + W_{ib+1,jb+1}\vec{B}^N_{ib+1,jb+1} \quad (3.66)$$

where subscripts $ie = INT(x_p/\Delta x + 1.5), je = INT(z_p/\Delta z + 1.5), ib = INT(x_p/\Delta x + 2.0), jb = INT(z_p/\Delta z + 2.0)$ and INT denotes the integer truncation function. Note that here $\vec{E}'$ is an effective electric field combined of electric field $\vec{E}$ and $\eta\vec{J}$ which is the resistive drag on the ions by electrons. $\eta\vec{J}$ term could be considered as modifying the electric field felt by an ion and thus added to the electric field $\vec{E}$. The weighting factors are:

$$W_{ie(b)+1,je(b)+1} = (x_p/\Delta x + 1.5 - ie(b)) \times (z_p/\Delta z + 1.5 - je(b))$$
$$W_{ie(b),je(b)+1} = (1.0 - (x_p/\Delta x + 1.5 - ie(b))) \times (z_p/\Delta z + 1.5 - je(b))$$
$$W_{ie(b)+1,je(b)} = (x_p/\Delta x + 1.5 - ie(b)) \times (1.0 - (z_p/\Delta z + 1.5 - je(b)))$$
$$W_{ie(b),je(b)} = (1.0 - (x_p/\Delta x + 1.5 - ie(b))) \times (1.0 - (z_p/\Delta z + 1.5 - je(b)))$$

As we can see, the difference between electric field and magnetic field weighting factors is due to the fact that the two field grids are staged by half a cell.

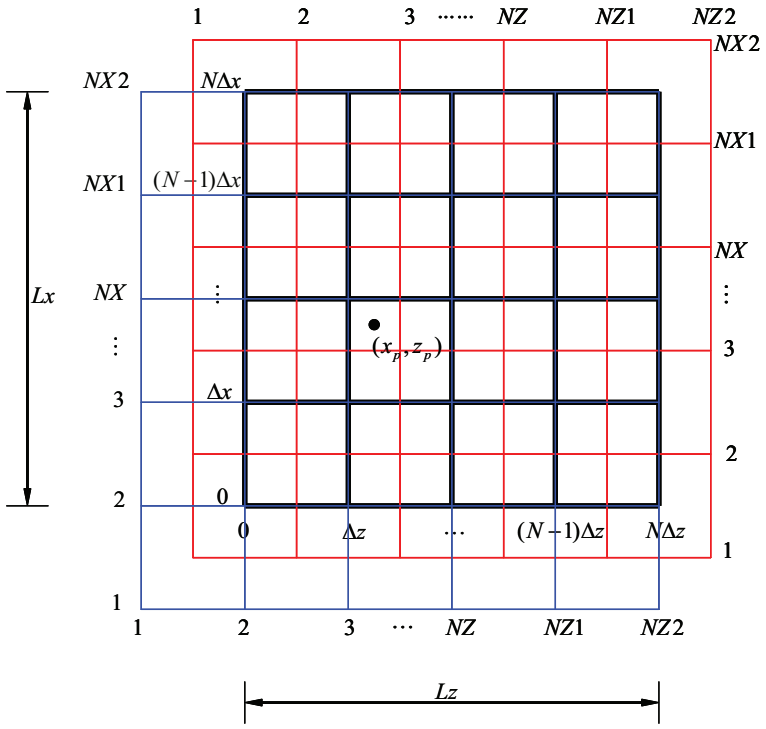

Figure 3.8: Interpolation of electromagnetic field on the particle position to obtain the force on each particle in the staggered mesh grid system.

Because the fields $\vec{E}^N(x_p^N, z_p^N), \vec{B}^N(x_p^N, z_p^N)$ are obtained from the neighboring four grid points, it is possible that several of these four points are of ghost cells. For example, if $x_p < \Delta x/2$, part of the contribution to $\vec{E}^N(x_p^N, z_p^N)$ is from $\vec{E}^N_{1,je}$ and $\eta\vec{J}^N_{1,je}$. The importance of ghost cells is now shown clearly.

3.7.2 Boris mover

After the electromagnetic field is interpolated on the particle position, the force on the particles is able to calculated and used to push the particles to update their velocities and trajectories. The method applied to update the velocity is called Boris mover which is a popular technique in particle simulation field [3]. As mentioned in section 3.4.1, in a typical hybrid model, the particle positions $\vec{x}_p$, the fields $\vec{E}$ and $\vec{B}$ are known at time step N, while the particle velocities $\vec{v}_p$ are given at the half-time step $N - 1/2$. The reason is simply to make particle positions and velocities naturally leapfrogged in time. Given $\vec{E}^N$ and $\vec{B}^N$ at the beginning of the time step, the velocities can be advanced to time level $N + 1/2$ and the

particle positions to time step $N+1$:

$$\vec{v}_p^{N+1/2} = \vec{v}_p^{N-1/2} + \frac{q_p}{m_p}(\vec{E}^N + \frac{(\vec{v}_p^{N+1/2} + \vec{v}_p^{N-1/2}) \times \vec{B}^N}{2c})\Delta t \tag{3.67}$$

$$\vec{x}_p^{N+1} = \vec{x}_p^N + \vec{v}_p^{N+1/2}\Delta t \tag{3.68}$$

Equation (3.67) is implicit in $\vec{v}_p^{N+1/2}$, as $\vec{v}_p^N$ is rewritten as $1/2(\vec{v}_p^{N+1/2} + \vec{v}_p^{N-1/2})$. Examining the above equations, we notice that the force on each particle could be divided to two parts: electric force $\vec{F}_{electric} = q_p\vec{E}$ and magnetic force $\vec{F}_{magnetic} = q_p\frac{\vec{v}_p \times \vec{B}}{c}$. The first part only change the magnitude of $\vec{v}_p$, and the second part is a $\vec{v}_p \times \vec{B}$ rotation without changing the magnitude of $\vec{v}_p$, as shown in Fig. 3.9(a).

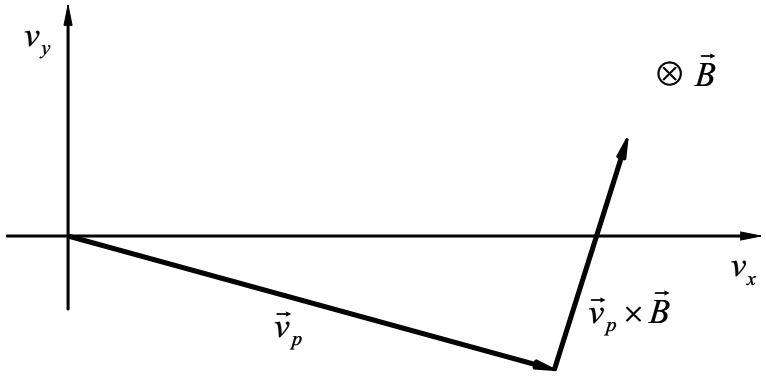

(a) The $v_x - v_y$ plane, showing the $q_p\frac{\vec{v}_p \times \vec{B}}{c}$ force normal to $\vec{v}_p$, which results in a rotation of $\vec{v}_p$, with no change in speed (here $q_p > 0$)

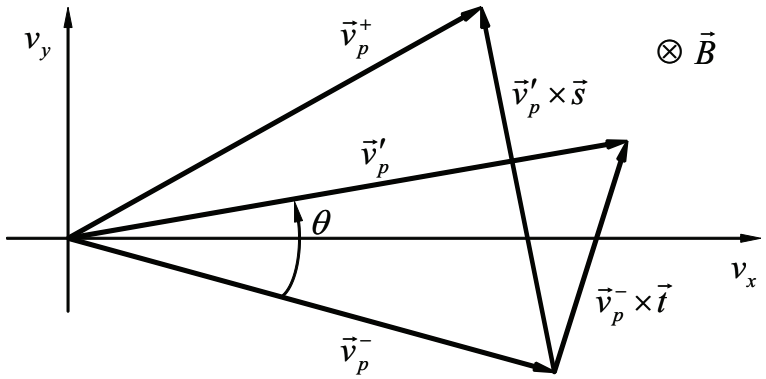

(b) Velocity space showing the rotation from $\vec{v}_p^-$ to $\vec{v}_p^+$. The velocities shown are projections of the total velocities onto the plane perpendicular to $\vec{B}$

Figure 3.9: A schematic of Boris mover scheme

Therefore, we could separate the velocity update into three steps, using this standard time-centering leapfrog scheme. Equation (3.67) is written as the following three steps [3]:

$$\text{step 1: } \vec{v}_p^{\,-} = \vec{v}_p^{N-1/2} + \frac{q_p \vec{E}^N \Delta t}{2m_p} \text{ (first half } \vec{E} \text{ acceleration)} \tag{3.69}$$

$$\text{step 2: } \frac{\vec{v}_p^{\,+} - \vec{v}_p^{\,-}}{\Delta t} = \frac{q_p}{m_p c} \frac{\vec{v}_p^{\,+} + \vec{v}_p^{\,-}}{2} \times \vec{B}^N = \frac{\vec{v}_p^{\,+} + \vec{v}_p^{\,-}}{2} \times \mathbf{\Omega}_p^N \text{ } (\vec{v}_p \times \vec{B} \text{ rotation}) \tag{3.70}$$

$$\text{step 3: } \vec{v}_p^{N+1/2} = \vec{v}_p^{\,+} + \frac{q_p \vec{E}^N \Delta t}{2m_p} \text{ (second half } \vec{E} \text{ acceleration)} \tag{3.71}$$

Solving Eq. (3.70) is tricky and potentially numerically intense especially if simulating millions (billions) of particles. It is best cast in the form of a rotation of the velocity vector. Eq. (3.70) is then divided into two substeps which are shown in Fig. 3.9(b):

$$\text{step 2a: } \vec{v}_p^{\,\prime} = \vec{v}_p^{\,-} + \vec{v}^{\,-} \times \vec{t} \text{ (first half } \vec{B} \text{ rotation)} \tag{3.72}$$

$$\text{step 2b: } \vec{v}_p^{\,+} = \vec{v}_p^{\,-} + \vec{v}_p^{\,\prime} \times \vec{s} \text{ (Second half } \vec{B} \text{ rotation)} \tag{3.73}$$

where $\vec{t} = -\hat{\mathbf{B}}_0 \tan\frac{\theta}{2}, \tan\frac{\theta}{2} \approx \frac{\theta}{2} = \frac{\Omega_p^N \Delta t}{2}$ for small Δt, $\vec{s} = -\hat{\mathbf{B}}_0 \sin\theta$ and $s = \frac{2t}{1+t^2}$. The above procedures is called Boris mover.

After obtaining $\vec{v}_p^{N+1/2}$, we could proceed to update the trajectory of each particle, using the leapfrog scheme Eq. (3.68) with periodic boundary treatment described in section 3.6

3.7.3 Accumulation of charge density and flow velocity

After the particles are moved to new positions, the charge density and current can be deposited back to the grid. Since the ion current are essential the ion flow velocity $\vec{v}_i$, we will only consider the accumulation of ion number density n_i and flow velocity $\vec{v}_i$ which are related with particle positions x_p^{N+1}, y_p^{N+1}, and particle velocities $\vec{v}_p^{N+1/2}$, respectively. In this sense, the density is collected at time level $N+1$ and flow velocity at $N+1/2$ [52].

To determine n_i^{N+1} and $\vec{v}_i^{N+1/2}$, we weight the particle number and velocity to the nearest four neighboring grid points in a similar way we did in interpolating fields on the particle positions. Note that since our mesh system defines the plasma density and flow velocity at the same position of electric field, this mesh grid for accumulation process is the electric field grid. The only difference between the "scatter" step and "gather step" in section 3.7.1 is that fields on the particle position are only determined by the neighboring four grid points; however, the contribution to the density and flow velocity on a grid point could come from thousands of particles, which deposit their own charges and velocities to the neighboring four grid points.

3.8 Initialization

Before completing the discussion of our hybrid model, we turn to how to get started: initialization. General speaking, there are three steps in initialization: setting up the domain size and time step, loading the particles in physical space, loading the particles in phase space, which are described in the following.

3.8.1 Spatial size and time step

The system's spatial size is based on physical considerations, such as, large enough to contain several anticipated wavelength of the instabilities and to allow plenty of room for possible wave-wave interactions. Since the domain is subdivided into computational cells, the cell size is then chosen to resolve the characteristic phenomena, i.e. enough cells (at least 5 cells) to well resolve the dominant modes [51]. In our particular problems, the highly oblique short wavelength Alfven waves ($k_\perp \gg k_z$) become ordinary longer wavelength Alfven waves ($k_\perp \sim k_z$) in the nonlinear evolution. Therefore, unless choosing a huge domain with very refined mesh grids, it is hard to maintain enough dominant modes in the simulation domain while able to well resolve them during the entire simulation. Such fact restricts further development of the waves in our simulation which would be shown in chapter 4.

Hybrid model usually choose constant time step, although adaptive time step has also been employed. Like the principle of choosing spatial cell size, the time step should be small enough to resolve the characteristic phenomena. Usually, the time step is limited to the condition that ion cyclotron frequency Ω_i is well resolved as well as keeping the particle increments not transverse more than one cell per time step. Typically, for 1D, the particle spatial increment, which is set to some fraction of one computational cell, is $V_{max}\Delta t \leq \Delta x/2$, where V_{max} represents the maximum speed of the particles. That is called Courant-Friedrichs-Lewy condition.

3.8.2 Loading the particles in space

The particles are loaded uniformly in space since the initial densities of hydrogen and lithium are uniform. The number of particles per cell should be large enough to give good statistics, yet not too many to make the run time excessive. To minimize the simulation noise level, 400 background hydrogen particles per cell as well as 400 lithium particles are loaded. Because of the quasi-neutral condition Eq. (3.3), the electron fluid density n_e equals the ion flow density n_i and they are defined at same grid points. Therefore, the initial conditions satisfy the Poisson's equation $\vec{\nabla} \cdot \vec{E} = 4\pi e(n_i - n_e)$. Besides, since the initial $\vec{B}$ is a constant which equals $\vec{B}_0$, $\vec{\nabla} \cdot \vec{B} = 0$ is also satisfied naturally.

3.8.3 Loading a Maxwellian velocity distribution

The particles which represent background hydrogen are loaded with a Maxwellian distribution in the velocity space. By defining a loading function $R_j(\vec{v})$ in terms of the velocity distribution $F_j(\vec{v})$ [51] (taking perpendicular velocity $\vec{v}_\perp$ as an example),

$$R_j(\vec{v}_\perp) = \frac{\int_0^{\vec{v}_\perp} F_j(\vec{v}_\perp)\vec{v}_\perp d\vec{v}_\perp}{\int_0^{\infty} F_j(\vec{v}_\perp)\vec{v}_\perp d\vec{v}_\perp} = 1 - \exp(-\vec{v}_\perp^2/\vec{v}_t^2) \tag{3.74}$$

we could easily invert Eq. (3.74) to obtain $\vec{v}_\perp$. Here choosing R_j to be a uniform random number set between 0 and 1. $\vec{v}_t$ is the thermal velocity. The random $\vec{v}_\perp$ is then used to calculate the v_x, v_y, using the Eq. (3.76) below:

$$\begin{aligned} v_x &= v_\perp \cos\phi \\ v_y &= v_\perp \sin\phi \end{aligned} \tag{3.75}$$

where ϕ is a random angle $0 \leq \phi \leq 0$. The similar fashion could be applied to get v_z, the parallel velocity. Besides, to decorrelate positions and velocities between particles, a random pair exchange between two particles is performed minimizing the influence due to imperfect random number generator. This above method is also able to include a nonrandom drift or other forms of distribution functions.

However, using the uniform random number set R_j to phase space tends to produce simulation with fully developed fluctuation level which is larger than laboratory levels; the level of noise may also prevent observing low level physics. In addition, the desired density variation may be reproduced on a gross scale, the moments of the density, however, may be poor on a fine scale. Hence, it is desirable to improve on the use of uniform random set. One way to achieve this is so-called "quiet start" which numerically integrates the distribution function in small steps and set equal to different R_j . The details of "quiet start" method could be found in Ref. [3].

3.8.4 Loading a ring velocity distribution

To drive the instability, the released lithium species has a ring distribution of velocity perpendicular to the background magnetic field $\vec{B}_0$. A simple way to create such distribution is as follows [25]:

$$v_r = v_\perp = \sqrt[2]{v_x^2 + v_y^2} = \sqrt[2]{v_{max}^2 + (1-\xi)v_{min}^2} \tag{3.76}$$

where v_{max} are v_{min} the estimated maximum and minimum ring speed respectively; ξ is a random number between 0 and 1. In our application, v_{max} and v_{min} are same since initially

the lithium ions are assumed to be cold with $v_r = 7km/s$. After $v_\perp$ is calculated, v_x and v_y could be obtained using Eq. (3.76) again. Similar to the idea of "quiet start" method described in section 3.8.3, four ring velocity particles are loaded simultaneously each time with random angle $\phi_1 = \phi, \phi_2 = \pi - \phi, \phi_3 = -\phi$ and $\phi_4 = \pi + \phi$. Therefore, the velocity vectors are canceled out and the initial fluctuation level is minimized. Again, after loading all the particles, random pair exchange is performed in order to decorrelate positions and velocities.

3.9 Normalization

Finally, the hybrid model needs to be normalized for minimizing the round-off error [51]. Usually, the speed of light c is the unit of velocity and inverse ion plasma frequency ω_i is the unit of time. The full normalization units are:

$e = e_0 e_s$, where e_0 is the proton charge
$m = m_0 m_s$, where m_0 is the proton mass
$n = n_0 n_s$, where n_0 is the initial ion number density equal to $n_H + n_{Li}$
$v = c v_s$, where c is the speed of light
$x = \dfrac{c}{\omega_i} x_s$, where $\omega_i^2 = \dfrac{4\pi n_0 e_0^2}{m_0}$
$t = \omega_i^{-1} t_s$
$E = \dfrac{m_0 c \omega_i}{e_0} E_s, B = \dfrac{m_0 c \omega_i}{e_0} B_s$
$\eta = \dfrac{4\pi}{\omega_i} \eta_s$

Here Ψ is field or particle variable, Ψ_0 is unit of the variable and Ψ_s is the normalized value of the variable.

Model equations then become dimensionless after normalized by these units, such as:

$$\vec{\nabla}_s \times \vec{E}_s = -\frac{\partial \vec{B}_s}{\partial t_s} \tag{3.77}$$

$$\vec{\nabla}_s \times \vec{B}_s = \vec{J}_s = n_{i_s}(\vec{v}_{i_s} - \vec{v}_{e_s}) \tag{3.78}$$

$$\frac{d\vec{v}_{p_s}}{dt} = \vec{E}_s + \vec{v}_{p_s} \times \vec{B}_s - \eta_s \vec{J}_s \tag{3.79}$$

$$\frac{d\vec{x}_{p_s}}{dt_s} = \vec{v}_{p_s} \tag{3.80}$$

$$
\begin{aligned}
&- \nabla_s^2 \vec{E}_{t_s} + \frac{n_{i_s}}{m_{e_s}} \vec{E}_{t_s} \\
&= -\frac{n_{i_s}}{m_{e_s}} (\vec{v}_{i_s} \times \vec{B}_s) + \frac{1}{m_{e_s}} (\vec{\nabla}_s \times \vec{B}_s) \times \vec{B}_s + \frac{n_{i_s} \eta_s}{m_{e_s}} (\vec{\nabla}_s \times \vec{B}_s) \\
&+ (\vec{v}_{i_s} \cdot \vec{\nabla}_s)(\vec{\nabla}_s \times \vec{B}_s) - \frac{1}{n_{i_s}} ((\vec{\nabla}_s \times \vec{B}_s) \cdot \vec{\nabla}_s)(\vec{\nabla}_s \times \vec{B}_s) \\
&+ ((\vec{\nabla}_s \times \vec{B}_s) \cdot \vec{\nabla}_s) \vec{v}_{i_s} \\
&+ (\vec{\nabla}_s \cdot \vec{v}_{i_s})(\vec{\nabla}_s \times \vec{B}_s) + \frac{1}{n_{i_s}^2} (\vec{\nabla}_s \times \vec{B}_s)((\vec{\nabla}_s \times \vec{B}_s) \cdot \vec{\nabla}_s) n_{i_s} \\
&- \frac{n_{i_s}}{m_{e_s}} \vec{E}_{l_s}
\end{aligned} \tag{3.81}
$$

$$
\begin{aligned}
&\nabla_s^2 \phi_{e_s} + \frac{1}{n_{i_s}} (\vec{\nabla}_s n_{i_s} \cdot \vec{\nabla}_s \phi_{e_s}) \\
&= (\vec{B}_s \cdot (\vec{\nabla}_s \times \vec{v}_{i_s}) - \vec{v}_{i_s} \cdot (\vec{\nabla}_s \times \vec{B}_s)) \\
&+ \frac{1}{n_{i_s}} ((\vec{v}_{i_s} \times \vec{B}_s) \cdot \vec{\nabla}_s n_{i_s} + \vec{B}_s \cdot \nabla_s^2 \vec{B}_s + (\vec{\nabla}_s \times \vec{B}_s) \cdot (\vec{\nabla}_s \times \vec{B}_s) - \eta_s (\vec{\nabla}_s \times \vec{B}_s) \cdot \vec{\nabla}_s n_{i_s} + \vec{\nabla}_s n_{i_s} \cdot \vec{E}_{t_s} \\
&\quad - m_e ((\vec{\nabla}_s \times \vec{B}_s) \cdot (\vec{\nabla}_s (\vec{\nabla}_s \cdot \vec{v}_{i_s})) + \vec{\nabla}_s \cdot ((\vec{v}_{i_s} \cdot \vec{\nabla}_s)(\vec{\nabla}_s \times \vec{B}_s) + (\vec{\nabla}_s \times \vec{B}_s \cdot \vec{\nabla}_s) \vec{v}_{i_s}))) \\
&+ \frac{m_e}{n_{i_s}^2} \vec{\nabla}_s \cdot ((\vec{\nabla}_s \times \vec{B}_s \cdot \vec{\nabla}_s)(\vec{\nabla}_s \times \vec{B}_s)) \\
&- \frac{m_e}{n_{i_s}^3} (\vec{\nabla}_s \times \vec{B}_s) \cdot ((\vec{\nabla}_s \times \vec{B}_s \cdot \vec{\nabla}_s)(\vec{\nabla}_s n_{i_s}) + (\vec{\nabla}_s n_{i_s} \cdot \vec{\nabla}_s)(\vec{\nabla}_s \times \vec{B}_s) - \vec{\nabla} n_{i_s} \times \nabla_s^2 \vec{B}_s) \\
&- \frac{m_e}{n_{i_s}^3} \vec{\nabla}_s n_{i_s} \cdot ((\vec{\nabla}_s \times \vec{B}_s \cdot \vec{\nabla}_s)(\vec{\nabla}_s \times \vec{B}_s)) \\
&+ \frac{2 m_e}{n_{i_s}^4} ((\vec{\nabla}_s \times \vec{B}_s) \cdot \vec{\nabla}_s n_{i_s})^2
\end{aligned} \tag{3.82}
$$

3.10 Computational cycle

We summarize the model algorithms in a computational cycle as a flowchart shown in Fig. 3.10.

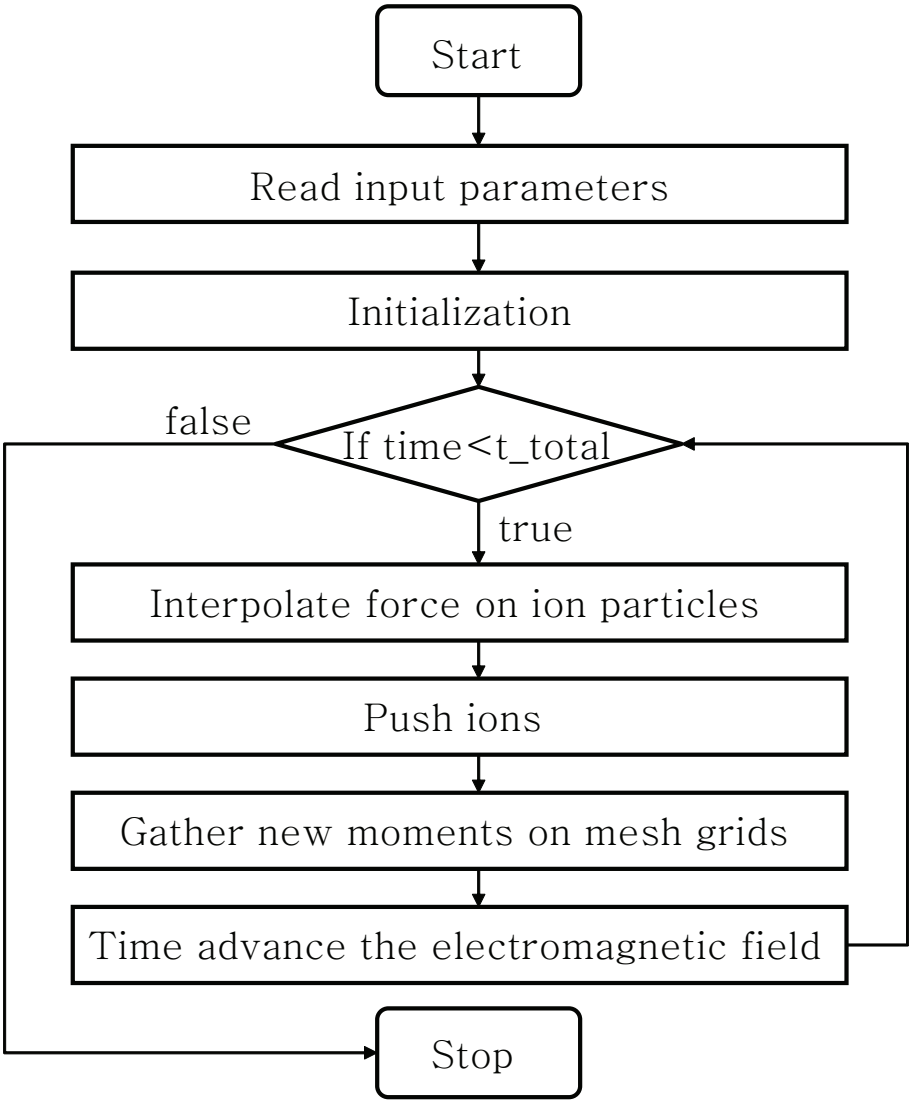

Figure 3.10: Flowchart of the electromagnetic hybrid model

Chapter 4

Simulation results

In this chapter, we discuss in detail the simulation results of the generation of the ring velocity instability and the nonlinear evolution of the ion-cyclotron turbulence. A benchmark case with description of the basic ring instability and nonlinear evolution is presented first. Important effects of varying the ring plasma density are considered later. The effect of further nonlinear processes on the ring energy extraction is also addressed along with the discussion of the viability of the shear Alfven waves under consideration for radiation belt remediation.

4.1 Initial conditions

In modeling the evolution of the ring velocity instability, the choice of initial conditions is very important. In order for the instability to develop clearly, the benchmark case described here uses a rather large lithium ring plasma to background plasma density ratio $n_{Li}/n_H = 0.1$. Other parameters are chosen to be consistent with the linear theory. The velocity of the ring is the same as section 2.2.2 with $v_r/v_{tH} \approx 1/\sqrt{2}$ which corresponds to a release speed of approximately 7km at the altitude $6000km$. The lithium ring is taken to be cold with $T_{Li} \approx 0$. The background plasmas have maxwellian distributions. The interaction between two velocity distributions will drive the instability. The 2D $(X-Z)$ simulation box, which is shown in Fig 3.1, is 128×128 grid cells with the background magnetic field in the simulation plane and in the Z direction. The domain is elongated along the background magnetic field with length along the magnetic field $L_z \approx 60c/\omega_{pH}$. The length across the magnetic field $L_x \approx 1.2c/\omega_{pH}$. Such a simulation domain is required to follow the evolution of waves with long wavelengths along the magnetic field and relatively short wavelengths across the magnetic field as described in the previous section. For the parameters of interest, the simulation domain corresponds to $L_z \approx 250$km and $L_x \approx 5$km. Besides, to minimize the noise level, 400 background hydrogen simulation particles per cell as well as 400 lithium

particles per cell are loaded in the simulation, which totally equals 13 million particles. The end time of the benchmark case is $\Omega_H t = 600$ which provides enough time to observe the nonlinear evolution. The parameters used for the benchmark simulation is summarized in table 4.1.

Table 4.1: Parameters correspond to benchmark simulation case.

Parameter	Unit	Quantity
Ambient magnetic field (B_0)	G	0.04
Ambient electric field (E_0)	G	0
Alfven velocity (V_A)	km/s	1.6×10^3
Ring velocity (v_r)	km/s	7
Initial ambient plasma temperature ($T_{H(e)}$)	eV	0.53(0.53)
Initial ring plasma temperature (T_{Li})	eV	0
Density ($n_{H(Li)}$)	cm^{-3}	3000(300)
Domain size ($L_{z(x)}$)	km	250(5)
Grid cells ($N_{z(x)}$)	1	128(128)
Time step (Δt)	$1/\Omega_H$	0.01

Initially, the particles are loaded uniformly in the simulation box therefore the ion density is same on the whole grid points. Figure 4.1 shows the initial 2D fluctuating magnetic field and density structures at $\Omega_H t = 1$. Note that at the beginning of the simulation, there only exists background magnetic field along Z direction with no fluctuating electromagnetic field. To let the simulation reach its steady noise level, we consider quantities at $\Omega_H t = 1$ as the initial values.

4.2 Temporal evolution

The simulation results in real time and space domain are presented first. The quality of our numerical simulations is checked by considering the time history of the energy conservation shown in Fig. 4.2. The total energy includes the fluctuating electromagnetic field energy and the particles' kinetic energy. The energy conservation shows to be fairly good as variation is around 0.5%. Since energy stored in finite mass electron fluid is not included in the total energy, such a small variation of energy conservation is acceptable in hybrid models and thus good numerical results are indicated. We would like to investigate the impacts of the spectral filter on energy conservation by using different filter parameters $\alpha = \vec{k}/k_{last}$. As stated clearly in section 3.2.4, k_{last} is the mode number that the amplitude of this mode is attenuated to $\frac{1}{e}$ of its original value. Figure 4.3 shows the total energy time history of 30% ring density ratio cases with different spectral filter parameter k_{last}. With no filter, the

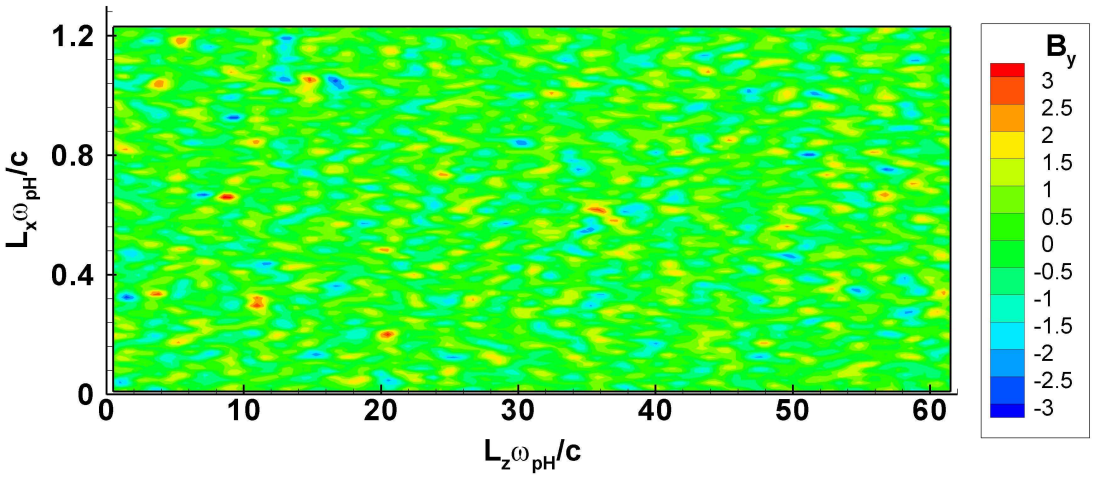

(a) The magnetic field B_y (the biggest fluctuating component) at time $\Omega_H t = 1$.

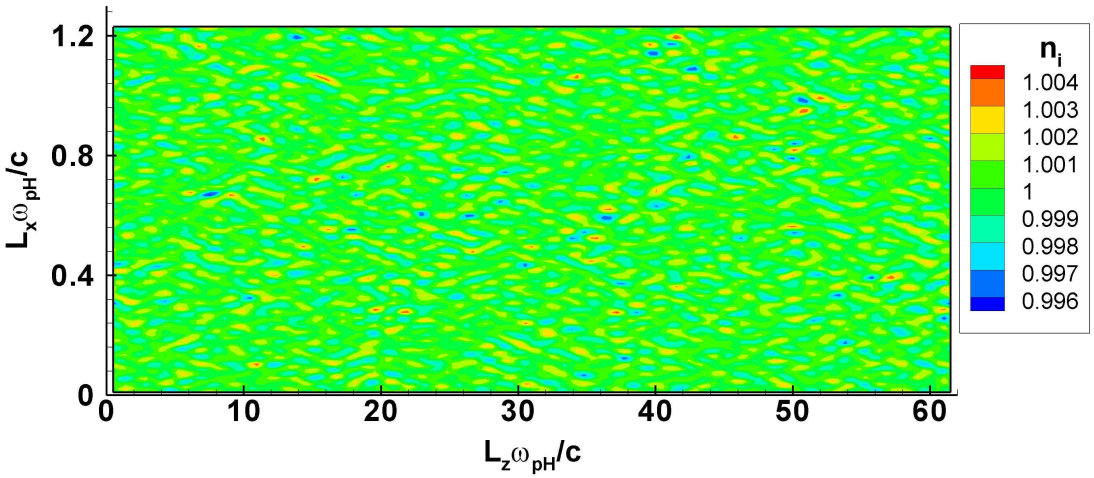

(b) The density n_i structures at time $\Omega_H t = 1$.

Figure 4.1: Initial fluctuating magnetic field and density used for normalization.

simulation becomes unstable due to numerical noises when the instability begins to develop. After a filter is applied, the high mode noise is attenuated and the simulation becomes stable. As the k_{last} continues to decrease, the the energy conservation is getting better and becomes almost constant. Note that when a low k_{last} is chosen such as $k_{last} = 26$, the energy conservation does not experience an obvious change. This indicates that it is the high mode noise that drives the numerical instability and causes the total energy variation. In the following simulation cases, k_{last} is chosen to be 32, which corresponds to filter structures within 4 grid cells.

Next, we check the thermal fluctuation induced by numerical errors. If the numerical errors

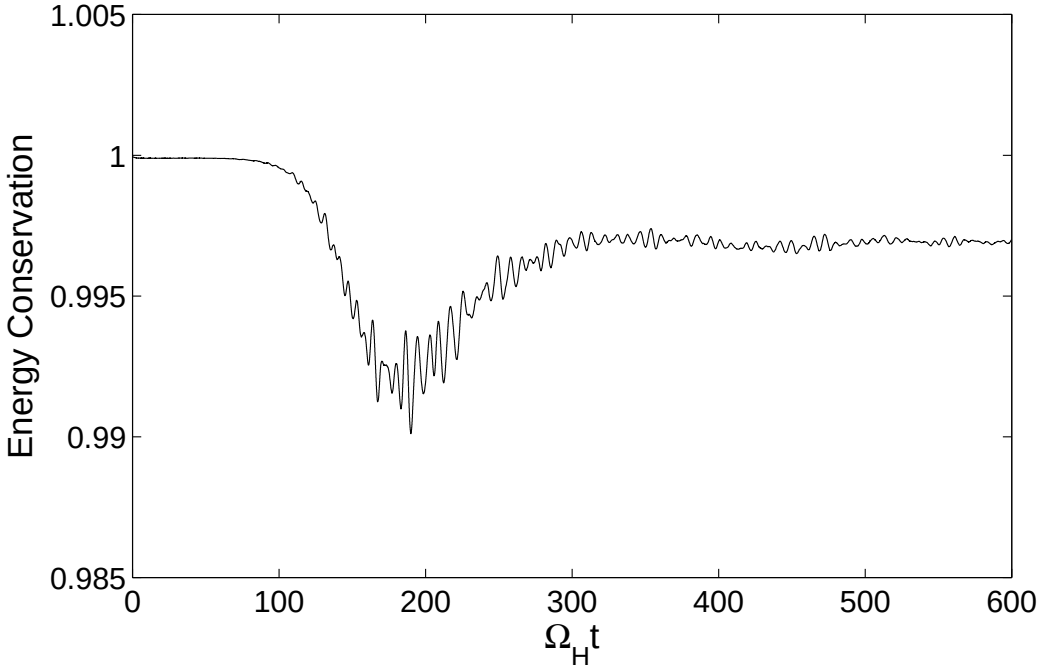

Figure 4.2: Time history of total energy show a 0.5% variation, indicating a good quality of the benchmark simulation case.

are in the acceptable range, the thermal fluctuation should be small enough that no obvious periodic oscillation is observed in the field energy history plot, for example. Figure 4.4 is the time history of the magnetic field energy for the case that no lithium plasma is included in the simulation. As shown clearly, the field energy experience no growth compared with the case having lithium plasma, such as Fig. 4.6(a). The frequency power spectrum is shown in Fig. 4.5. It is taken over the entire time of the simulation and most of wave power is focused at the hydrogen cyclotron frequency Ω_H and no significant modes at the Alfven frequency are observed. Comparing the magnitude of the power spectrum with the benchmark case Fig. 4.10, we notice that the wave power is two magnitude smaller than that of the benchmark case with 10% ring plasma density ratio. This indicates that the normal plasma modes are seldom enhanced by the noise in the PIC method. We also checked the 2D magnetic field contour plots at various time of simulation and observed no dominant periodic fluctuations. Therefore, the numerical fluctuation is small enough and the dominant structures and modes observed in the following benchmark case should be trusted and not considered as numerical structures.

Figure 4.6 shows the time evolution of the field energy, which separates into the magnetic field energy, the electrostatic component of electric field energy and the electromagnetic component of electric field energy. The instability begins to develop after the lithium ring interacts with the background plasma for a short while. During the initial evolution, linear

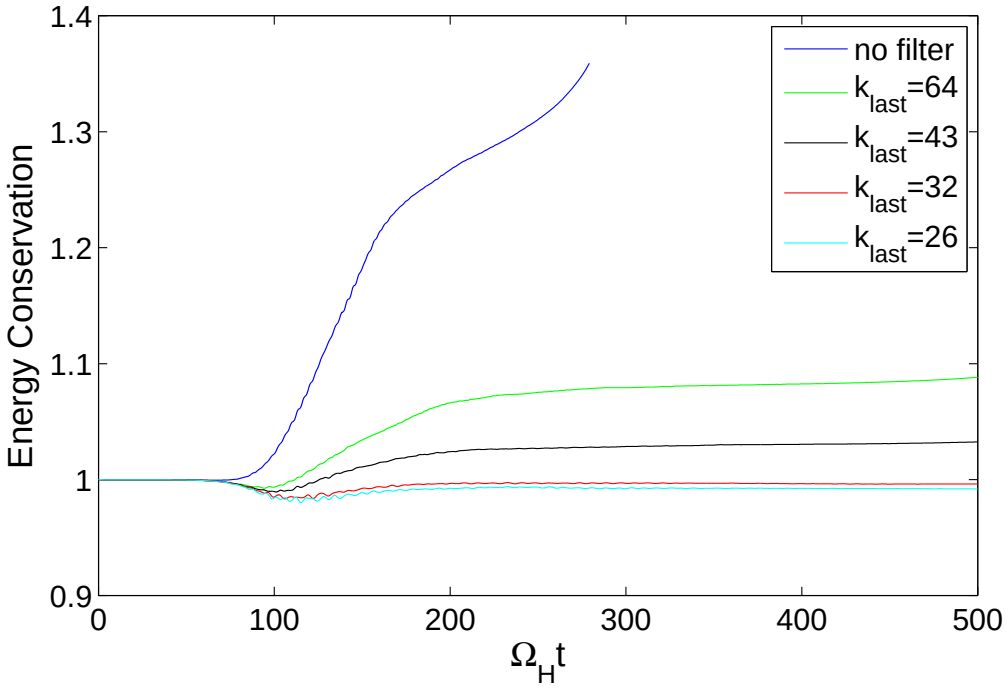

Figure 4.3: Total energy time history of 30% ring density ratio cases with different spectral filter parameter k_{last}.

growth in the field is observed in both the magnetic and electrostatic electric components. The linear growth rate from Fig. 2.7 is observed to describe the growth of the fields well as we calculated the growth rate from Fig. 4.6. The growth rate can be obtained by the following procedures:

1. Take nature logarithm of the field energy. Since in linear theory, the amplitude of fluctuating field could be described as $E_1 e^{\gamma t}$ (see section 2.2.2), the field energy is then expressed as $0.5E_1^2 e^{2\gamma t}$ and the nature logarithm gives $2\gamma t + \ln(0.5E_1^2)$.

2. Take the linear fit of the nature logarithm of the field energy v.s. time. The growth rate is then obtained by dividing the slope by 2.

For the 10% ring density benchmark case, the growth rate normalized to the hydrogen cyclotron frequency γ/Ω_H is about 0.018, which is consistent with linear theory shown on Fig. 2.7. We also would like to investigate the impacts of the spectral filter on linear growth rate. Figure 4.7 shows the magnetic field energy time history of 30% ring density ratio cases with different k_{last} corresponding to Fig. 4.3. As shown clearly, the filter has no impacts on linear growth rate. Although the case with no filter becomes unstable after the linear growth period, the growth rate is same as those cases with spectral filter. The

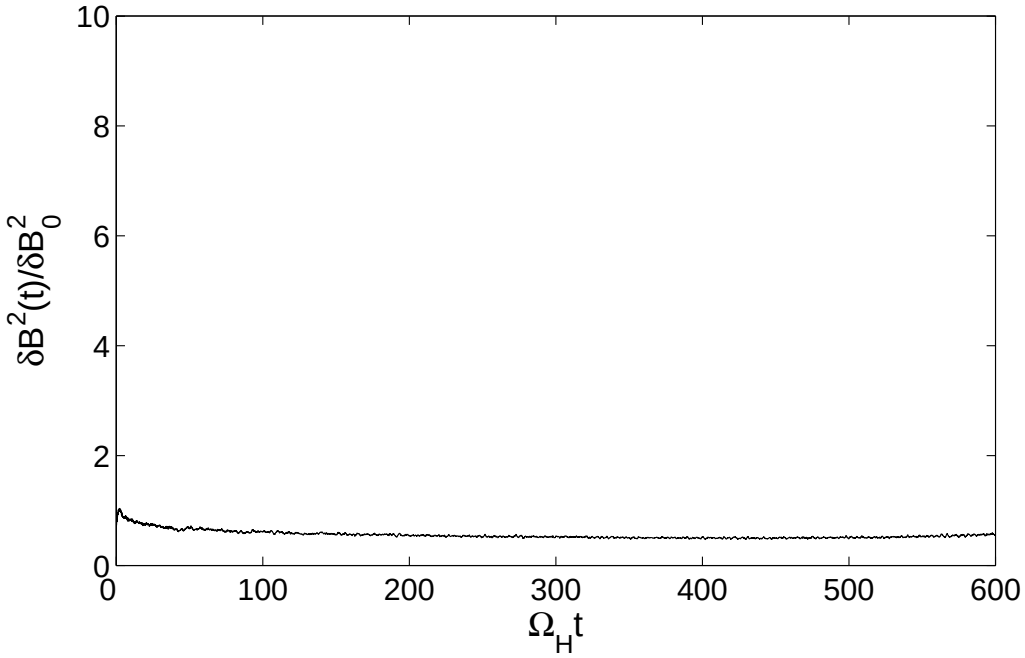

Figure 4.4: Time history of magnetic field energy for the case with no lithium plasma included.

filter tends to attenuate the field energy magnitude a little bit, however, the overall trend remains unchanged and the simulation results are still useful to investigate the further wave evolution.

In Fig. 4.6, note that although both electrostatic and electromagnetic components of electric field increase by a similar factor, the absolute magnitude of electrostatic component is much bigger than that of electromagnetic component. Therefore, the electric field energy are mostly electrostatic. At time $\Omega_H t = 150$ the linear wave growth saturates as the slopes of the field energy growth begin to decrease. The higher frequency oscillations during the linear growth period, observed in both magnetic field energy and electric field energy, are interpreted as lithium cyclotron harmonic frequencies which are pointed out in Fig. 4.6(a). This corresponds with the linear theory calculation shown in Fig. 2.7. The detailed frequency analysis will be presented shortly. Figure 4.8 shows the fluctuating magnetic field and the density structures at $\Omega_H t = 150$. As we could observe from the magnetic field, the wave front shows much longer wavelength in parallel direction and shorter wavelength in perpendicular direction. This signature corresponds with the wavenumber which is $k_x \gg k_z$ initially. The wavenumber analysis is shown later in this section. Besides, the waves have already tended to form larger structure in Fig. 4.8(a). The density structures show oscillations primarily along the Z direction, which means transverse to the propagation direction of the wave. (A movie of density structure shows a much clearer oscillation along the background magnetic field).

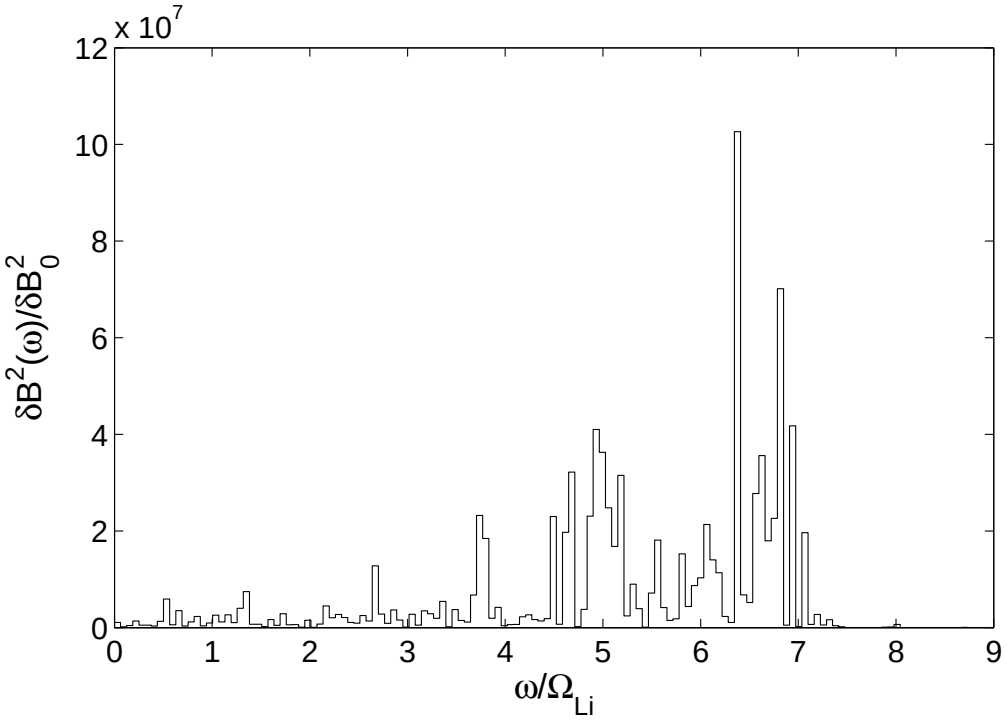

Figure 4.5: Frequency power spectrum of the magnetic field B_y component shows that no dominant Alfven modes are generated in the case with no lithium ring plasma.

This density motion indicates that the initially generated waves are shear Alfven waves whose density motion is transverse to the propagation direction and therefore along the magnetic field in this case. This series of key signatures are consistent with a quasi-electrostatic short perpendicular wavelength shear Alfven waves amplified at lithium cyclotron harmonics.

In the nonlinear evolution after saturating at time $\Omega_H t = 150$, much lower frequency oscillations, which are also pointed out in the Fig. 4.6(a), gradually begin to be observed and dominate in the magnetic field energy and electromagnetic component of electric field energy. These oscillations can be shown to be in the range of ordinary shear Alfven waves that satisfy the dispersion relation in Eq. (2.13) quite well. On the other hand, there are no further structures developed in electrostatic component which is gradually reabsorbed by the rotating lithium. It indicates the transforming from quasi-electrostatic waves into electromagnetic waves. Besides, comparing with the electric field energy, the magnetic field energy is much bigger and the lower frequency oscillations are more obvious. Therefore, the fluctuating magnetic field stores most of the energy in nonlinear period. Figure 4.9 shows the fluctuating magnetic field and the density structures at $\Omega_H t = 500$. The waves are observed to form much longer wavelength in both parallel and perpendicular direction as shown in the snapshot of the magnetic field Fig. 4.9(a). The wave front indicates that the longer wavelength wave propagates in less perpendicular direction that it has initially, which

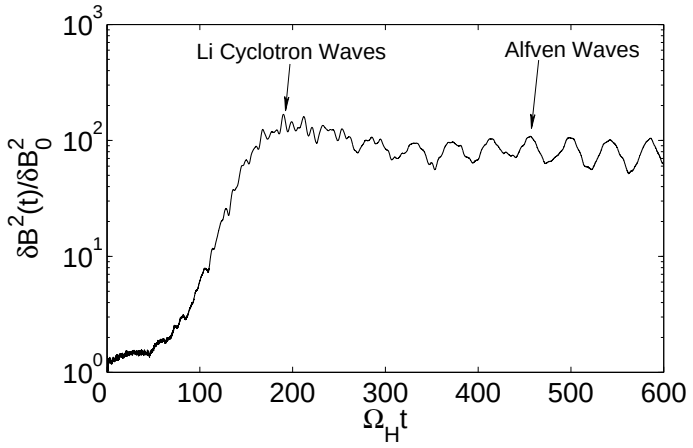

(a) Magnetic field energy.

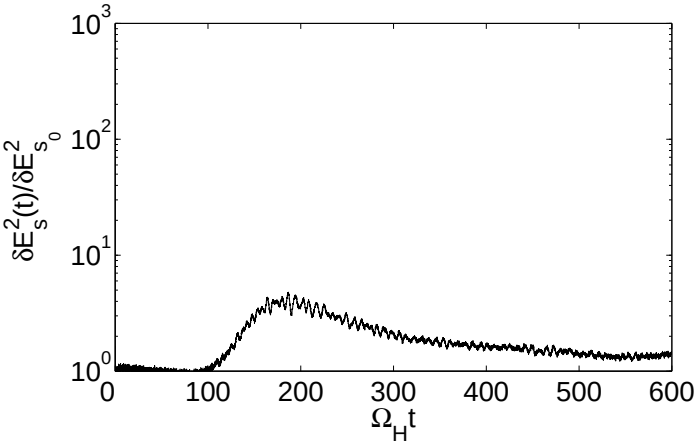

(b) Electrostatic component of electric field energy.

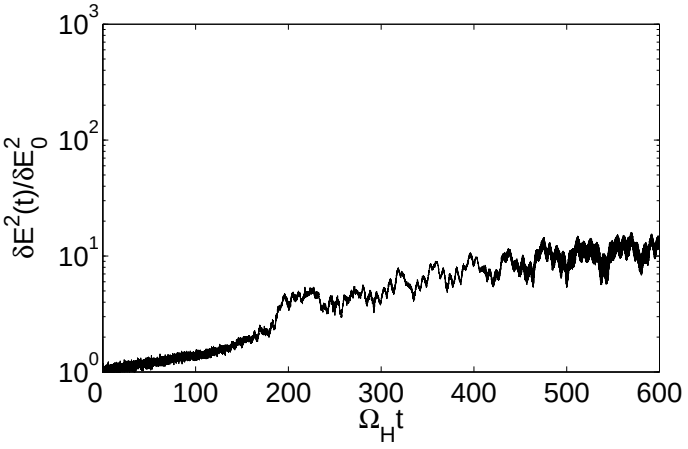

(c) Electromagnetic component of electric field energy.

Figure 4.6: Field energy time history shows initial development of lithium cyclotron harmonic waves and subsequent generation of oblique shear Alfven waves.

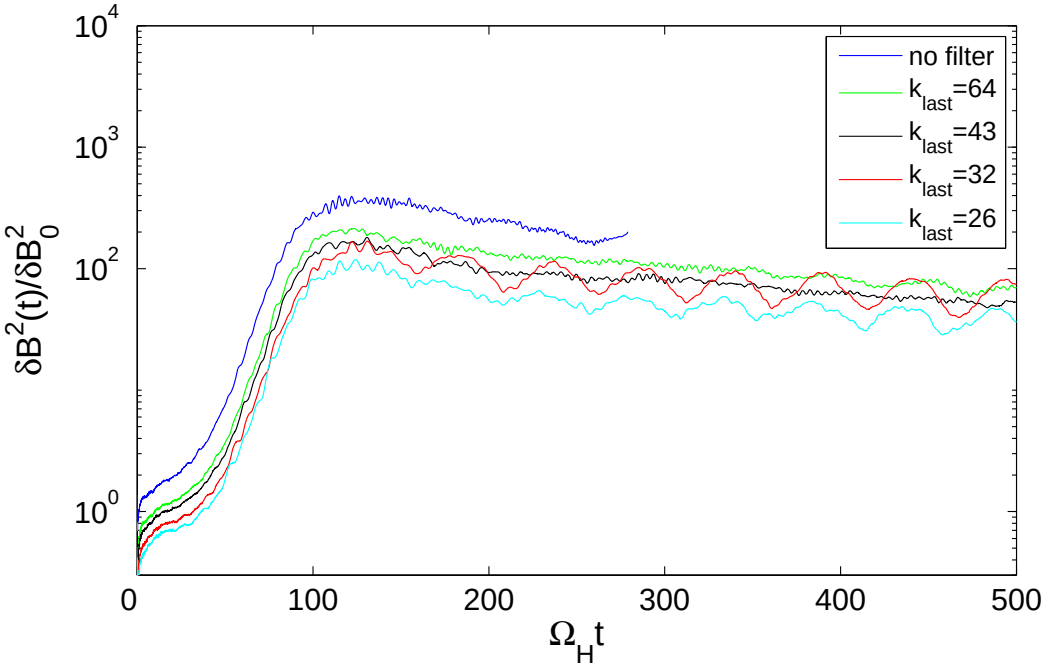

Figure 4.7: Magnetic field energy time history of 30% ring density ratio cases with different spectral filter parameter k_{last} (normalized to the case with no filter).

is consistent with the theory prediction. The density structures Fig. 4.9(b) also show oscillations less along the background magnetic field and more across the field while the larger scale structure begins to form, which also indicates the shifting of propagation direction to less perpendicular direction as the ion motions are always transverse to the wave propagation for shear Alfven waves. Therefore, the nonlinear evolution converts the initial quasi-electrostatic waves into electromagnetic waves with lower frequency and longer wavelength propagating less perpendicular to the background magnetic field.

Using spectral methods, we could transform the simulation results into Fourier domain as functions of frequency and wavenumber. Information in Fourier domains provides more insights on the ring velocity instability and the evolution of the shear Alfven waves. Figure 4.10 shows the frequency power spectrum of the dominant fluctuating magnetic field B_y component taken during three time periods in the logarithm scale. The first time period $0 < \Omega_H t < 200$ is taken during the linear growth. The spectrum shows power at harmonics of the lithium cyclotron frequency. This power is particularly enhanced at the first three harmonics which is in agreement with the predictions of linear theory in Fig. 2.7. The next period $0 < \Omega_H t < 300$ is taken during the initial saturation of the waves. Lower frequency waves are observed as well as the waves near the lithium cyclotron harmonics. The low frequency waves are found to satisfy the dispersion relation of shear Alfven waves quite well. The final spectrum is taken over the entire time of the simulation $0 < \Omega_H t < 600$. The

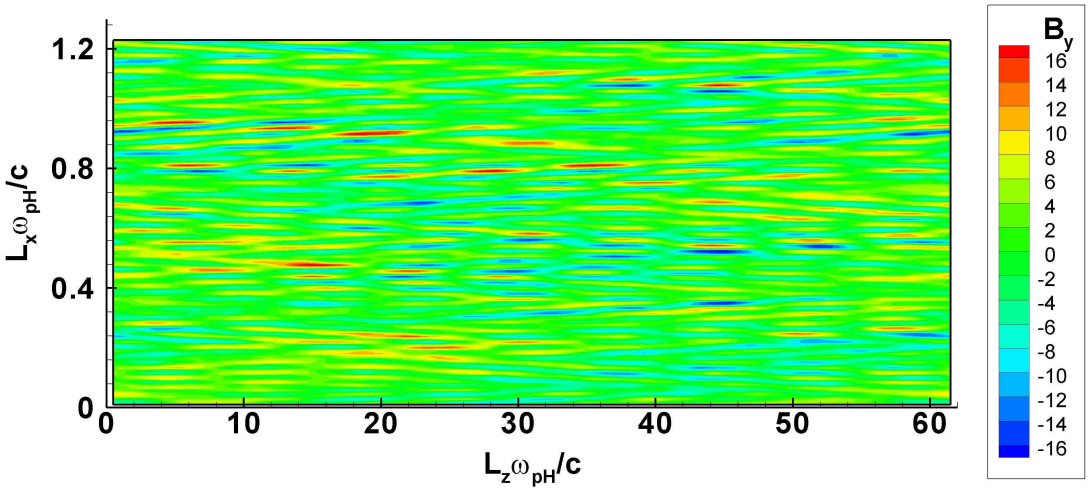

(a) The magnetic field B_y (the biggest fluctuating component) at time $\Omega_H t = 150$.

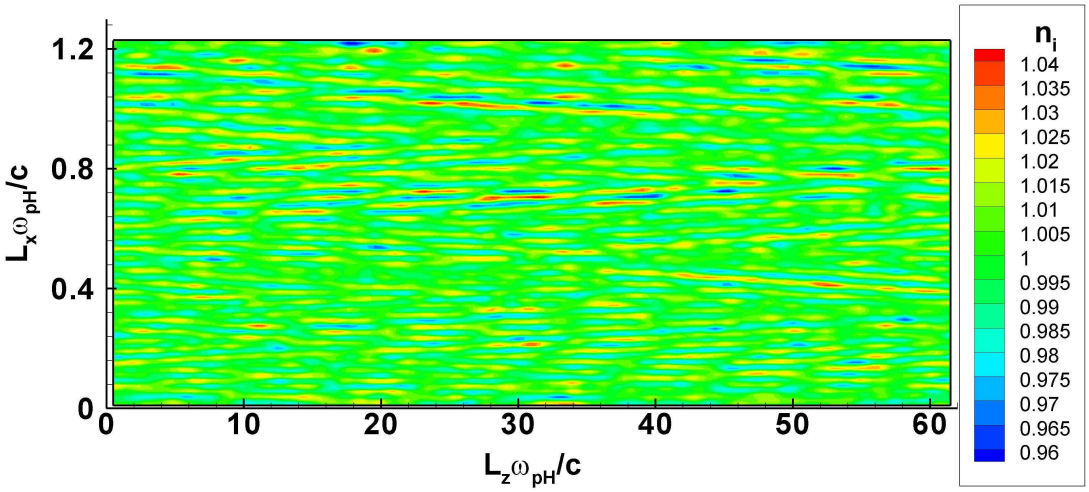

(b) The density n_i structures at time $\Omega_H t = 150$.

Figure 4.8: In linear growth period, fluctuating magnetic field and density show short perpendicular wavelength modes oscillating more along the background magnetic field.

whole time period spectrum shows that the low frequency waves near the shear Alfven frequency dominate the spectrum. This could be observed more clearly in the enlarged view of power spectrum in linear scale shown in Fig. 4.11. Note that the scale on the time period $0 < \Omega_H t < 600$ of Fig. 4.11 is one magnitude larger than that of the earlier two periods. This indicates that most of field energy is stored in the lower frequency shear Alfven waves which are generated due to nonlinear wave-wave processes, while the initial quasi-electrostatic waves near the lithium cyclotron harmonics contain relatively less energy. In general, from power spectrum, an evolution of the initially generated waves near the lithium cyclotron harmonics to lower frequency shear Alfven waves is observed, which is correspondent to the field energy

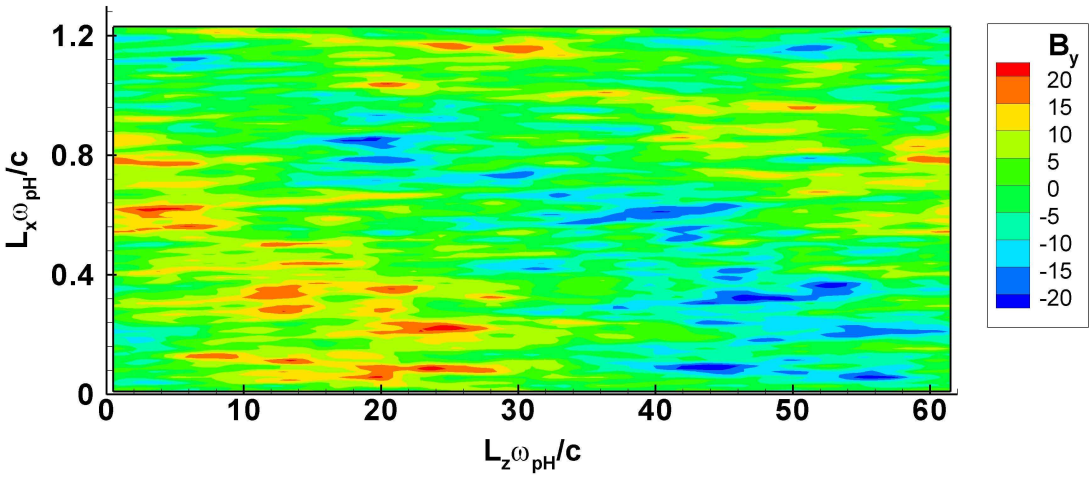

(a) The magnetic field B_y (the biggest fluctuating component) at time $\Omega_H t = 500$.

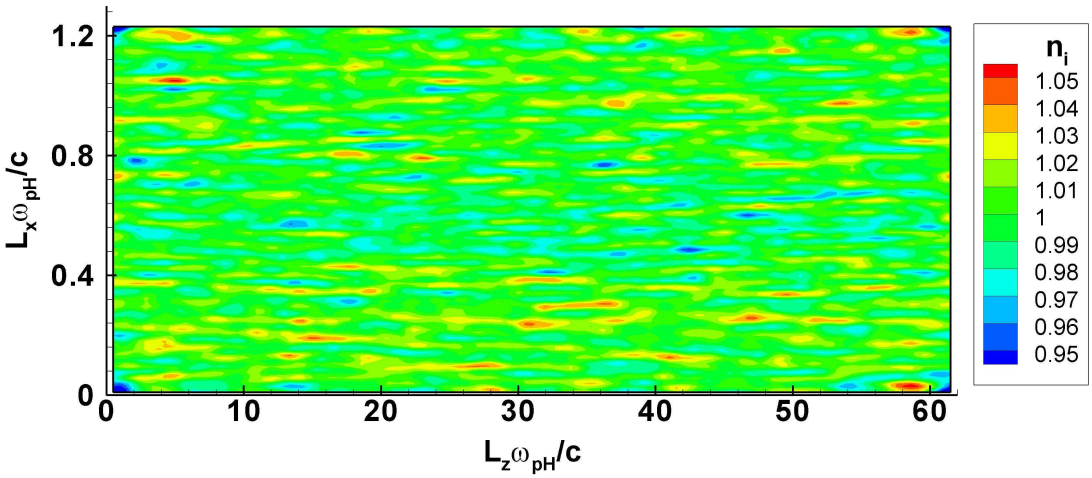

(b) The density n_i structures at time $\Omega_H t = 500$.

Figure 4.9: In nonlinear evolution, fluctuating magnetic field and density show longer wavelength modes oscillating more across the background magnetic field.

time history shown previously in Fig. 4.6.

To examine the wave interactions in more detail, snapshots of wavenumber spectra are taken, shown in Fig. 4.12 at three fixed times which are $\Omega_H t = 100, 200$ and 600. During the linear growth period ($\Omega_H t = 100$), power is observed at three distinct regions in wavenumber space which correspond to the first three lithium cyclotron harmonics as predicted by linear theory. The wavenumbers for the first three harmonics from the simulation are $\ell = 1, k_x = 80, k_z = 0.25$; $\ell = 2, k_x = 130, k_z = 0.45$; $\ell = 3, k_x = 170, k_z = 0.55$. These $\vec{k}$ values are acceptable close to the values obtained from theoretical calculation shown in Fig. 2.7. Examining

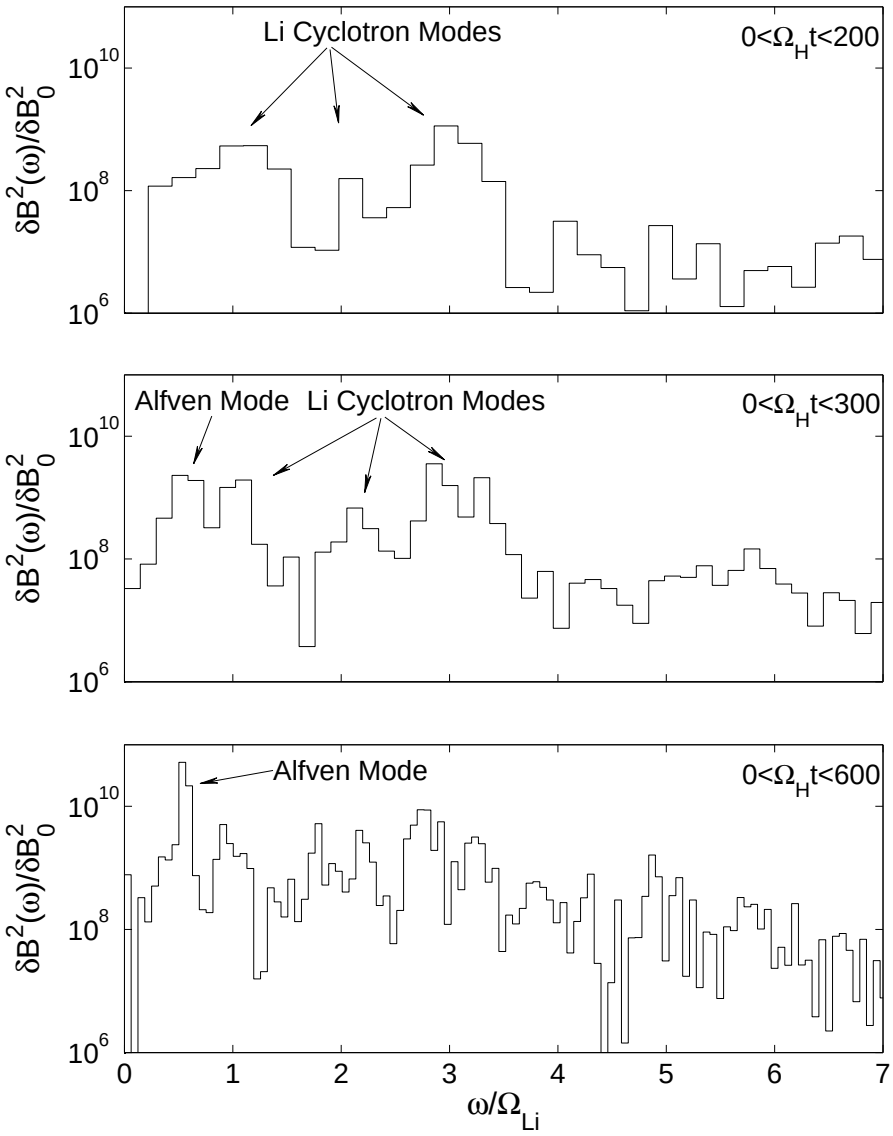

Figure 4.10: Frequency power spectrum of the magnetic field B_y component shows initial development of lithium cyclotron harmonic modes and subsequent development of lower frequency shear Alfven modes.

the ratio of k_x/k_z which is around 300, we found that these cyclotron harmonic modes are perpendicular propagating, corresponding to the magnetic field snapshot of Fig. 4.8(a). This in turn verifies the accuracy of our hybrid model. After nonlinear saturation ($\Omega_H t = 200$), in addition to the cyclotron harmonic modes, a mode with much longer perpendicular wavelength is observed which is interpreted as a shear Alfven wave. The spectrum at the end of the simulation shows a wave propagating relatively less perpendicular to the magnetic field with a substantially longer wavelength interpreted as a shear Alfven wave. The wavenumbers

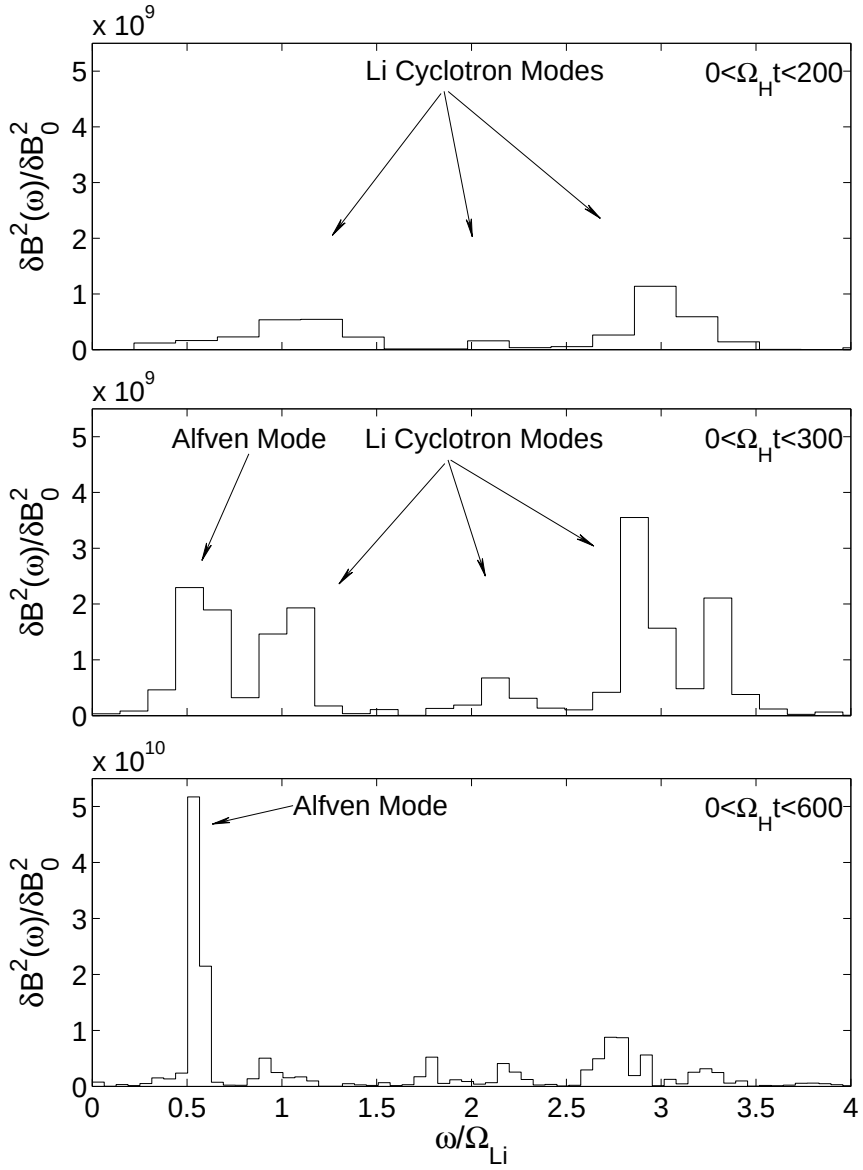

Figure 4.11: The enlarged view of frequency power spectrum from harmonic $\ell = 1$ to $\ell = 4$ in linear scale.(Note change in vertical scale for $0 < \Omega_H t < 600$.)

for the Alfven mode is about $k_x = 5, k_z = 0.1$ and the ratio of k_x/k_z decreases to 50. The perpendicular wavelength thus increases more than a factor of 30 comparing with initial cyclotron harmonic modes. Again, the wavenumber spectrum of the longer wavelength modes is consistent with the magnetic field snapshot of Fig. 4.9(a). From the color contour of the wavenumber spectra, we also notice that the longer wavelength shear Alfven modes store more energy than the cyclotron harmonic modes, which corresponds to the frequency power spectrums. Such longer wavelength waves then dominate the spectrum as we checked several other power spectrums at different time after the wave amplitude has saturated.

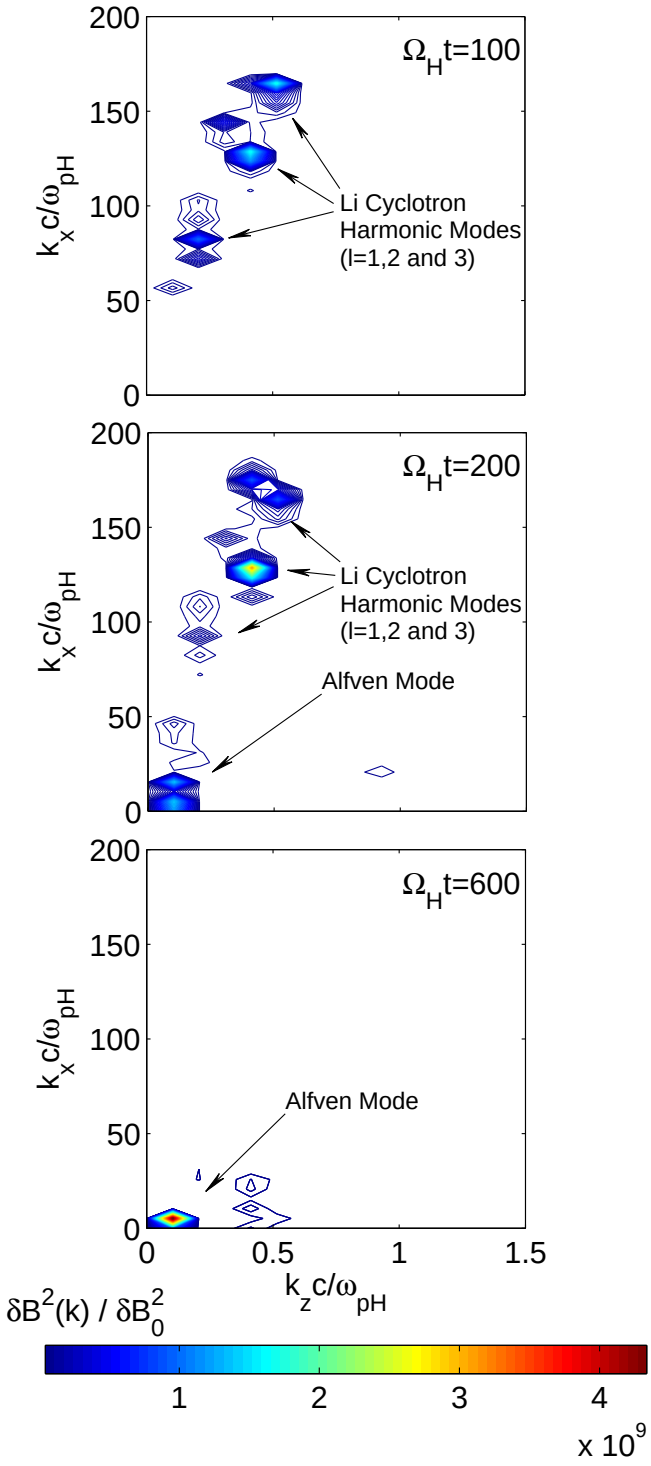

Figure 4.12: Wavenumber spectrum of B_y shows initial development of shorter wavelength lithium harmonic modes and subsequent development of longer wavelength Alfven modes.

Comparison of the both frequency and wavenumber to the dispersion relation of oblique shear Alfven waves Eq. (2.13) shows quite a good agreement. Therefore the results from both real space domain and Fourier domain indicate an initial generation of waves near lithium cyclotron harmonic frequencies and the subsequent development of these higher frequency short wavelength perpendicular propagating waves into obliquely propagating shear Alfven waves with much longer wavelengths both parallel and perpendicular to the background magnetic field. Although the waves in the saturated state still propagate nearly perpendicular ($k_x/k_z = 50$) to the magnetic field by the end of the simulation, they propagate less perpendicularly than the initially generated cyclotron waves ($k_x/k_z = 300$). The size of the simulation domain plays a critical role in restricting the development of longer wavelengths. In the saturated state, it is observed that the perpendicular wavelength typically becomes as large as the system length L_x which means the dominant mode number is 1. This has been verified with several test cases of increasing the perpendicular system length L_x which shows development of longer perpendicular wavelengths and decreasing k_x/k_z although still $k_x/k_z > 1$. Figure 4.13 shows the magnetic field snapshot in the saturated state for a test case with double perpendicular system length. Compared with Fig. 4.9(a), it shows the shear Alfven wave develops to further longer wavelength and propagate even less perpendicular ($k_x/k_z = 25$). This indicates that if a large enough simulation domain is utilized, k_x might develop to become of similar magnitude as k_z as predicted by Ref. [15]. Based on current simulation results, to contain a few (5) wavelengths in both Z and X directions, L_z has to be increased by a factor of 5, and L_x should be as large as L_z. Therefore the domain size needs to be expanded by 1250 times. On the same time, enough resolution in the X direction for the initial growth of short wavelength cyclotron modes has to be maintained. If particles per cell remains unchanged, and we sacrifice a little resolution (a factor of 4) in Z direction for the sake of computational efficiency, the estimated computational cost (memory, cpu time, etc) would be increased by a factor of 312.5 over the current level. However, such computing resources is beyond what is utilized for this investigation and may be the subject of future work. The current model is thus unable to investigate further nonlinear processes predicted to occur on much larger spatial scales than considered here.

The previous results indicate important nonlinear properties involving nonlinear wave-wave processes. The results to be presented next provide insight on the wave-particle interactions and the anomalous transport processes. Figure 4.14 shows the velocity phase space of the hydrogen and lithium ions at three fixed times during the simulation which are $\Omega_H t = 100, 150$ and 250. It is observed that there is relatively little wave-particle heating of the hydrogen ions. On the contrary, the ring velocity lithium particles are thermalized quickly. Initially the lithium is a cold ring, whose velocity equals the spacecraft orbit velocity. At $\Omega_H t = 150$, the lithium ring experiences slowing down as the results of the heating of lithium particles by lithium hydrogen collision. Comparing with the field energy growth of Fig. 4.6, we find that initially there is no threshold for the instability; but as the thermal lithium population increases, there is a threshold (around $\Omega_H t = 150$) which determines the growth rate and indicates the transform from quasi-linear to nonlinear saturated state. Such an impact on wave growth could be modeled by combing thermal lithium contribution in the

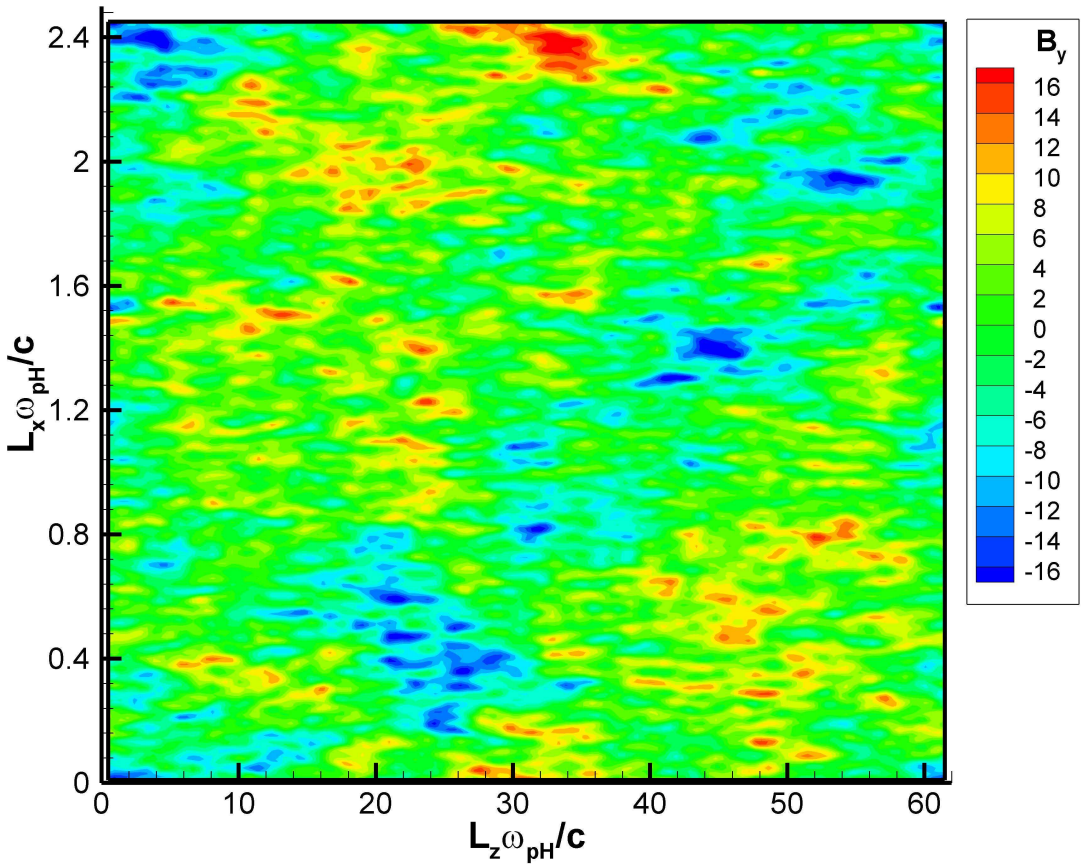

Figure 4.13: Fluctuating magnetic field of a test case with double perpendicular system length shows that the initial cyclotron waves have potentials to develop to further longer wavelength in the nonlinear evolution.

dispersion relations shown in Eq. (4.1).

$$\begin{aligned} D(\omega,k) = & \frac{k_z^2 V_A^2}{\omega^2}(1+\frac{k_x^2c^2}{\omega_{pe}^2}\frac{1}{\zeta^2 Z'(\zeta)})^{-1} \\ & -\sum_\ell \frac{\ell^2\Omega_H^2}{\ell^2\Omega_H^2-\omega^2}\frac{2\Gamma_\ell(b_H)}{b_H} \\ & +\sum_\ell \frac{n_{Li}m_{Li}}{n_H m_H}\frac{dJ_\ell^2(\sigma_s)}{\sigma_s d\sigma_s}\frac{\ell^2\Omega_{Li}^2}{\omega(\omega-\ell\Omega_{Li})}(1+\frac{n_{Lit}}{n_{Li}}\frac{2\Gamma_l(b_{Lit})}{b_{Lit}}\frac{1}{dJ_\ell^2(\sigma_s)/\sigma_s d\sigma_s}) \\ & =0 \end{aligned} \tag{4.1}$$

where the subscript *Lit* indicate thermalized lithium quantities. After the saturated point,

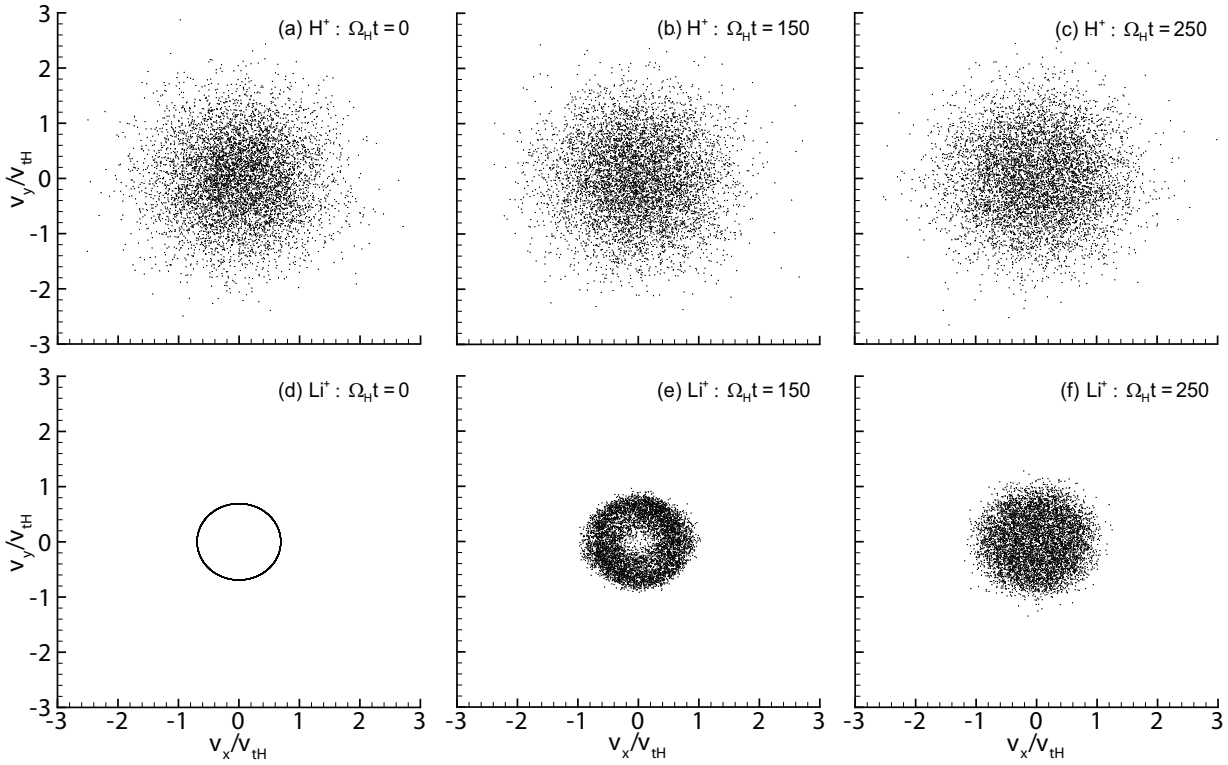

Figure 4.14: Hydrogen and lithium phase spaces at $\Omega_H t = 0$, 150, 250.

the lithium particles continue to be thermalized and the lithium ring gradually fades away that would no longer drive instability shown in Fig. 4.14(f). This represents the entering into the steady nonlinear saturated state.

Distribution functions in v_x and $v_\perp$ for the ions at corresponding times are shown in Fig. 4.15. Consistent with the velocity phase, the background hydrogen ions experience only some tail heating while the lithium ring ions slow down and exhibit bulk heating in Fig. 4.15(a) and Fig. 4.15(b), respectively. At $\Omega_H t = 250$, the initial ring velocity distribution has totally vanished and the lithium particles has become the quasi-maxwellian distribution. In Fig. 4.15(c), the evolution of the lithium ring can be observed more clearly. The ring particles perpendicular velocity $v_\perp$ initially focus on the ring velocity v_r and gradually expand to both directions with more population having a much smaller $v_\perp$ due the loss of momentum in collision with hydrogen. This anomalous transport process ultimately results in the thermalized lithium ring and the maxwellianized distribution functions corresponding with Fig. 4.14(f) and 4.15(b), respectively.

An important consequence of the wave-particle interactions is the extraction of free energy of the ring particles into the generation of the waves. The amount of energy extracted from the ring lithium can be quantified by considering the temporal evolution of the lithium kinetic energy which is shown in Fig. 4.16(a). Part of the free energy is used to drive the instability

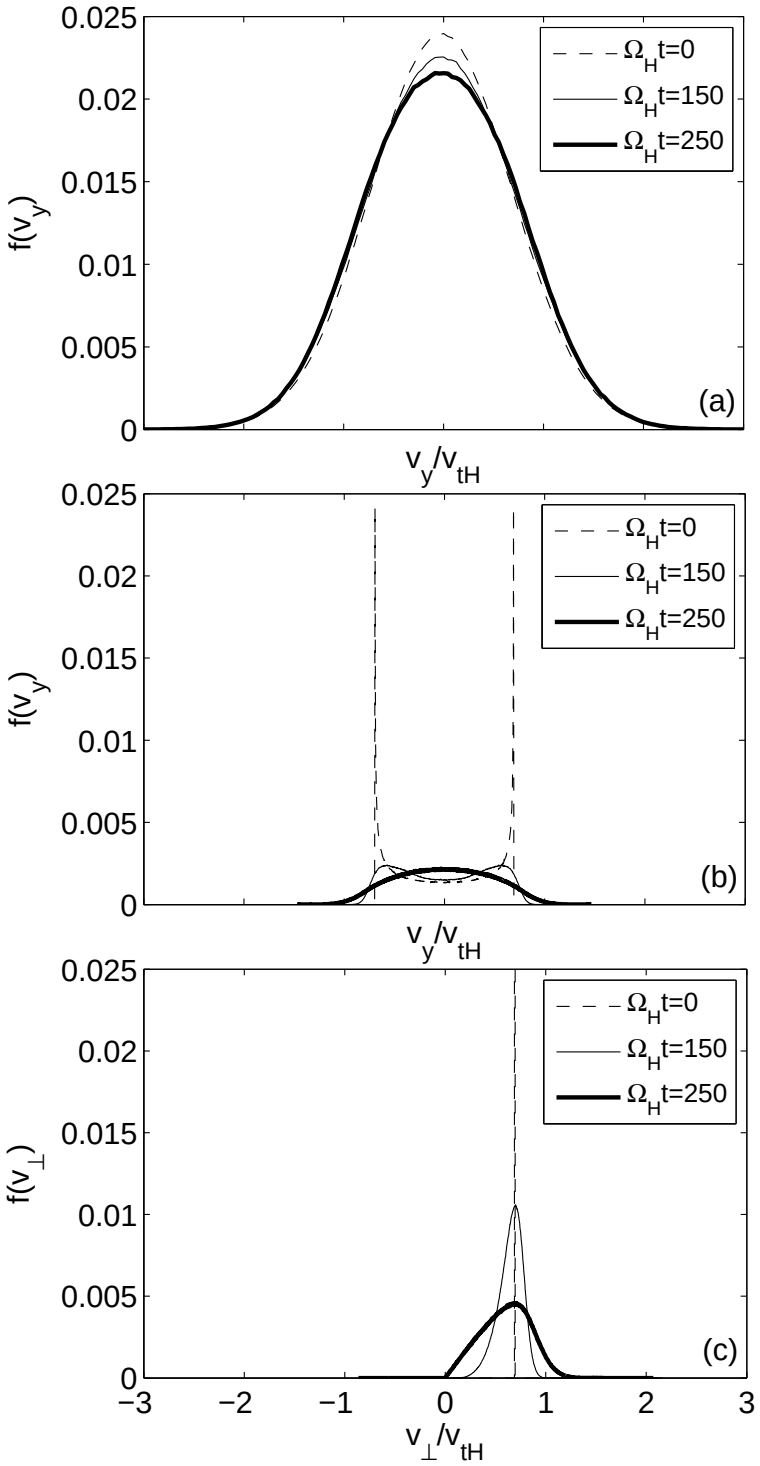

Figure 4.15: Hydrogen and lithium velocity distribution functions at $\Omega_H t = 0$, 150, 250.

and sustain electromagnetic waves and the total lithium energy decrease initially. It can be observed that roughly 20% of the energy is extracted from the lithium ring ions at the time of saturation. However, as the thermal lithium population grows up, the increase of the energy extraction rate is observed to slow down. This is due to the fact that part of the free energy has been utilized by the anomalous transport process of lithium hydrogen collision to thermalize the cold lithium ions as observed in phase space and distribution functions. Finally there is no more free energy that could be drawn to support the continuous growth of the waves and the lithium kinetic energy starts to increase after the saturation point as the continuous thermalization of the lithium particles. Therefore, the time history of lithium kinetic energy is controlled by such two mechanisms and the final energy extraction rate from the lithium ions are around 12% in steady state for this 10% ring density benchmark case. Possibilities of controlling the amount of energy reabsorbed by the ring particles will be discussed in section 4.3.

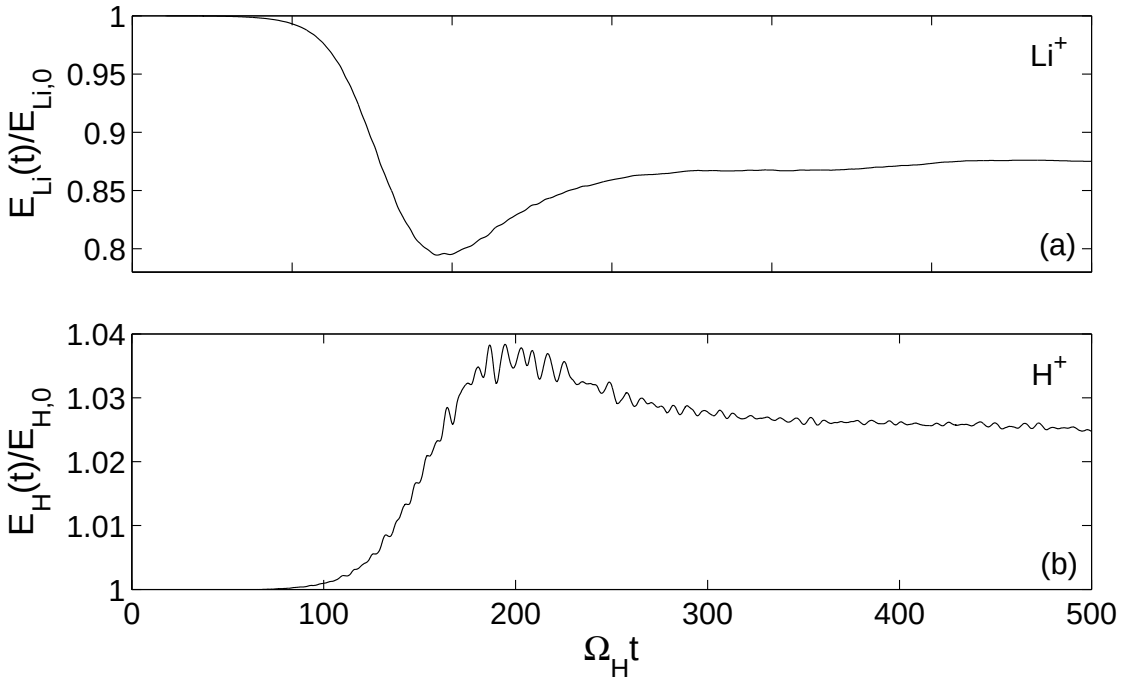

Figure 4.16: Lithium and hydrogen kinetic energy time evolution.

The energy that goes into heating the background hydrogen ions is also shown for comparison in Fig. 4.16(b). It is observed that there is a relatively small percentage increase in the hydrogen kinetic energy from wave-particle heating in the linear growth period. This amount of gained energy is much larger than the field energy, which indicates that the initial energy of these waves is largely in the kinetic energy of the particle described by the linear theory. As the nonlinear evolution goes on, the kinetic energy of hydrogen experience a small decrease about 1% for the benchmark case. Recall that power and wavenumber spectrums (Fig. 4.10

and 4.12) show much stronger lower frequency shear Alfven waves in the nonlinear state. Combining these two points indicates the trend of transferring energy from particles into fields compared with initial cyclotron harmonic waves. However, since the limited domain size restrict the further development of the waves, the electromagnetic waves which are predicted by Ref. [15] having energy equally partitioned in the fields and particles could not be observed in current simulations.

4.3 Variation with ring density

An important question related to the nonlinear evolution of the ion cyclotron waves generated by the ring plasma instability is the condition under which these waves evolve nonlinearly into lower frequency shear Alfven waves. It has been predicted [15] that if the waves are of sufficient amplitude that the process observed in the previous section may occur. From a practical standpoint, it is useful to consider how the strength of the perturbation, i.e., ring plasma density, is related to the nonlinear evolution. Linear theory calculations in the section 2.2.2 for ring plasma densities from 1% to 30% of the background density predict initial generation of the ion cyclotron waves. However, it is of importance to see if the longer wavelength shear Alfven waves are generated after the nonlinear saturation upon varying the ring density.

A series of simulations were performed with varying ring plasma density to consider this question. Figure 4.17(a) shows the time evolution of the magnetic field energy and energy extraction from the ring plasma for four values of ring density, 30%, 10%, 5% and 1%. These different density ratio cases are observed to be consistent with the growth rate obtained by the linear theory. The high 30% density case shows that the ion cyclotron waves quickly evolve into the lower frequency shear Alfven waves after the nonlinear saturation. Its frequency power spectrum and wavenumber spectrum, shown in Fig. 4.18(a) and 4.18(b) respectively, also confirm that the frequency and wavenumber satisfy the dispersion relation. In the 30% density case, the shear Alfven mode is very strong since the energy is more than one magnitude larger than that of the cyclotron harmonic modes. The 10% ring density case (described in detail in the previous section) shows a somewhat slower evolution of the ion cyclotron waves into the shear Alfven waves.

As the ring density is further decreased to 5%, it becomes clear that it takes much longer for the shear Alfven waves to appear. Besides, high frequency oscillation near lithium cyclotron harmonics are found coupled with the lower frequency oscillations as shown at the later times of the field energy time history. A power spectrum Fig. 4.19(a) shows proofs of such observation since the Alfven waves are much smaller in amplitude than in the previous cases and comparable to the cyclotron harmonic waves. Correspondingly, the wavenumber spectrum Fig. 4.19(b) appears to be much more noisy compared with higher density cases, showing several longer wavelength modes around the dominant Alfven mode.

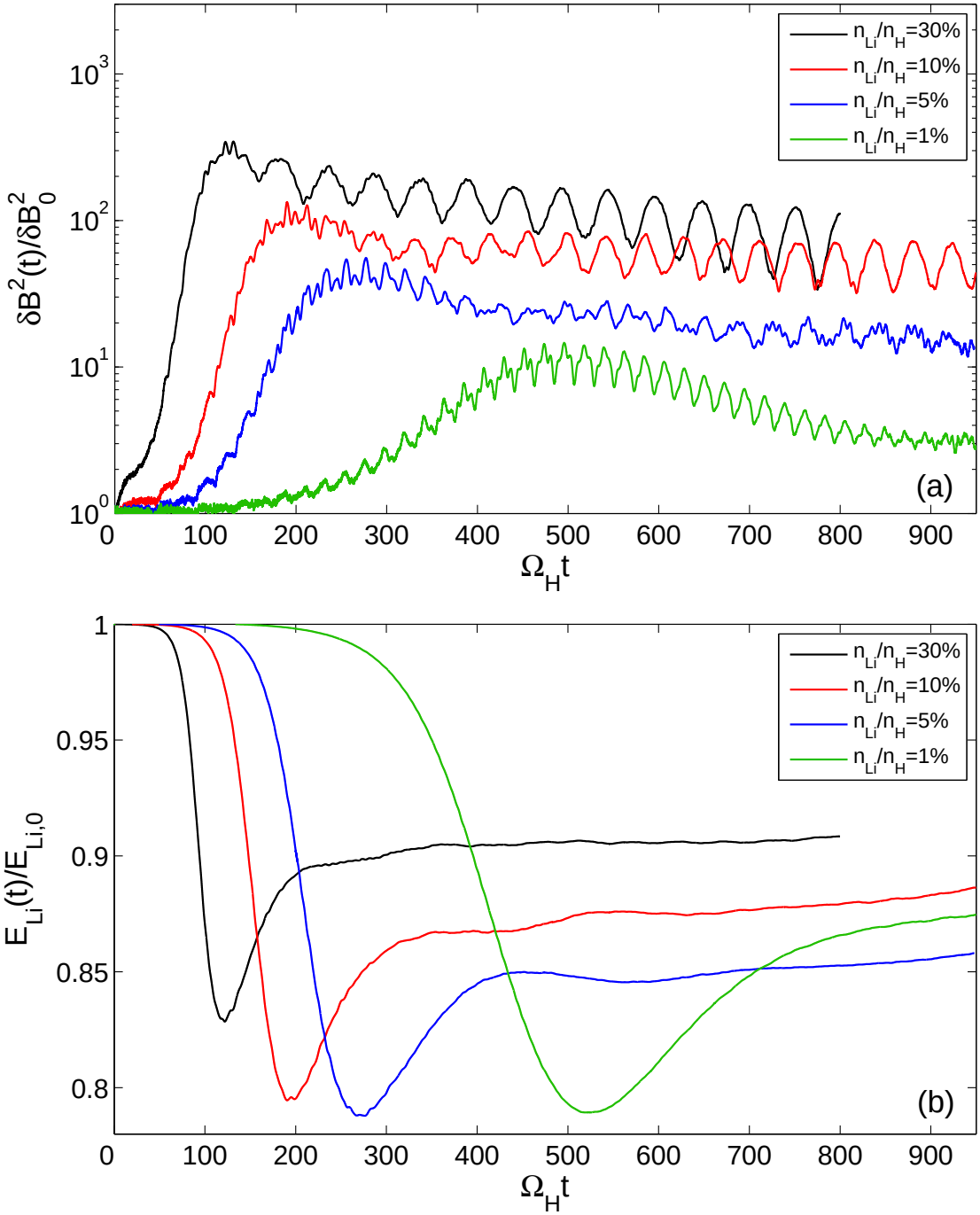

Figure 4.17: Effect of varying ring plasma density ratio n_{Li}/n_H on magnetic field energy and ring kinetic energy. Lower frequency and longer wavelength shear Alfven waves result from sufficiently large density ratios.

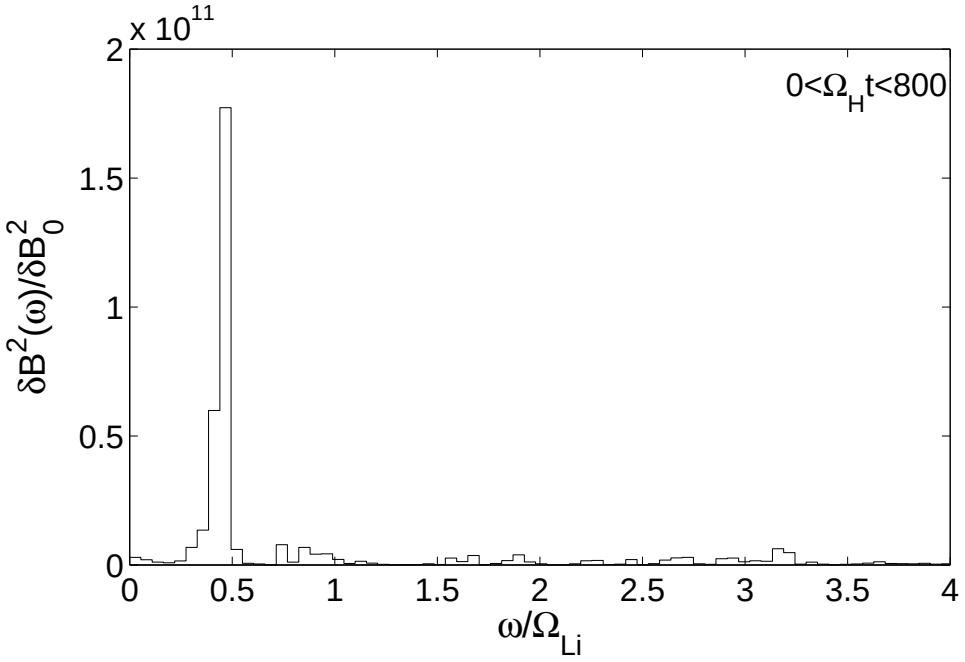

(a) Frequency power spectrum for 30% ring plasma density ratio case.

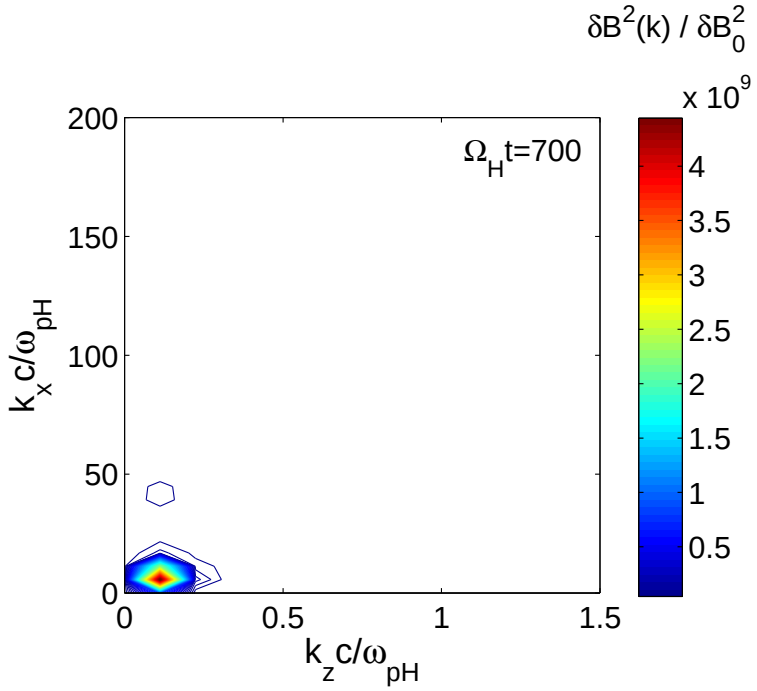

(b) Wavenumber spectrum for 30% ring plasma density ratio case.

Figure 4.18: Power and wavenumber spectra show the evolution into a dominant lower frequency longer wavelength shear Alfven mode in nonlinear period for 30% ring plasma density ratio case.

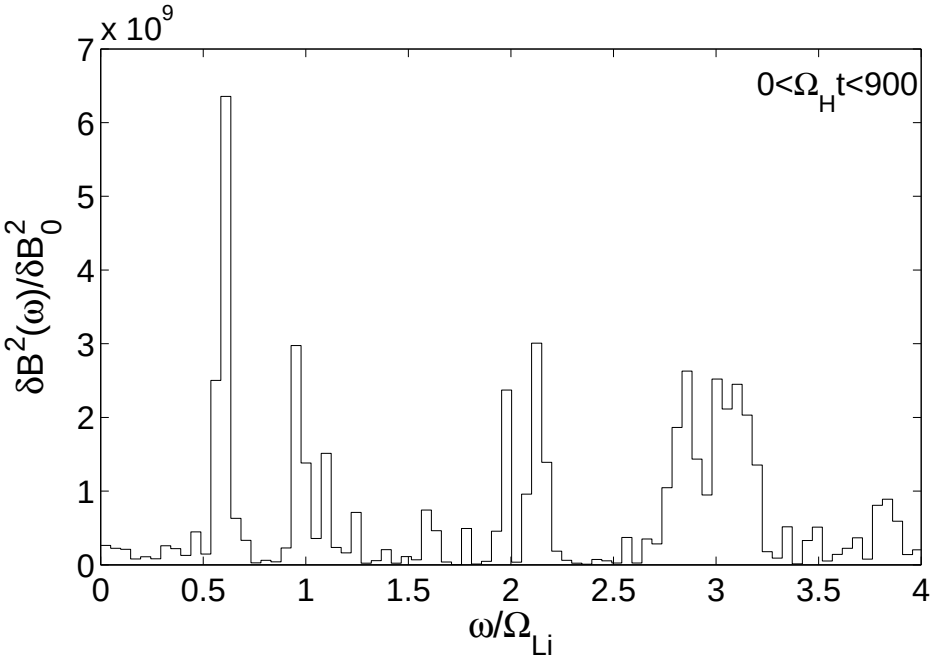

(a) Frequency power spectrum for 5% ring plasma density ratio case.

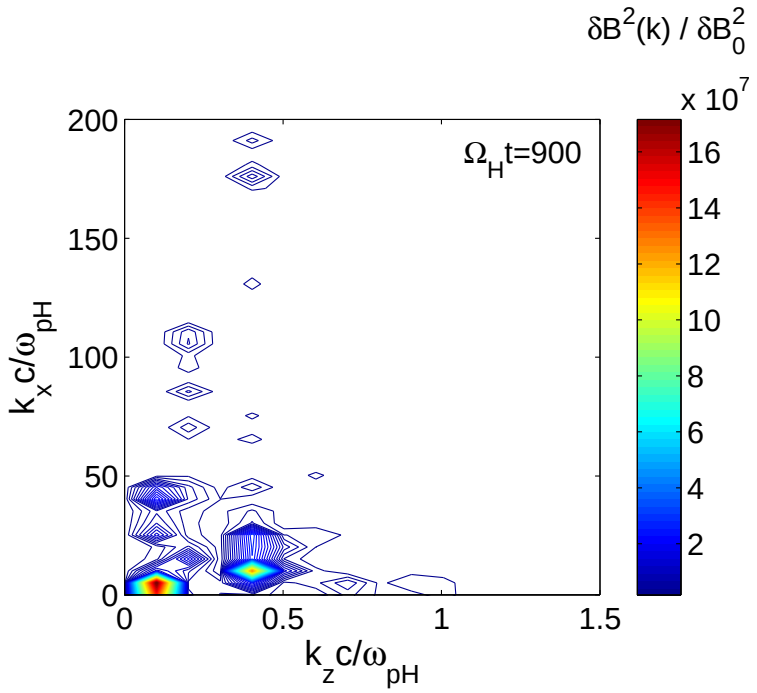

(b) Wavenumber spectrum for 5% ring plasma density ratio case.

Figure 4.19: Power and wavenumber spectra show the evolution into a weak shear Alfven mode in nonlinear period for 5% ring plasma density ratio case.

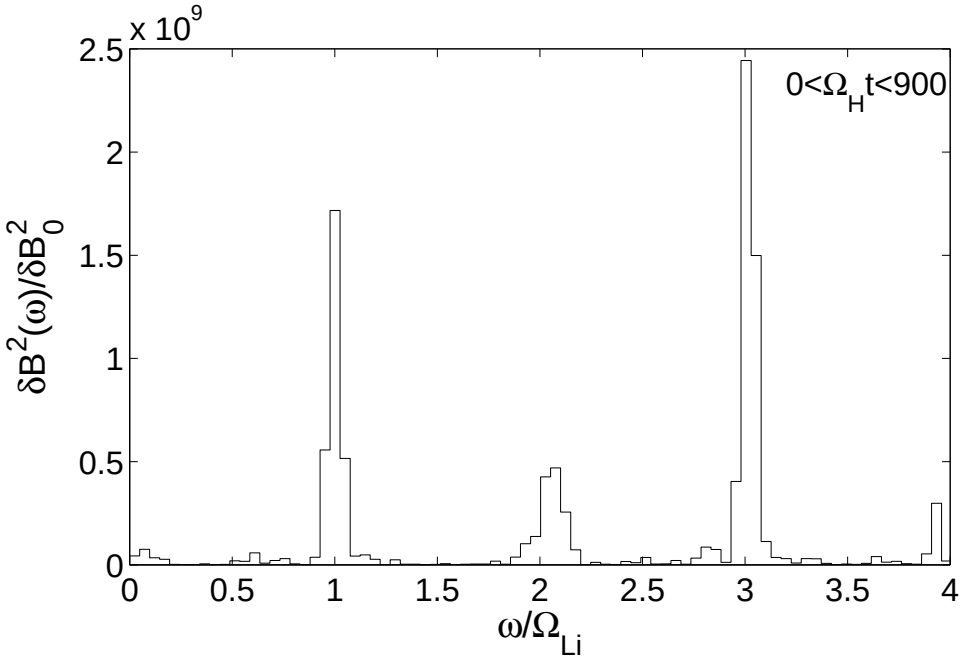

(a) Frequency power spectrum for 1% ring plasma density ratio case.

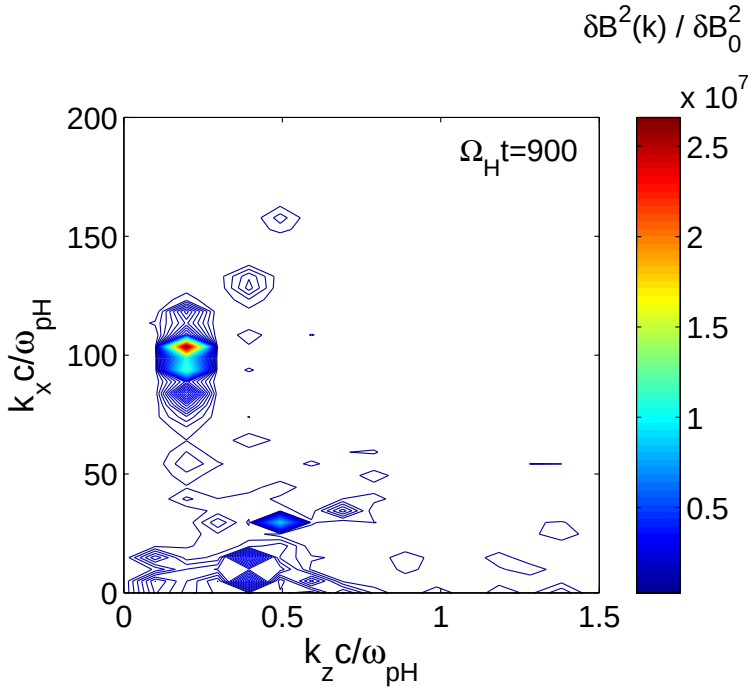

(b) Wavenumber spectrum for 1% ring plasma density ratio case.

Figure 4.20: Power and wavenumber spectra show no evolution into a lower frequency longer wavelength shear Alfven mode for 1% ring plasma density ratio case.

The low 1% density case shows no generation of lower frequency Alfven waves from the field energy time history as well as frequency and wavenumber spectra, shown in Fig. 4.20(a) and 4.20(b), respectively. It can be observed from both spectra that short wavelength modes near the cyclotron harmonics are dominant modes. The harmonic $\ell = 1$ dominates in the wavenumber spectrum, which is consistent with the linear theory prediction in Fig. 2.7. Like the 5% density case, several weak longer wavelength modes are generated in the wavenumber spectrum due to the relatively high noise level for this low density ratio case.

In general, the linear theory predictions are in good agreement with the simulations during the initial growth phase. Increasing the ring density, for the parameter range under consideration, shows a trend to enhance the field energy growth and result in stronger longer wavelength shear Alfven waves. However, a high density ratio does not necessarily mean a higher percentage of energy drawn from the ring plasma. Among all the cases shown here, 5% ring density has the highest energy extraction rate, which is about 15% in steady nonlinear stage shown in the Fig. 4.17(b). Again note that the variation of lithium kinetic energy is affected by two mechanisms: wave-particle interaction tends to draw the free energy of lithium ring to excite waves; lithium hydrogen collision tends to utilize the free energy to thermalize the cold ring. The 5% ring density may has less free energy to be drawn compared with higher density cases, but also has less lithium ions to be thermalized. The optimization of such two opposite effects turns out that the 5% case has the highest energy extraction rate under the current simulation parameters. The corresponding evolution of the background hydrogen ion kinetic energy is shown in Fig. 4.21, which indicates that an extra energy goes into heating the background hydrogen as the ring density increases. However, judging from the 30% to 1% lithium cases, there is not a large difference of energy extraction rate, which is in the range of 10-15%. Therefore, from a practical standpoint, one may still want to consider dumping as much lithium chemical as possible to sustain a stronger wave growth.

Since the simulation above show that an approximate 10% energy is deposited into the wave energy in the nonlinear saturated state, we may apply it to evaluate the efficiency of pitch angle scattering radiation belt particles through the theoretical model Eq. (2.19). This shows that a large enough change of pitch angle could be reached for efficient pitch angle scattering. Although such evaluation may be not precise since the further nonlinear development of much longer shear Alfven waves could not be observed in current simulation, the qualitative results indicate the suitability and viability of the nonlinearly generated shear Alfven waves for applications to radiation belt remediation.

4.4 Effect of electron resistivity on energy extraction

It is observed that the extraction of energy from the ring ions maximizes near the time of wave saturation. After this time some of the wave energy is reabsorbed by the ring ions. The efficiency of lithium ring energy extraction is then reduced after the wave saturation. A possibility to control the amount of energy reabsorbed by the lithium is to introduce the

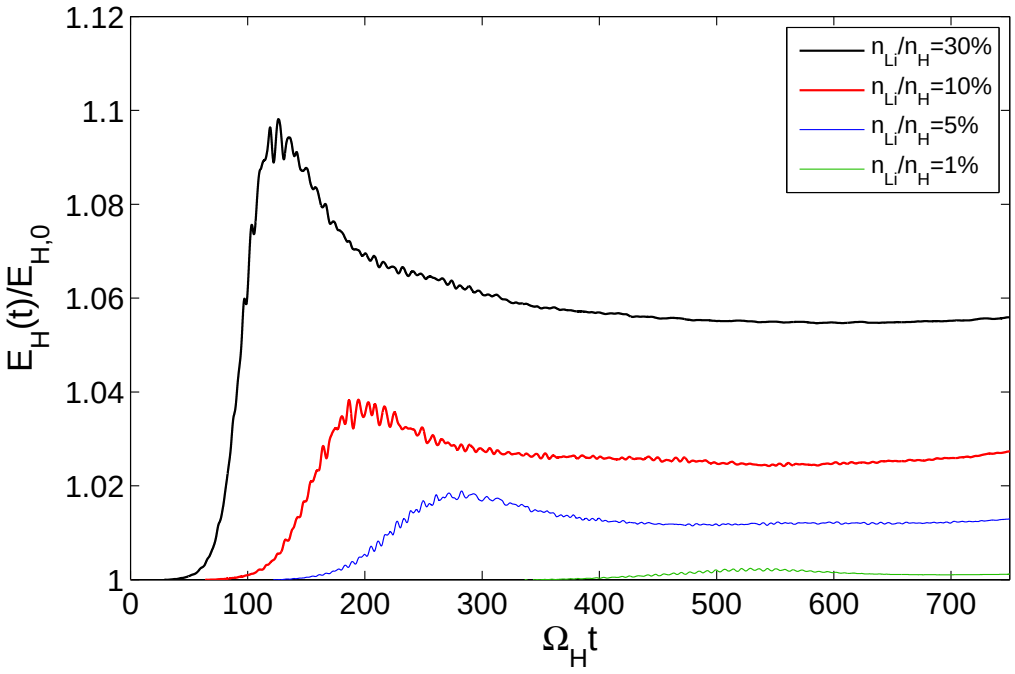

Figure 4.21: Effect of varying ring plasma density ratio n_{Li}/n_H on ambient hydrogen kinetic energy. An extra small percentage increase is observed in the hydrogen kinetic energy as the ring density increases.

effects of further nonlinear processes and electron collisions. However, the previous cases do not include any physical collision with electrons since the simulation model incorporates fluid electrons for the sake of computational efficiency. To model such effects which may have influence on the extraction of energy from the ring particles, the anomalous resistivity η^* on the fluid electrons is then included in the model. This anomalous resistivity η^* can be considered to model the effects of transfer of energy to other nonlinear processes or convection out of the system, i.e., it could be used to evaluate the impact of the further nonlinear coalescence of the longer wavelength shear Alfven waves which is not able to simulate in current model due to the requirement of much larger spatial scale [41]. Therefore, the resistivity in the electron momentum equation (3.8) is modeled as

$$\eta = \eta_0 + \eta^* \exp(|E|^2/|E_{max}|^2) \tag{4.2}$$

where η_0 is the numerical resistivity and η^* is the anomalous resistivity with $\eta_0 \ll \eta^*$. The electric field amplitude is denoted by $|E|$ and the electric field amplitude at saturation is $|E_{max}|$ which is determined a priori by performing a simulation without the effects of anomalous resistivity such as the cases shown in previous sections. Such a model approximately describes the effects of wave-particle interactions with the fluid electrons in the simulations having an anomalous resistivity.

Figure 4.22(a) shows the results of lithium kinetic energy time history with varying the anomalous resistivity for ring plasma density $n_{Li}/n_H = 30\%$. The anomalous resistivity for the conditions under consideration is $\eta^* \sim 10^{-12}s$. Simulation results for three values $\eta^* = 10^{-12}s$, $2 \times 10^{-12}s$, and $4 \times 10^{-12}s$ are shown. It is observed that anomalous resistivity increases the efficiency of extraction from the ring ions after saturation compared to the case with no anomalous resistivity. In the largest anomalous resistivity case ($\eta^* = 4 \times 10^{-12}s$), the energy from the ring is not appreciably reabsorbed by the ring ions after saturation. There is also less heating of the background ions for cases incorporating anomalous resistivity shown in Fig. 4.22(b). As less energy is going to the lithium and hydrogen ions, it should be expected that more energy is going to the field and electrons. However, there is no extra field energy increase observed in the simulation, which could be explained by the fact that the relative small domain restricts the further nonlinear evolution which is predicted to have more field energy stored in the turbulence. Besides, incorporating anomalous resistivity enhances the anomalous electron collisions with plasma turbulence and therefore extra energy is drawn from the field to electrons. The increase of electron energy for different anomalous resistivity value is compared in Fig. 4.23. Note that the electron energy could be expressed as:

$$E_e = E_{e,0} + E_{total,0} - E_H - E_{Li} - E_{field} \tag{4.3}$$

Here $E_{e,0}$ is the initial electron energy which equals the initial hydrogen energy. As we said before, the total energy E_{total} does not include the fluid electron energy. Thus the variation of electron energy is obtained by assuming energy conservation in the entire simulation.

Although in general such model for fluid electron collision does not increase the field energy, it reduces the energy reabsorbed by the lithium ions which otherwise could never be utilized again to support the application under consideration. The increased electron energy, on the other hand, is considered as part of the wave energy and predicted to be transferred into electromagnetic field energy on much longer time and spatial scales in Ref. [15]. The importance of this result is that most likely the estimates of energy extraction efficiency after saturation from our hybrid fluid electron model are underestimated. Therefore the instability process described here may be even more effective at generating plasma turbulence in a much larger simulation domain and the pitch angle scattering of relativistic electrons might be more efficient. Of course, the model for the resistivity is rather simplified and future work will consider a more realistic model.

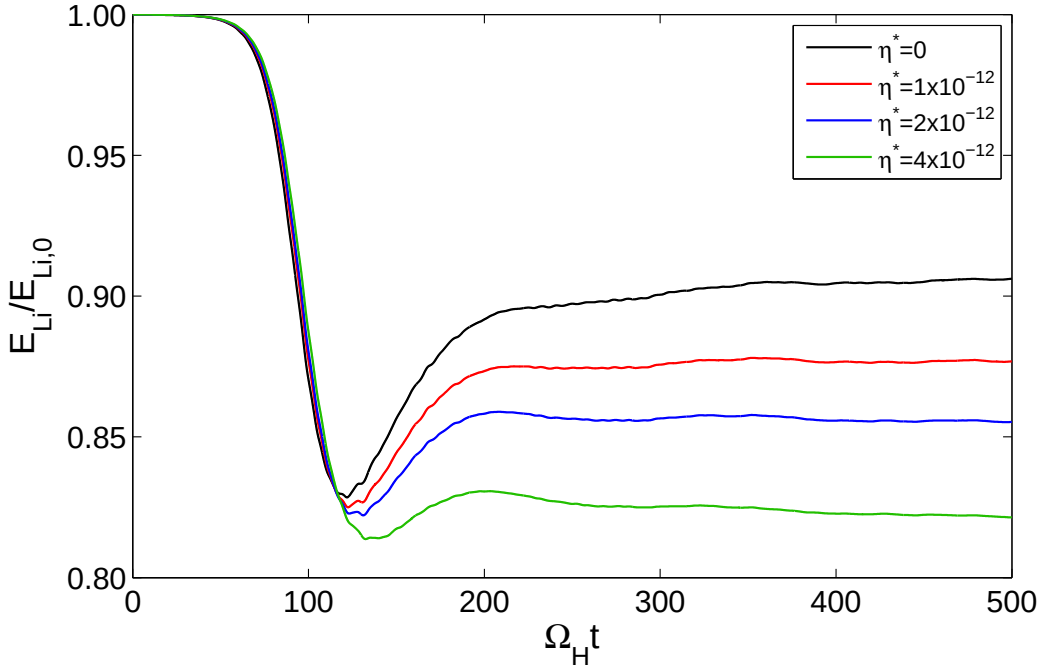

(a) Impact of varying anomalous electron resistivity η^* on lithium kinetic energy extraction after wave saturation.

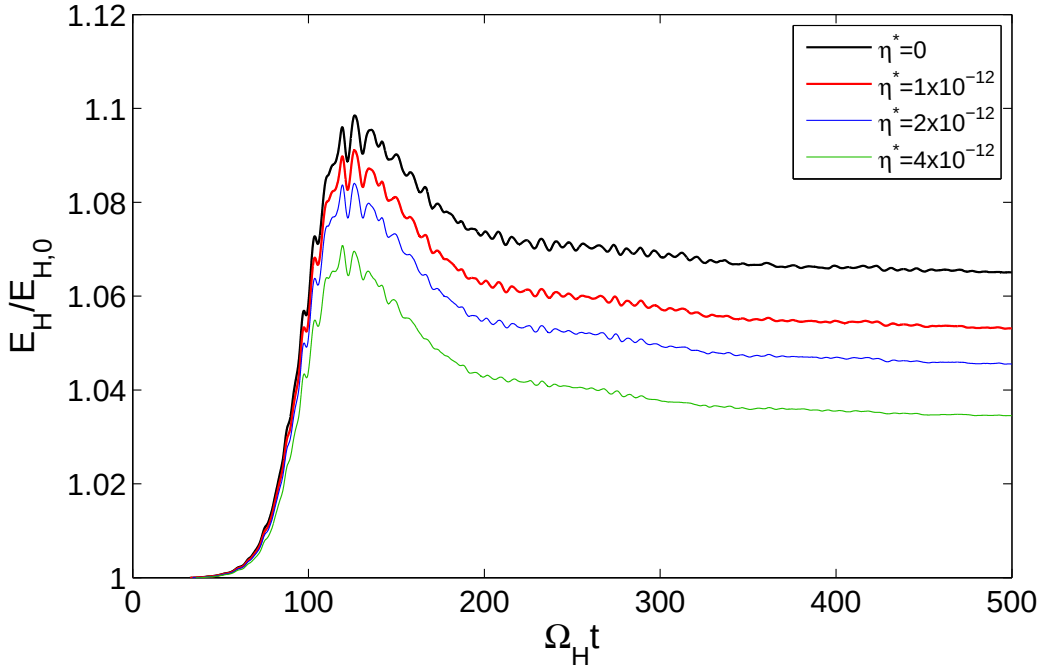

(b) Impact of varying anomalous electron resistivity η^* on hydrogen kinetic energy.

Figure 4.22: Time history of ions kinetic energy for various anomalous electron resistivity η^*.

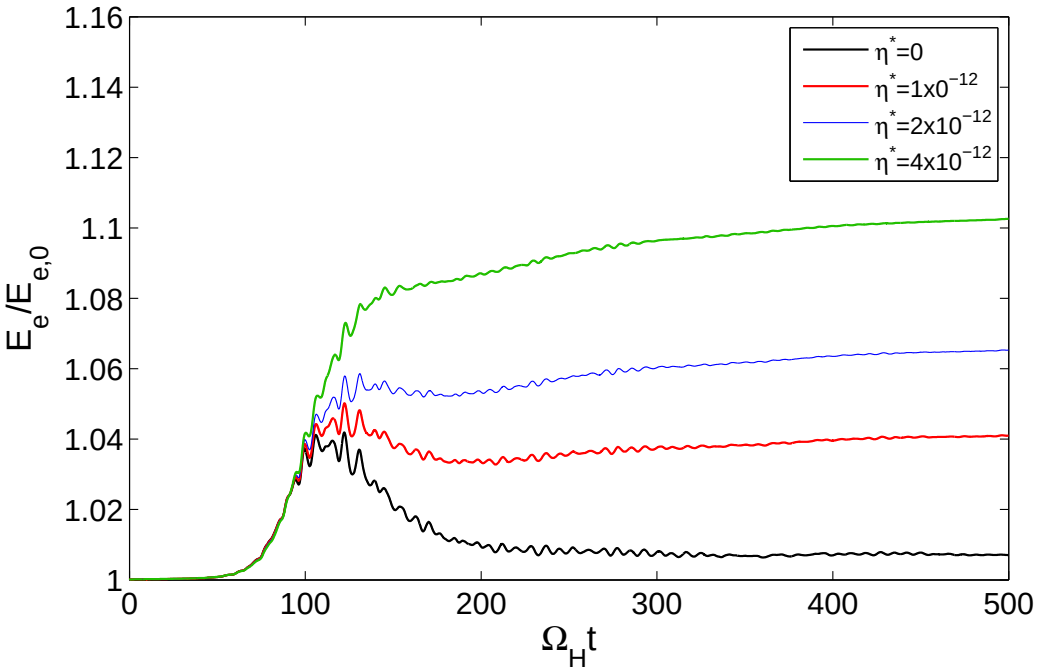

Figure 4.23: Increased fluid electron energy due to enhanced collisions with ions and plasma turbulence for various anomalous electron resistivity η^*.

Chapter 5

Summary and conclusion

The possibility of generating intense electromagnetic plasma turbulence by plasma clouds release to provide control of space weather processes such as radiation belts remediation has been investigated. Such plasma clouds are created through injecting and photoionizing heavy neutral chemicals into a magnetized background plasma typical of the Earth's magnetosphere at altitudes between $3000km$ and $9000km$. A two-dimensional electromagnetic hybrid (fluid electrons and particle ions) model with electron inertia effects included is developed to study the generation and nonlinear evolution of the plasma turbulence. The specific plasma wave modes under consideration here are obliquely propagating shear Alfven waves due to their predicted unique suitability for interaction with relativistic electrons in the Earth's radiation belts. An essential ingredient for the success of the whole process is the ability to create a ring distribution in the perpendicular velocity of the injected ions. This converts the orbital kinetic energy of the neutrals into a reservoir of free energy for the waves to tap into. Since the orbital kinetic energy is large, it allows for a very large source of energy for exploitation.

An important contribution of this study is that it has verified a number of important qualitative and quantitative predictions of the theoretical scenario for generation and quasi-linear growth of such turbulence as well as provided further physical details of the initial nonlinear evolution. The results also provide estimates of the extraction efficiency of energy from the ring plasma kinetic energy into plasma wave turbulence, the characteristics of the turbulence in a saturated state and the ring plasma density levels that are predicted to efficiently initiate the production of such turbulence. Moreover, the impacts of further nonlinear processes on the energy extraction efficiency is modeled through introducing electron anomalous resistivity. The quantitative results of energy extraction are applied to the theoretical model to show the viability for applications to scattering energetic particles and the remediation of the radiation belt.

The current computational model is restricted to investigation of the initial generation of the plasma turbulence due to the relative small simulation domain size. It does not allow study of further nonlinear processes predicted to occur on much longer time and spatial

scales than considered here. Also it does not allow numerical study of the efficiency of pitch angle scattering of relativistic electrons which needs interactions with much longer wavelength shear Alfven waves. However, the characterization of the generation of the seed electromagnetic turbulence provided here will make such investigations possible in ongoing and future studies.

Larger domain sizes and relativistic particle electrons will be utilized through parallel computing techniques in future studies and may provide further insight into the nonlinear processes and the radiation belt remediation under investigation.

Appendix A

Derivation of the electric field equations

The derivation of the field Eqs. (3.9, 3.11, 3.12) will now be discussed. The basic electron momentum equation including electron inertia term is given in Eq. (3.7) [7]. It can be rewritten as:

$$\vec{E} = -\frac{\vec{v}_e \times \vec{B}}{c} + \eta\vec{J} - \frac{m_e}{e}\frac{d}{dt}\vec{v}_e \tag{A.1}$$

With the quasi-neutrality condition Eq. (3.3), the electron velocity can be expressed as:

$$n_e\vec{v}_e = n_e\vec{v}_i - \frac{\vec{J}}{e} \tag{A.2}$$

Using Eq. (A.2) and Eq. (3.2) to substitute $\vec{v}_e$ and $\vec{J}$ in Eq. (A.1) respectively, the electron momentum equation becomes:

$$\begin{aligned}\vec{E} = &-\frac{\vec{v}_i \times \vec{B}}{c} + \frac{1}{4\pi e n_e}(\vec{\nabla} \times \vec{B}) \times \vec{B} + \frac{c\eta}{4\pi}(\vec{\nabla} \times \vec{B}) \\ &-\frac{m_e}{e}(\frac{\partial}{\partial t} + \vec{v}_e \cdot \vec{\nabla})\vec{v}_i \\ &+\frac{cm_e}{4\pi e^2}(\frac{\partial}{\partial t} + \vec{v}_e \cdot \vec{\nabla})(\frac{\vec{\nabla} \times \vec{B}}{n_e})\end{aligned} \tag{A.3}$$

Substituting $\frac{\partial \vec{B}}{\partial t}$ with Faraday's law Eq. (3.1), the term $\frac{cm_e}{4\pi e^2}\frac{\partial}{\partial t}(\frac{\vec{\nabla}\times\vec{B}}{n_e})$ can be written as:

$$-\frac{c^2 m_e}{4\pi e^2 n_e}\vec{\nabla} \times (\vec{\nabla} \times \vec{E}) - \frac{cm_e}{4\pi e^2 n_e^2}\frac{\partial n_e}{\partial t}(\vec{\nabla} \times \vec{B}) \tag{A.4}$$

Since the electron continuity equation is:

$$\frac{\partial n_e}{\partial t} + \vec{\nabla} \cdot (n_e\vec{v}_e) = 0 \tag{A.5}$$

it can be used to substitute the time derivative term $\frac{\partial n_e}{\partial t}$ in Eq. (A.4). Then we could use the ion momentum equation:

$$\frac{\partial \vec{v}_i}{\partial t} + (\vec{v}_i \cdot \vec{\nabla})\vec{v}_i = \frac{e}{m_i}\vec{E} + \frac{e\vec{v}_i \times \vec{B}}{cm_i} - \frac{e\eta}{m_i}\vec{J} \tag{A.6}$$

to get rid of time derivative of ion flow velocity $\frac{\partial \vec{v}_i}{\partial t}$ in Eq. (A.3) [9, 22]. Here m_i is the PIC ion mass and v_i is ion flow velocity. Finally, using Eq. (A.2) to eliminate $\vec{v}_e$, and substituting n_e back with n_i, the final expression for electric field equation is:

$$\begin{aligned}
&\frac{c^2}{4\pi}(\vec{\nabla}(\vec{\nabla}\cdot\vec{E}) - \nabla^2\vec{E}) + \frac{e^2 n_i(1+\frac{m_e}{m_i})}{m_e}\vec{E} \\
&= -\frac{n_i e^2(1+\frac{m_e}{m_i})}{cm_e}(\vec{v}_i \times \vec{B}) + \frac{e}{4\pi m_e}(\vec{\nabla}\times\vec{B})\times\vec{B} + \frac{ce^2 n_i \eta(1+\frac{m_e}{m_i})}{4\pi m_e}(\vec{\nabla}\times\vec{B}) \\
&+ \frac{c}{4\pi}(\vec{v}_i\cdot\vec{\nabla})(\vec{\nabla}\times\vec{B}) - \frac{c^2}{16\pi^2 e n_i}((\vec{\nabla}\times\vec{B})\cdot\vec{\nabla})(\vec{\nabla}\times\vec{B}) \\
&+ \frac{c}{4\pi}((\vec{\nabla}\times\vec{B})\cdot\vec{\nabla})\vec{v}_i \\
&+ \frac{c}{4\pi}(\vec{\nabla}\cdot\vec{v}_i)(\vec{\nabla}\times\vec{B}) + \frac{c^2}{16\pi^2 e n_i^2}(\vec{\nabla}\times\vec{B})((\vec{\nabla}\times\vec{B})\cdot\vec{\nabla})n_i
\end{aligned} \tag{A.7}$$

Since $\frac{m_e}{m_i} \ll 1$ which indicates the term $\frac{m_e}{m_i}$ can be neglected, Eq. (A.7) then becomes Eq. (3.9) in section 3.1. The advantage of Eq. (A.7) is that it incorporates the finite electron inertia without containing an explicit time derivative.

However, since the dispersion relation requires $\nabla\cdot\vec{E} \neq 0$, it can not be assumed that $\nabla\cdot\vec{E} = 0$ in Eq. (A.7). However, at the same time the quasi-neutral assumption which indicates $\vec{\nabla}\cdot\vec{E} = 4\pi e(n_i - n_e) \approx 0$ must be maintained. Solving Eq. (A.7) explicitly, numerical inaccuracy would be introduced into the simulation due to the direct violation of Poisson's equation $\vec{\nabla}\cdot\vec{E} = 4\pi e(n_i - n_e)$. Thus, solving the field equation with the $\nabla\cdot\vec{E}$ term must be avoided. The method presented here is to sperate electric field into transverse and longitudinal components and take advantage of their identities [18].

$$\begin{aligned}
&\because \vec{E} = \vec{E}_t + \vec{E}_l, \vec{\nabla}\times\vec{E}_l = 0, \vec{\nabla}\cdot\vec{E}_t = 0 \\
&\therefore \vec{\nabla}(\vec{\nabla}\cdot\vec{E}) - \nabla^2\vec{E} \\
&= \vec{\nabla}\times(\vec{\nabla}\times\vec{E}) = \vec{\nabla}\times(\vec{\nabla}\times(\vec{E}_l + \vec{E}_t)) \\
&= \vec{\nabla}\times(\vec{\nabla}\times\vec{E}_t) = \vec{\nabla}(\vec{\nabla}\cdot\vec{E}_t) - \nabla^2\vec{E}_t \\
&= -\nabla^2\vec{E}_t
\end{aligned} \tag{A.8}$$

Applying the above identity to Eq. (A.7), the transverse electric field equation can be ob-

tained as:

$$
\begin{aligned}
&-\frac{c^2}{4\pi}\nabla^2\vec{E}_t+\frac{e^2n_i(1+\frac{m_e}{m_i})}{m_e}\vec{E}_t\\
&=-\frac{n_ie^2(1+\frac{m_e}{m_i})}{cm_e}(\vec{v}_i\times\vec{B})+\frac{e}{4\pi m_e}(\vec{\nabla}\times\vec{B})\times\vec{B}+\frac{ce^2n_i\eta(1+\frac{m_e}{m_i})}{4\pi m_e}(\vec{\nabla}\times\vec{B})\\
&+\frac{c}{4\pi}(\vec{v}_i\cdot\vec{\nabla})(\vec{\nabla}\times\vec{B})-\frac{c^2}{16\pi^2en_i}((\vec{\nabla}\times\vec{B})\cdot\vec{\nabla})(\vec{\nabla}\times\vec{B})\\
&+\frac{c}{4\pi}((\vec{\nabla}\times\vec{B})\cdot\vec{\nabla})\vec{v}_i\\
&+\frac{c}{4\pi}(\vec{\nabla}\cdot\vec{v}_i)(\vec{\nabla}\times\vec{B})+\frac{c^2}{16\pi^2en_i^2}(\vec{\nabla}\times\vec{B})((\vec{\nabla}\times\vec{B})\cdot\vec{\nabla})n_i\\
&-\frac{e^2n_i}{m_e}\vec{E}_l
\end{aligned}
\tag{A.9}
$$

Throwing away the term $\frac{m_e}{m_i}$, Eq. (A.9) is same as Eq. (3.11) in section 3.1.

The electron and ion momentum equations can be summed (assuming $n_e = n_i$) to be obtain:

$$
\begin{aligned}
&\frac{\partial\vec{J}}{\partial t}+n_i(\vec{v}_i\cdot\vec{\nabla})\frac{\vec{J}}{n_i}+(\vec{J}\cdot\vec{\nabla})(\vec{v}_i-\frac{\vec{J}}{en_i})+\frac{\vec{J}}{n_i}\vec{\nabla}\cdot(n_i\vec{v}_i)\\
&=e^2n_i(\frac{1}{m_i}+\frac{1}{m_e})(\vec{E}_l+\vec{E}_t)\\
&+\frac{e^2n_i}{c}(\frac{\vec{v}_i}{m_i}+\frac{\vec{v}_e}{m_e})\times\vec{B}-e^2n_i\eta(\frac{1}{m_i}+\frac{1}{m_e})\vec{J}
\end{aligned}
\tag{A.10}
$$

Here $\vec{J}$ is total current density, equal to $en_i(\vec{v}_i-\vec{v}_e)$. Next $\vec{E}_l$ is substituted with $-\nabla\phi_e$, where ϕ_e is a scalar potential, and then the divergence $\vec{\nabla}\cdot$ on both sides of Eq. (A.10) is taken. Note that the divergence of the first left hand side term will then vanish as a result of quasi-neutrality $\vec{\nabla}\cdot\vec{J}=0$. Using the same approach in the derivation of transverse component to get rid of electron velocity $\vec{v}_e$, the longitudinal field equation which is written in terms of the electric scalar potential can be obtained as:

$$
\begin{aligned}
&\nabla^2\phi_e + \frac{1}{n_i}(\vec{\nabla}n_i \cdot \vec{\nabla}\phi_e) \\
&= \frac{1}{c}(\vec{B}\cdot(\vec{\nabla}\times\vec{v_i}) - \vec{v_i}\cdot(\vec{\nabla}\times\vec{B})) + \frac{1}{cn_i}(\vec{v_i}\times\vec{B})\cdot\vec{\nabla}n_i \\
&+ \frac{1}{4\pi e n_i(1+\frac{m_e}{m_i})}(\vec{B}\cdot\nabla^2\vec{B} + (\vec{\nabla}\times\vec{B})\cdot(\vec{\nabla}\times\vec{B})) - \frac{c\eta}{4\pi n_i}(\vec{\nabla}\times\vec{B})\cdot\vec{\nabla}n_i + \frac{1}{n_i}(\vec{\nabla}n_i\cdot\vec{E_t}) \\
&- \frac{cm_e}{4\pi e^2 n_i(1+\frac{m_e}{m_i})}((\vec{\nabla}\times\vec{B})\cdot(\vec{\nabla}(\vec{\nabla}\cdot\vec{v_i})) + \vec{\nabla}\cdot((\vec{v_i}\cdot\vec{\nabla})(\vec{\nabla}\times\vec{B}) + (\vec{\nabla}\times\vec{B}\cdot\vec{\nabla})\vec{v_i})) \\
&+ \frac{c^2 m_e}{16\pi^2 e^3 n_i^2(1+\frac{m_e}{m_i})}\vec{\nabla}\cdot((\vec{\nabla}\times\vec{B}\cdot\vec{\nabla})(\vec{\nabla}\times\vec{B})) \\
&- \frac{c^2 m_e}{16\pi^2 e^3 n_i^3(1+\frac{m_e}{m_i})}(\vec{\nabla}\times\vec{B})\cdot((\vec{\nabla}\times\vec{B}\cdot\vec{\nabla})(\vec{\nabla}n_i) + (\vec{\nabla}n_i\cdot\vec{\nabla})(\vec{\nabla}\times\vec{B}) - \vec{\nabla}n_i\times\nabla^2\vec{B}) \\
&- \frac{c^2 m_e}{16\pi^2 e^3 n_i^3(1+\frac{m_e}{m_i})}\vec{\nabla}n_i\cdot((\vec{\nabla}\times\vec{B}\cdot\vec{\nabla})(\vec{\nabla}\times\vec{B})) \\
&+ \frac{c^2 m_e}{8\pi^2 e^3 n_i^4(1+\frac{m_e}{m_i})}((\vec{\nabla}\times\vec{B})\cdot\vec{\nabla}n_i)^2
\end{aligned}
\tag{A.11}
$$

Neglecting the term $\frac{m_e}{m_i}$, Eq. (A.11) then becomes Eq. (3.12) section 3.1.

Bibliography

[1] K. Akimoto and K. Papadopoulos. Lower-hybrid instabilities driven by an ion velocity ring. *J. Plasma Phys.*, 34:445, 1985.

[2] J. A. Van Allen and L. A. Frank. Radiation around the Earth to a radial distance of 107,400 km. *Nature*, 183:430, 1959.

[3] C. K. Birdsall and A. B. Langdon. *Plasma Physics via Computer Simulation.* New York: McGraw-Hill, 1991.

[4] N. Brice and C. Lucas. Influence of magnetospheric convection and polar wind on loss of electrons from the outer radiation belt. *J. Geophys. Res.*, 76:900, 1971.

[5] Encyclopadia Britannica. Van Allen radiation belt. . http://www.britannica.com/EBchecked/topic/622563, 2009.

[6] G. Chae. *Numerical Simulation of Ion Waves in Dusty Plasmas.* PhD thesis, Virginia Polytechnic Institute and State University, 2000.

[7] Francis F. Chen. *Introduction to Plasma Physics and Controlled Fusion.* New York: Plenum Press, 1974.

[8] C. R. Clauer. Lecture notes from Introduction to Space Science, 2008.

[9] P. A. Damiano, R. D. Sydora, and J. C. Samson. Hybrid magnetohydrodynamics-kinetic model of standing shear alfven waves. *J. Plasmas Phys.*, 69:277, 2003.

[10] A. Z. Dolginov and V. M. Ostryakov. Rayleigh-taylor instability in the plasma of solar prominences. *Astron. Zh.*, 57:1302, 1980.

[11] E. Dubinin, K. Sauer, and J. F. McKenzie. Nonlinear inertial and kinetic alfven waves. *J. Geophys. Res.*, 110:A10S04, 2005.

[12] P. Dyal. Particle and field measurements of the starfish diamagnetic cavity. *J. Geophys. Res.*, 111:A12211, 2006.

[13] Max Planck Institute for Plasma Physics (IPP). Plasma Turbulence: Research. http://www.ipp.mpg.de/∼fsj/research.html, 2009.

[14] G. Ganguli, P. Palmadesso, and J. Fedder. Temporal evolution of whistler growth in a cold plasma injection experiment. *J. Geophys. Res.*, 89:7351, 1984.

[15] G. Ganguli, L. Rudakov, M. Mithaiwala, and K. Papadooulos. Gneration and evolution of intense ion cyclotron turbulence by artificial plasma cloud in the magnetosphere. *J. Geophys. Res.*, 112:A06231, 2007.

[16] B. L. Giles, M. A. McCook, M. W. McCok, and G. P. Miller. CRRES Combined Radiation and Release Effects Satellite Program. Technical report, NASA Technical Memorandum, 1995.

[17] D. Hastings and H. Garrett. *Spacecraft-Environment Interactions*. Cambridge University Press, 2004.

[18] D. W. Hewett and C. W. Nielson. A multidimensional quasineutral plasma simulation model. *J. Comput. Phys.*, 29:219, 1978.

[19] R. B. Horne and R. Thorne et al. Wave acceleration of electrons in the Van Allen radiation belts. *Nature*, 437:227, 2005.

[20] W. Horton and G. Hu. Plasma turbulence. Technical report, The Institute for Fusion Studies, IFSR-827, 1999.

[21] U. S. Inan, T. F. Bell, J. Bortnik, and J. M. Albert. Controlled precipitation of radiation belt electrons. *J. Geophys. Res.*, 108:1186, 2003.

[22] S. T. Jones and S. E. Parker. Including electron inertia without advancing electron flow. *J. Comput. Phys.*, 191:322, 2003.

[23] M. G. Kivelson and C. T. Russell. *Introduction to Space Physics*. Cambridge University Press, 1995.

[24] J. K. Lee and C. K. Birdsall. Velocity space ring-plasma instability, magnetized, part I and II. *Phys. Fluids*, 22:1306, 1979.

[25] A. S. Lipatov. *The Hybrid Multiscale Simulation Technology*. Springer-Verlag, Heidelberg, Germany, 2001.

[26] L. R. Lyons. Pitch angle and energy diffusion coefficients from resonant interactions with ion-cyclotron and whistler waves. *J. Plasma Phys.*, 12:417, 1974.

[27] K. G. McClments, R. Bingham, J. J. Su, J. M. Dawson, and D. S. Spicer. Lower hybrid resonance acceleration of electrons and ions in solar flares and the associated microwave emission. *Astrophysical J.*, 409:465, 1993.

[28] N. P. Meredith, M. Cain, R. B. Horne, R. M. Thorne, D. Summers, and R. R. Anderson. Evidence for chorus-driven electron acceleration to relativistic energies from a survey of geomagnetically disturbed periods. *J. Geophys. Res.*, 108:1248, 2003.

[29] Committee on Solar and Space Physics. Space Weather: A Research Perspective. Technical report, National Academy of Sciences, 1997.

[30] O. G. Onishchenko, O. A. Pokhotelov, R. Z. Sagdeev, L. Stenflo, V. P. Pavlenko, P. K. Shukla, and V. V. Zolotukhim. Modification of Kolmogorov spectra of weakly turbulent shear Alfven waves by dust grains. *Phys. Plasmas*, 10:69, 2003.

[31] S. A. Orszag. Numerical simulation of incompressible flows within simple boundaries: Accuracy. *J. Fluid Mech.*, 49:75, 1971.

[32] S. A. Orszag. Numerical simulation of incompressible flows within simple boundaries: Galerkin (spectral) representations. *Studies in Appl. Math.*, 50:395, 1971.

[33] S. A. Orszag. Comparison of pseudospectral and spectral approximation. *Studies. in Appl. Math.*, 51:253, 1972.

[34] D. Papadopulos. Satellite Threat Due to High Altitude Nuclear Detonations. Technical report, FAS Space Panel, July 2003.

[35] G. S. Patterson and S. A. Orszag. Spectral calculations of isotropic turbulence: efficient removal of aliasing interactions. *Phys. Fluids*, 14:2538, 1971.

[36] W. H. Press, S. A. Teukolsky, W. T. Vetterling, and B. P. Flannery. *Numerical recipes in FORTRAN: the art of scientific computing, 2nd ed.* Cambridge University Press, 1992.

[37] C. T. Russell. *The Solar Wind and the Earth, edited by S. I. Akasofu and Y. Kamide.* Terra Scientific Publishing Company (TERRAPUB), Tokyo, 1987.

[38] S. Saito, S. P. Gary, H. Li, and Y. Narita. Whistler turbulence: Particle-in-cell simulations. *Phys. Plasmas*, 15:102305, 2008.

[39] W. A. Scales. Lecture notes from Introduction to Space Plasmas, 2008.

[40] W. A. Scales and P. A. Bernhardt. Simulation of high-speed (orbital) releases of electron attachment materials in the ionosphere. *J. Geophys. Res.*, 96:13815, 1991.

[41] W. A. Scales, O. Chang, J. J. Wang, G. Ganguli, L. Rudakov, and M. Mithaiwala. Nonlinear evolution of ion-cyclotron turbulence generated by artificial plasma cloud release. 2009. In preparation.

[42] Rainer Schwenn. Space Weather: The Solar Perspective. . http://solarphysics.livingreviews.org/Articles/lrsp-2006-2/, 2006.

[43] J. R. Shewchuk. An introduction to the conjugate gradient method without the agonizing pain. 1994.

[44] Y. Y. Shprits, D. A. Subbotin, N. P. Meredith, and S. R. Elkingotn. Review of modeling of losses and sources of relativistic electrons in the outer radiation belt. *Journal of Atmospheric and Solar-Terrestrial Physics*, 70:1694, 2008.

[45] P. K. Shukla and L. Stenflo. Decay of a magnetic-field-aligned Alfven wave into inertial and kinetic Alfven waves in plasmas. *Phys. Plasmas*, 12:084502, 2005.

[46] D. Summers and R. M. Thorne. Relativistic electron pitch angle scattering by electromagnetic ion cyclotron waves during geomagnetic storms. *J. Geophys. Res.*, 108:1143, 2003.

[47] D. Summers, R. M. Thorne, and F. Xiao. Relativistic theory of wave-particle resonant diffusion with application to electron acceleration in the magnetosphere. *J. Geophys. Res.*, 103:20487, 1998.

[48] Y. Voitenko and M. Goossens. Cross-scale nonlinear coupling and plasma energization by Alfven waves. *Phys. Rev. Lett.*, 94:135003, 2005.

[49] J. Wang, P. Liewer, and V. Decyk. 3D electromagnetic plasma particle simulations on a MIMD parallel computer. *Comput. Phys. Commun.*, 87:35, 1995.

[50] C. Watt, R. Rankin, and R. Marchand. Kinetic simulations of electron response to shear alfven waves in magnetospheric plasmas. *Phys. Plasmas*, 11:1277, 2004.

[51] D. Winske and N. Omidi. *Hybrid Codes: Methods and Applications, Computer Space Plasma Physics, edited by H. Matsumoto and Y. Omura.* Terra Scientific Publishing Company (TERRAPUB), Tokyo, 1993.

[52] D. Winske, L. Yin, N. Omidi, H. Karimabadi, and K. Quest. *Hybrid Simulation Codes: Past, Present and Future. Space Plasma Simulation, edited by J. Bchner, C. Dum, and M. Scholer. Lecture Notes in Physics*, volume 615. 2003.